UNIVERSITY OF CALIFORNIA

Los Angeles

# Nanostructured Surfaces for High Throughput Lensfree Microscopy and Sensing On a Chip

A dissertation submitted in partial satisfaction of the requirements for the degree Doctor of Philosophy in Electrical Engineering

by

Bahar Khadem Hosseinieh

2012

ABSTRACT OF THE DISSERTATION

Nanostructured Surfaces for High Throughput Lensfree

Microscopy and Sensing On a Chip

By

Bahar Khadem Hosseinieh

Doctor of Philosophy in Electrical Engineering

University of California, Los Angeles, 2012

Professor Aydogan Ozcan, Chair

Lensfree platforms are becoming valuable alternatives to conventional lens-based imaging and sensing methods because they are compact and cost-effective and provide large field-of-view systems more compatible with microfluidic devices. Due to the lack of lenses in these systems, an additional step of processing is required to obtain the final result; however, digital technology and efficient mathematical algorithms make the task rapid and straightforward. In this dissertation, I introduce a lensfree modality utilizing nanostructured surfaces to provide high throughput and on-chip incoherent imaging and plasmonic sensing. In the imaging implementation of the proposed platform, the emitted incoherent light from an object is modulated by a nanostructured surface on top of which the object is placed. Through a

compressive-sensing algorithm, the embedded spatial resolution and intensity information are extracted. In the sensing implementation, the light source illuminates the surface of the microfluidic substrate that is placed on top of an image sensor. The bottom layer of the microfluidic device is a metal-coated glass layer on top of which there are arrays of nano-slits modulating the transmission of light so that the diffraction pattern of those structures on the image sensor alters based on the amount of change in the refractive index. In addition, I explain how the pixel super resolution method can be deployed in lensfree incoherent imaging to provide a high-resolution image out of a series of low-resolution frames that have shifted in relation to each other.

The dissertation of Bahar Khadem Hosseinieh is approved.

Oscar M. Stafsudd, Jr.

Benjamin M. Wu

Benjamin Williams

Aydogan Ozcan, Committee Chair

University of California, Los Angeles

2012

## Table of Contents

## Acknowledgment

I would like to express my deep appreciation of and best wishes for the people who, throughout these five years of my PhD studies, have supported me both with aspects of the research itself and by helping make my personal life more compatible with my academic one so that I could focus more on my project.

To my supervisor Professor Aydogan Ozcan, I offer my sincerest thanks, appreciation, and respect. With his expertise in the field and motivation and enthusiasm for research, he was an inspiration. I am grateful for the privilege to learn from his technical knowledge and the example of his managerial skills.

I also appreciate the invaluable support and guidance of my PhD committee members Professor Oscar Stafsudd, Professor Benjamin Wu, and Professor Benjamin Williams.

I sincerely thank the talented members of our lab. I cannot imagine having progressed in my research without their assistance. The lab's postdoctoral scholars, Dr. Gabriel Biener, Dr. Justin Su, Dr. Hongying Zhu, Dr. Euan McLeod, Dr. Zoltan Grocos, Dr. Songkyu Seo, Dr. Waheb Bishara, and Dr. Sam Mavandadi, provided critical help to me at the necessary moments, and I benefited from the experience that they had each spent a long time gaining. Ikbal, Ahmet, Serhan, Swati, Derek, Alon, Frank, Steve, Liang, Serap, Caglar, Onur, Andy, Oguzhan, Evan, Randy, and Uzair also devoted valuable and wonderful collaborative time, without which I could not have succeeded.

I am also very grateful to the Engineering Department staff members who were always available to make our work environment pleasant and comfortable: Deeona, Mandy, Michelle, and Lori.

My most heartfelt thanks go to my parents. I am very blessed to have their unconditional support and love. This was especially important in very hard days when I needed help most. I would also like to thank my sister, Banafsheh, who, although thousands of miles of physical distance are between us, has always been available, loving, and helpful.

Please accept my thanks and appreciation. My best wishes for you all.

# Vita

| | |
|---|---|
| 2001-2005 | Bachelor of Science in Electrical Engineering |
| | University of Tehran, Iran |
| 2005-2007 | Master of Science in Electrical Engineering, Fields and Waves |
| | University of Tehran, Iran |

**Journal Publications**

B. Khademhosseinieh, G. Biener, I. Sencan, T. Su, A.F. Coskun and A. Ozcan, "Lensfree Sensing on a Micro-fluidic Chip using Plasmonic Nano-apertures," Applied Physics Letters, vol 97**,** no. 22, p.221107, 2010.

B. Khademhosseinieh, G. Biener, I. Sencan, and A. Ozcan, "Lensfree Color Imaging On a Nanostructured Chip using Compressive Decoding," Applied Physics Letters, vol. 97**,** no.21, p.211112, 2010.

B. Khademhosseinieh, I. Sencan, G. Biener, T. Su, A.F. Coskun, D. Tseng and A. Ozcan , "Lensfree On-chip Imaging using Nanostructured Surfaces," Applied Physics Letters, vol. 96, no.17, p. 171106, 2010.

C. Oh, S. O. Isikman, B. Khademhosseinieh, and A. Ozcan, "On-chip differential interference contrast microscopy using lensless digital holography," Optics Express, vol. 18, Issue 5, pp. 4717-4726, 2010.

O. Mudanyali, D. Tseng, C. Oh, S.O. Isikman, I. Sencan, W. Bishara, C. Oztoprak, S. Seo, B. Khademhosseini, and A. Ozcan, "Compact, Light-weight and Cost-effective Microscope based on Lensless Incoherent Holography for Telemedicine Applications," Lab on a Chip, vol. 10, no. 11, p.1417, 2010.

**International Conference Publications**

B. Khademhosseinieh, G. Biener, I. Sencan, "Lens-free, near-infrared (NIR) imaging using structured substrates and compressive sensing", SPIE Defense, Security, and Sensing Conference, April 23-27 2012 Baltimore, Maryland USA, Paper # 8373-95

B. Khademhosseinieh, I. Sencan, G. Biener, A.Ozcan, “Use of Nanostructured Surfaces to Enable Higher Resolution Detector Arrays for Lensfree Imaging and Sensing on a Chip", Nanoelectronic Devices for Defense and Security Conference ( Nano DDS), New York, August 29-September 1, 2011, ( Invited Talk)

B. Khademhosseinieh, G. Biener, I. Sencan, T. Su, A.F. Coskun and A. Ozcan, “Plasmonic Nano-Apertures for Lensfree On-chip Sensing,” OSA Conference on Lasers and Electro-optics (CLEO ’11) (May 1-6, 2011), Baltimore, Maryland USA, Paper # CTuZ4

B. Khademhosseinieh, G. Biener, I. Sencan, and A. Ozcan, “Lensless On-Chip Color Imaging using Nanostructured Surfaces and Compressive Decoding,” OSA Conference on Lasers and Electro-optics (CLEO ’11) (May 1-6, 2011), Baltimore, Maryland USA, Paper # CTuM1

B. Khademhosseinieh, G. Biener, I. Sencan, T. Su, A.F. Coskun and A. Ozcan, “Lensfree sensing on a chip using plasmonic nano-apertures,” SPIE Defense, Security, and Sensing Conference, April 25-29 2011 Orlando, USA, Paper # 8024-8

B. Khademhosseinieh, I. Sencan, G. Biener, T. Su, A.F. Coskun, D. Tseng, and A. Ozcan, “Incoherent lensfree imaging on a chip using compressive decoding of nanostructured surfaces,” SPIE Photonics West, Nanoscale Imaging, Sensing, and Actuation for Biomedical Applications VII, January 2011, San Francisco, CA, paper # 7908-21

I. Sencan, A. F. Coskun, B. Khademhosseinieh, T. Su, G. Biener, and A. Ozcan, “Compressive decoding for incoherent lensfree on-chip imaging,” SPIE Photonics West, Three-Dimensional and Multidimensional Microscopy: Image Acquisition and Processing XVIII, January 2011, San Francisco, CA, paper # 7904-45

B. Khademhosseinieh, I. Sencan, G. Biener, T. Su, A.F. Coskun, D. Tseng, A. Ozcan, “Lensfree Incoherent Microscopy on Nanostructured Chips,” BMES Annual Meeting, October 6-9 2010, Austin Texas USA

B. Khademhosseinieh, I. Sencan, G. Biener, T. Su, A.F. Coskun, D. Tseng, A. Ozcan**,** “Nanostructured surfaces for lensless incoherent microscopy on a chip” 11th Annual UC Systemwide Bioengineering Symposium, June 17-19, 2010, University of California, Davis, US

O. Mudanyali, D. Tseng, S.O. Isikman, I. Sencan, W. Bishara, C. Oztoprak, S. Seo, B. Khademhosseini, and A. Ozcan, “Compact and Light-weight Telemedicine Microscope based on Lensfree On-Chip Imaging,” BMES Annual Meeting, October 6-9 2010, Austin Texas USA

O. Mudanyali, D. Tseng, S.O. Isikman, I. Sencan, W. Bishara, C. Oztoprak, S. Seo, B. Khademhosseini, and A. Ozcan, “Light-weight, Field-portable and Cost-effective Lensfree Microscopy for Telemedicine Applications,” 11th Annual UC Systemwide Bioengineering Symposium, June 17-19, 2010, University of California, Davis, USA

# Chapter 1 Introduction

## 1.1 Microscopy

Over the last several decades, advances in optical microscopy have produced a revolution in science, especially in biology and medicine. Seeing cellular structures more clearly has allowed scientists to prevent and cure many diseases. Imaging modalities can be categorized as either *coherent* or *incoherent*, depending upon the data derived as the rays from a given object (cell, tissue, etc.) reach the microscope. With coherent linear imaging systems, the object's amplitude and phase are both used to obtain the amplitude and phase of the output. By contrast, with incoherent imaging systems, there is no phase information for the input, and therefore, we can obtain only the image's intensity pattern in the output [1], [2]. For most applications, having information about the intensity alone is sufficient to detect the sample's features. In addition, in some cases, such as fluorescent microscopy, there is no information about the input phase due to the random nature of the process [3], [4].

Through well-designed and well-placed lenses and optical components, microscopy can provide a magnified image of the object of interest. Combining regular optical microscopes and electronic components has improved the quality and ease of imaging. Recording images in a digital format makes it possible to see each part of the image through pixels. In addition to the advances in digital recording, much has been done to improve the resolution of imaging through super-resolution techniques that overcome the limitations of pixel size and the signal-to-noise ratio (SNR). However, for the majority of biomedical applications, the decent resolution ($\lambda/2NA$) obtainable which is around 0.3 μm in the visible range, is sufficient for identifying critical components in biological samples. This is especially true for clinical purposes and pathological

and cytometry applications. In such cases, the *field-of-view,* or screening area, is highly important, particularly when looking for specific cells in a large piece of tissue or in a liquid [3], [5].

## 1.2 Lensfree Imaging

Lensfree imaging has been recognized as a compact and cost-effective method that can provide a high-throughput platform. In this method, the imaging area is not limited to the lens's focusing point; lensfree imaging can therefore provide decent resolution over the whole field of view [3]. Several lensless techniques have been merged with advanced technology to miniaturize imaging and sensing systems.

One of the most common lensfree optical imaging techniques is inline *holography*. This is based on recording interference between illumination and the light diffracted by the object, and it requires partial coherency for illumination, as shown in Fig. 1-1. The first holographic microscope [6] was based on the *inline* technique, which means that the light source, object, and recording plane are on one axis [6], [7].

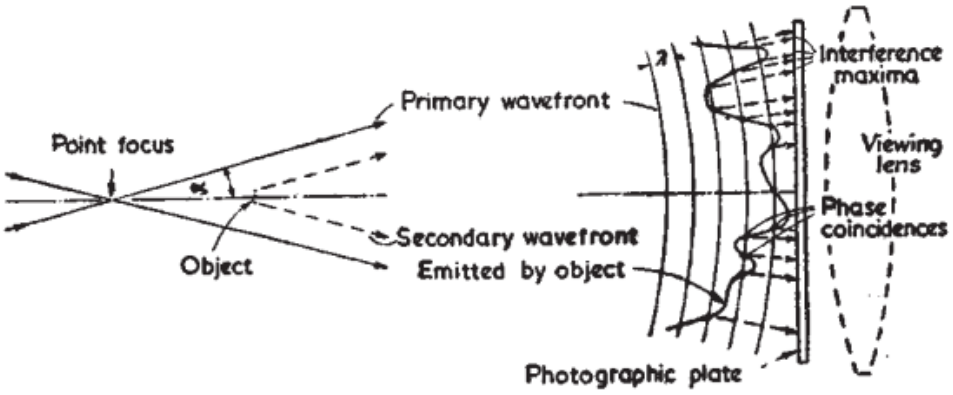


**Figure 1-1 | Original inline holography imaging method [6]. Figure reprinted from [6] by permission from Nature Publishing Group, copyright (1948).**

Digital holography (DH) is an approach that deploys digital technology such as a CCD or CMOS camera in holography for fast and nondestructive imaging of both phase and amplitude objects [8]. The imaging possible with this technique is of a quality suitable for biological samples., and increasing its imaging area makes this methodology perfect for medical applications [8–10]. Unlike with regular traditional optical holography, the imaging area of digital holography is highly limited, to the image sensor array. Some methods have been introduced to overcome this problem, such as the one described by Di (2008), which works based on scanning a CCD [8].

Combining inline holography, lensfree imaging, and information processing for image reconstruction has provided a new method suitable for 3D micron-level resolution imaging for biological applications [11]. Lensfree digital inline holography makes possible rapid transparent specimen imaging without being limited to a lens's focusing area. In this modality, the magnification ($M$) is defined based on the ratio between the source-screen and source-sample distances and can affect the final resolution by overcoming the pixel-size limitation. In other words, increasing $M$ will magnify the hologram to be sampled by the image sensor at the cost of reducing signal intensity and, thus, the signal-to-noise ratio (SNR) [7], [11].

## 1.3 Lensfree On-Chip Holographic Imaging

Researchers in Professor Aydogan Ozcan's laboratory at UCLA have shown a lensfree imaging technique based upon digital inline holography with a partially incoherent light source that can provide a screening area as large as the surface of the image sensor without using any bulky optical component (e.g., lens) or a scanning area [3], [7]. In this technique, the glass slide containing a biological sample is put directly on the surface of a CCD or CMOS image sensor.

The glass slide therefore prevents the object from directly touching the image sensor. Because the glass slide, the air gap between its layers, and the image sensor's protective layer together create distance between the object and the sensing area, diffraction patterns**,** instead of real images, of the sample area sitting on top of the sensor are recorded [3], [7], [12]. The illumination source can be a simple LED light source placed at a distance of around 4-10 cm from the surface of the sample slide. A relatively large pinhole (~ 50-100 μm) is enough to provide a coherence diameter of ~ 0.2-0.5 mm on the image plane. This amount of coherency is needed for phase recovery and image-reconstruction purposes [3], [12].

As shown in Fig.1-2, with a holographic microscope, part of the light is scattered by sample components, such as blood cells, and the portion of the light that is unperturbed reaches the sensor. To use holography terminology, a *reference light* (unperturbed wave) and an *object wave* (scattered light) consequently interfere with each other on the image plane. If we show the reference wave as $R(x, y, z_0)$ and the scattered wave as $s(x, y, z_0)$, the interference between these two waves on the detection screen can be mathematically interpreted in the following form [5], [7]:

$$I(x,y) = |R(x,y,z_0) + s(x,y,z_0)|^2 = |R(x,y,z_0)|^2 + |s(x,y,z_0)|^2 + R^*(x,y,z_0)s(x,y,z_0) + s^*(x,y,z_0)R(x,y,z_0). \quad (1\text{-}1)$$

In this equation, $|R(x, y, z_0)|^2$ indicates the background light coming from illumination, which has a constant value plus noise. The term $|s(x, y, z_0)|^2$ represents the object scattered light, which is weak enough to be neglected in calculations. The summation of the last two terms $R^*(x, y, z_0)s(x, y, z_0) + s^*(x, y, z_0)R(x, y, z_0)$, shows the interference of the reference wave and the scattered light from the object that structures lensfree holograms. To obtain real images from holograms, one step of the image processing should be performed on raw captured images.

This step should involve propagating the hologram back to the object plane, using the known intensity distribution on the sensor plane, the wavelength, and the propagation distance. Free space propagation can be modeled as a linear operation with a particular impulse response. As a result, image reconstruction involves a set of complex number calculation processes [3], [5], [7].

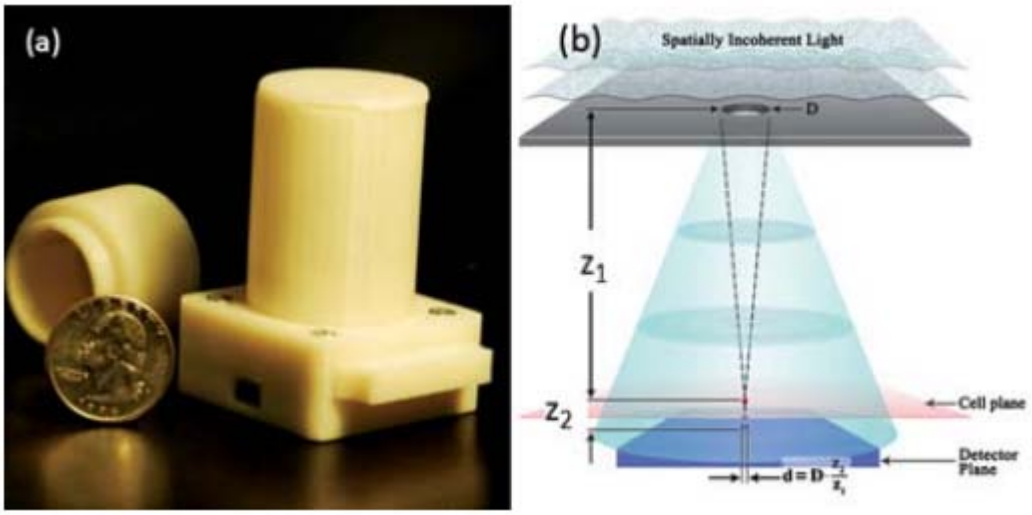


**Figure 1-2 | (a) An actual lensfree microscope, whose size is compared to the US quarter coin [3]. (b) A schematic showing the holographic setup with magnification factor (*M*) equal to 1 [3]. Figure reprinted from [3] by permission from the Royal Society of Chemistry [RSC], copyright (2010).**

This new lensfree on-chip platform has been called *LUCAS* (*lensfree ultra-wide-field cell monitoring array platform based on shadow imaging*) [13]. Due to unit magnification of hologram fringes, the LUCAS system suffers from pixel-size limitation. The idea proposed to tackle this issue is to apply the pixel super-resolution algorithm to achieve high-resolution images by capturing multiple frames for one image [14].

Lensfree incoherent inline holography can provide a differential interference contrast (DIC) imaging tool as well [12]. In lensless DIC imaging (see Fig. 1-3), the coherent hologram of each object enters a thin birefringent crystal optic axis that is at 45° compared to the

propagation direction. Due to the double-refraction property of crystal, when the holographic field is entered, the crystal splits into two holograms with orthogonal polarizations. The phase velocities of both holograms and the energy flow directions differ; therefore, the two holographic fields have a phase difference, relative to each other. The final interference hologram propagates to the sensor array to be captured by the image sensor and analyzed to obtain the real image using image reconstruction algorithm [12].

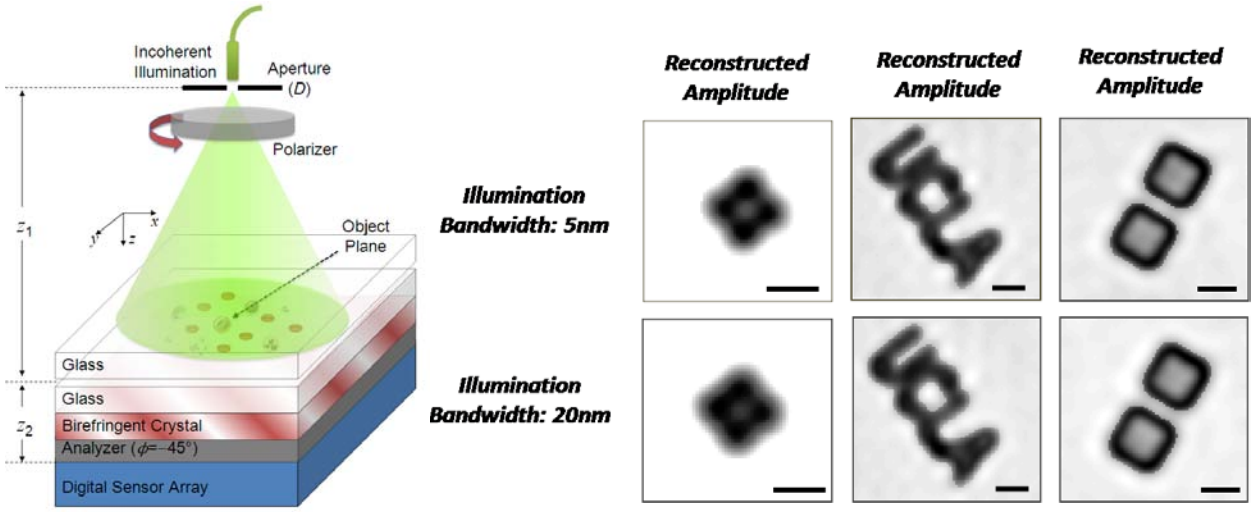


**Figure 1-3 | (a) DIC lensless imaging holography [12]. (b) Image reconstruction of different test objects with well-defined sizes and known refractive indexes [12]. Spatial resolution of < 1.5 µm with a 2.2-µm pixel size has been achieved using the lensfree incoherent DIC method ( scale bars, 5µm). Figure reprinted from [12] by permission from OSA, copyright (2010).**

In addition to holography techniques, there are other onchip imaging methods. For instance, researchers from the Biophotonics Laboratory at the California Institute of Technology have implemented an optofluidic device that offers low-cost and highly compact imaging solutions [15]. When a target specimen is placed on top of a grid, a sampled image of the object can be obtained. The final image is achieved by scanning the object over the grid using a flow system

(see Fig. 1-4). In this technique, resolution is determined by the aperture size and not the image sensor pixel size [15]. The fundamental limitation of OFM is the presence, which can be assumed, of nonrotating objects in the flow. In addition, fabricating well-defined arrays of small holes is an expensive process, which makes the technique undesirable for routine applications.

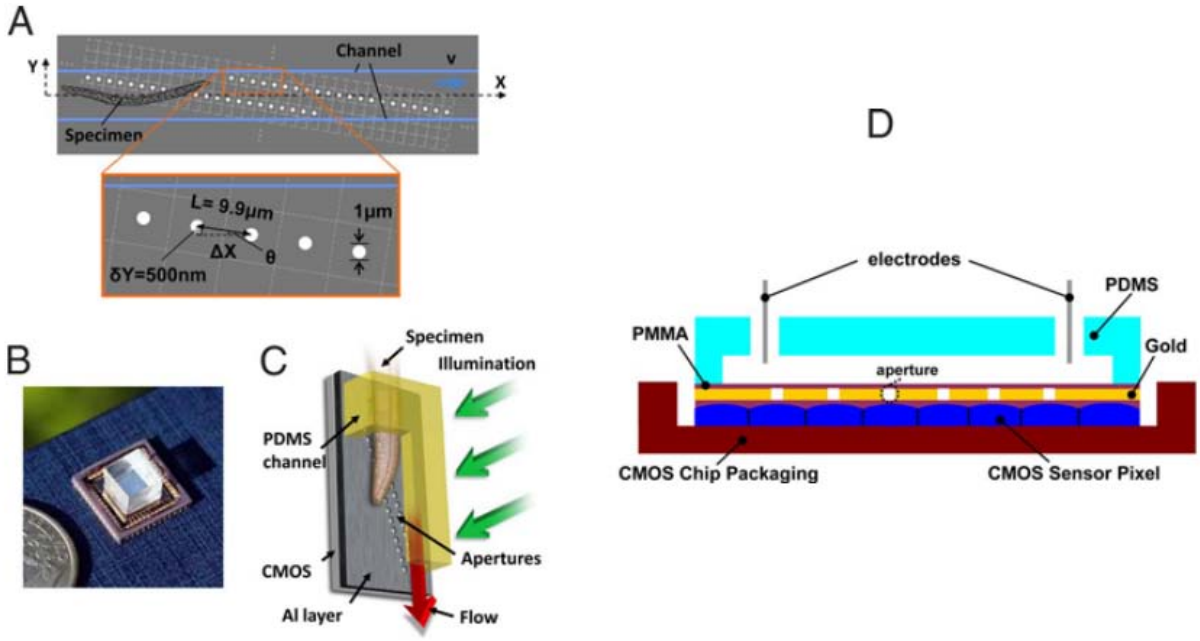


**Figure 1-4 | The OFM [15] device. (a) Schematic of the OFM device. Apertures (white circles) fabricated on the CMOS image sensor which was coated with Aluminum. (b) Depiction of the actual device. (c) Illustration of object's movement in the microfluidic device. (d) Cross-section of the OFM device fabricated on the CMOS sensor. Figure reprinted from [15] by permission granted from PNAS, copyright (2008), National Academy of Sciences, USA.**

## 1.4 Lensfree On-Chip Fluorescent Imaging

The LUCAS technique can be used for samples compatible with inline holography. For fluorescent samples emitting incoherent light, LUCAS can therefore not be used, and a different on-chip modality should be employed. Researchers in Professor Ozcan's lab have introduced a lensfree on-chip modality for fluorescent microscopy that can provide pixel-size resolution

imaging quality over an ~ 60-mm$^2$ area [16]. In this scheme, the excitation light is rejected through total internal reflection that occurs in the bottom facet of the sample substrate, and the fluorescent emission from the sample is then collected by the smaller end of the tapered fiber array and transferred to the image sensor array to be digitally sampled. The image-processing method used in this process is *compressive sensing* (*CS*) [17], which will be described in further detail in Chapter 2. Combining lensfree on-chip fluorescent imaging with the LUCAS system has provided a compact and complete imaging platform for large field-of-view microscopy, especially for biomedical applications [16], [18], [19].

## 1.5 Label-Free Optical Biosensing

Microscopy is an excellent tool for monitoring small-scale components. However, in many cases, all that is required is a system that can detect or sense the existence of a particular component or quantify the amount of a certain chemical. Among all sensor types, optical sensors have gained much attention and improved greatly, due to their compatibility with imaging components and their high level of sensitivity. There are two general types of biological sensors: label-based and label-free. A label-based sensor deploys, as its name suggests, a variety of labels, such as magnetic, fluorescent, and quantum dots, to produce detectable signals during a certain event. This type of sensor has a high degree of sensitivity and provides molecular-level detection. Fluorescent imaging is the most common method for label-based sensing. Although photo bleaching can be regarded as a significant problem with this technique, several solutions, such as utilizing the lately introduced quantum dots, have recently been proposed. The second type of sensor, a label-free one, does not require any specific characteristics for labels, and this is the main advantage it offers over label-based sensors. Label-free sensing is especially valuable in

that it does not interfere with specimens' biochemical structures. It also provides output data from measurements that can be comprehensively analyzed to provide more accurate data in real time [20], [21].

## 1.6 Optical Sensing Using Surface Plasmon Resonance (SPR)

Surface plasmon sensors (SPR) are a group of optical sensors that perform based on resonant electron oscillation when incident light satisfies certain physical conditions. The resonance condition is established when the frequency of light photons matches the natural frequency of surface electrons that are oscillating. The surface plasmon resonance (SPR) effect in nanometer-sized features, such as edges or nanoparticles, is called localized surface plasmon resonance (LSPR) [20], [22]. The SPR phenomenon occurs on a noble metal surface (such as gold or silver) when an incident light beam interacts with the surface at a particular polarization, wavelength, and angle. Depending on the thickness of a biomolecular layer at the metal surface, the SPR phenomenon results in an alteration of the reflected light's intensity. Biomedical applications deploy the high sensitivity of SPR to the permittivity of the medium surrounding the metal surface. This results in detecting and quantifying the adsorption of biomolecules on the metal surface [23]. SPR has had numerous applications in biosensing, especially in the quantification of affinity parameters. The binding antibody is immobilized on the sensor chip, and its antigen is in the liquid flowing on the metal surface. After the light strikes the metal surface, the light intensity is tracked in order to detect the binding affinity [23]. The SPR technique has the advantages of requiring few chemicals, offering rapid results, and not necessitating a labeling process [21], [24].

The most commonly used scheme for utilizing SPR is the Kretschmann configuration. As you see in Fig.1-5, which demonstrates an example of the Kretschmann method, the transmitted light from the microfluidic device is enhanced through surface plasmon resonance effect [24–26].

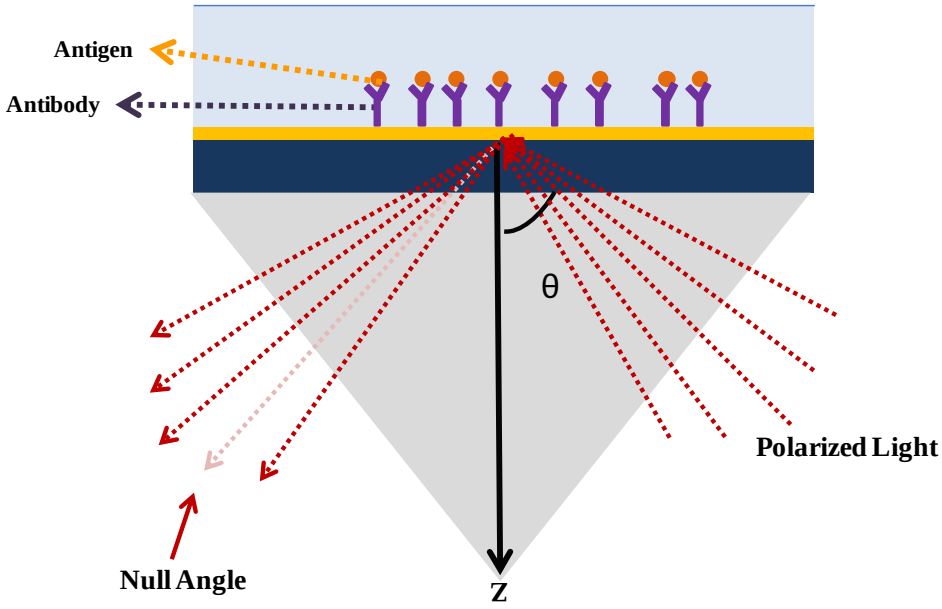


**Figure 1-5 | The polarized light striking the gold-coated substrate reflects back, depending on the angle of illumination and the binding efficiency results in a refractive index alteration on the metal surface. Monitoring the angle at which the reflection has the minimum intensity (i.e., the absorption from surface plasmons has the maximum intensity), makes it possible to calculate the amount of the antigen attached to the immobilized antibody [26].**

In order to increase the throughput or sensing area of the Kretschmann configuration, the reflected light is collimated though optical elements to map a large area of the metal surface to the image sensor array. This technique, because it combines SPR sensing with imaging components, is called SPR imaging or SPRI [27]. SPRI is a powerful technique for monitoring and sensing a large area in a short time, and it is achieved by merging an SPR sensing scheme

with an imaging setup. However, since there are collimator components containing a lens in the system, the whole setup is still bulky and cannot be used as a handheld tool.

Another high-throughput device based on SPR sensing is TI-SPR, manufactured by Texas Instruments. This device does not include any lens and simply maps the sensing area though rays of illumination that travel to the image sensor. As there is no lens or any other bulky optical component, TI-SPR is a compact and cost-effective device that can be used for biosensing applications [28]. It is commercially available under the name Spreeta.

Realizing the full potential of SPR sensors requires integrating plasmonic structures with illumination and detection elements to increase throughput without significant resolution loss [27]. Noteworthy examples of recent achievements in this area are the on-chip plasmonic sensing modalities reported by Professor Hatice Altug's research group at Boston University. One in particular makes use of monopole nanoantennas and circuits for an on-chip plasmonic sensor with potential biological applications [29].

Several other attempts have been made to merge plasmonic concepts with other technologies to make SPR sensors compact and on chip [30], [31].

## 1.7 Thesis Outline

As indicated by the preceding discussion, there is great interest in advancing imaging and sensing modalities by using current technology and computational methods to improve their throughput and make them more compact and cost-effective. Removing physical components such as bulky lenses and relying more on image-processing tools, which are becoming faster and more powerful, results in miniaturized microscopy systems. For instance, the LUCAS technique, which works based on digital inline holography, can produce holograms from a large part of a

sample of, for example, blood or tissue, and these can be processed in a remote computation center to provide high-resolution images in a very short time. Lensfree fluorescent imaging has supplied large field-of-view images from incoherent samples. This powerful technique can satisfy the great demand for fluorescent imaging needed to detect rare particles or subcellular components in a large sample volume. The disadvantage to earlier forms of lensfree incoherent imaging was in resolution due to the space-invariant point-spread function in the system.. In this dissertation, I explain how structured substrates can improve resolution enhancement for incoherent imaging techniques by encoding lensfree farfield diffraction patterns. To test, we assembled an imaging system containing a high-tech Olympus microscope, a 3D Piezo scanning stage, a CCD image sensor, and LED illumination, all of which were interconnected with a synchronization LabVIEW code. We fabricated the structured substrates using deposition and FIB machines in the cleanroom facilities of the UCLA Nanoelectronics Research Facility. For the computational portion of the work, we used compressive-sensing codes to acquire the final images and compare them with the images obtained from a microscope for the proof-of-concept validation. The structured substrate technique can be used not only for fluorescent and biological applications but also for regular lens-based imaging techniques that require a smaller pixel size with artificially increasing pixel density. For instance, in infrared (IR) or near-infrared (NIR) cameras, the main limitation is relatively large pixel size. The fabrication of a large-area infrared image sensor with a small pixel size is a very expensive process. We have shown that the structured substrate technique can be used to increase the pixel density of an NIR camera artificially and obtain higher-resolution images. Although the results attained are for an NIR system with a communication wavelength (1.55 μm), this technique can be used for thermal

imaging that requires a smaller pixel size for image sensors. It can also be applied to any other array-based image sensors.

In addition to utilizing the structured substrate method, we have applied the pixel super-resolution (PSR) technique in lensfree incoherent imaging to enhance the image resolution of incoherent imaging systems especially for fluorescent imaging. Researchers from Professor Ozcan's lab had implemented the PSR technique for the LUCAS system, but using it for fluorescent applications had some challenges. We modified the scanning system that we had set up for the structured substrate imaging method in order to combine the pixel super-resolution technique with lensfree incoherent imaging to permit resolution enhancement in a large imaging area for incoherent imaging as well.

Bulky optical components are a disadvantage of plasmonic sensing devices too. We have deployed farfield lensfree diffraction patterns of an array of subwavelength structures to measure the trace refractive index change inside a microfluidic channel that contains nanostructures. The proposed technology enables large throughput and label-free plasmonic sensing. Professor Ozcan has named this new modality *plasmonic LUCAS* (*PLUCAS*) due to similarities in the setup and processing techniques that exist between the proposed sensing method and the formerly introduced imaging one.

At the end of my thesis, I also introduce optofluidic fluorescent imaging spectroscopy and multicolor cytometry on a cellphone. These techniques are based on tracking and classification methods and require a linear variable filter (LVF). The cellphone and a small device attached to it can be used to classify and count different live particles in a blood sample.

# Chapter 2 Lensfree Incoherent Imaging Using Structured Substrates and Compressive Sensing[1]

## 2.1 Introduction[2]

Lensfree imaging has recently been gaining a lot of consideration due to its capability in creating modalities that can potentially abolish bulky optical components to provide high throughput on-chip microscopy systems [11], [18], [34–39]. Such on-chip microscope designs would particularly benefit microfluidic systems to create powerful capabilities, especially for medical diagnostics and cytometry applications. Because the equipment for lensfree imaging is lightweight and compact, the process can also potentially create an important alternative to

[1] Reprinted with permission from [32], Copyright (2010), American Institute of Physics, and [33], Copyright (2010), American Institute of Physics.

[2] The content of this chapter has been published in or presented at the following: Khademhosseinieh, B., Biener, G., Sencan, I. & Ozcan, A., "Lensfree color imaging on a nano-structured chip using compressive decoding," *Applied Physics Letters* 97(2010); Khademhosseinieh, B., Sencan, I., Biener, G., Su, T., Coskun, A. F., Tseng, D. & Ozcan, A., "Lensfree on-chip imaging using nano-structured surfaces," *Applied Physics Letters* 96 (2010); selected for the *Virtual Journal of Biological Physics Research*; highlighted in *Nature Photonics* 4, 408 (2010)); Khademhosseinieh, B., Biener, G. & Sencan, I., **"**Lens-free, near-infrared (NIR) imaging using structured substrates and compressive sensing**"** (paper # 8373-95), SPIE Defense, Security, and Sensing Conf., Baltimore, MD, USA, 23-27 Apr. 2012; Khademhosseinieh, B., Sencan, I., Biener, G. & Ozcan, A., "Use of nano-structured surfaces to enable higher resolution detector arrays for lensfree imaging and sensing on a chip" (invited talk), Nanoelectronic Devices for Defense and Security Conf. (Nano DDS), New York, USA, 29 Aug.-1 Sept. 2011; Khademhosseinieh, B., Biener, G., Sencan, I., & Ozcan, A., "Lensless on-chip color imaging using nano-structured surfaces and compressive decoding" (paper # CTuM1), in proceedings of OSA Conf. on Lasers and Electro-optics (CLEO '11); 1-6 May 2011, Baltimore, MD, USA; Khademhosseinieh, B., Sencan, I., Biener, G., Su, T., Coskun, A. F., Tseng, D. & Ozcan, A., "Incoherent lensfree imaging on a chip using compressive decoding of nanostructured surfaces" (paper # 7908-21), SPIE Photonics West Conf.: Nanoscale Imaging, Sensing, and Actuation for Biomedical Applications VII, Jan. 2011, San Francisco, CA, USA; Khademhosseinieh, B., Sencan, I., Biener, G., Su, T., Coskun, A. F., Tseng, D. & Ozcan, A., "Lensfree incoherent microscopy on nano-structured chips," BMES Annual Meeting, 6-9 Oct. 2010, Austin, Texas, USA; Khademhosseinieh, B., Sencan, I., Biener, G., Su, T., Coskun, A. F., Tseng, D. & Ozcan, A., "Nano-structured surfaces for lensless incoherent microscopy on a chip" 11th Annual UC Systemwide Bioengineering Symposium, 17-19 June 2010, Univ. of CA, Davis, USA.

conventional lens-based microscopy, especially for telemedicine applications. Researchers from Professor Ozcan's lab at UCLA have shown a lensfree technique for fluorescent imaging that uses a highly compact device and provides large field-of-view imaging for high throughput sample analysis in a short time. In their proposed configuration, the sandwiched sample glass slide is put on the surface of a faceplate fiber array that is placed on the image sensor's surface. Short wavelength excitation beam hits the particles (microbeads, biological particles, etc.) and reflects back from the glass surface with total internal reflection (TIR), while the emission from the beads is collected using a faceplate fiber array and delivered to the image sensor through optical fibers [18], [19]. In this modality, due to the lack of a lens, fluorescent emission from particles is broadened so that the point-spread function (PSF) is around a 40-μm bright spot. The negative effect of broadened PSF on resolution can be eliminated using an inverse problem method, such as compressive sensing, to provide 10-μm resolution over an 8 $cm^2$-area [16], [40].

The main limitation factor for resolution in this system is having space-invariant PSF; in other words, when two point-source emitting particles are sitting close to each other, due to diffraction over a large space in a noisy medium, the overlapped diffraction pattern is similar to that of individual particles. Therefore, the deconvolution methods cannot overcome the effect of noise in calculations to recover two spots instead of one. This limitation was the origin of my idea for increasing the resolution of incoherent imaging systems by *encoding diffraction patterns* using structured substrates, the idea that will be explained in this chapter**.** In the proposed lensfree system with space-variant point-spread function, the lensfree diffraction pattern of particles sitting on different parts would be a 2D pattern. For this reason, compressive sensing [17], [41] was used to decompose the overlapped diffraction pattern into two independent ones. The proof of concept will be shown for both visible and near-infrared objects.

In the first part of this chapter, I will introduce the compressive-sensing theory that we applied in image recovery from the space-variant PSF platform. After that, I will demonstrate the concept and implementation of structured substrates for sub-pixel resolution in lensfree imaging platforms.

## 2.2 Compressive Sensing (Compressive Sampling) Theory

In this part, I briefly explain the fundamental concept of compressive sensing (CS) and how this mathematical technique is utilized as a decomposition tool for signal recovery that is highly robust in noisy conditions.

Assume that we want to recover an unknown matrix $x_0 \in R^m$, which is a sampled representation of matrix $y$ in the equation $y = Ax_0 + v$, where $A$ is an $n \times m$ matrix and $v$ is the noise term in the system [41]. Conventional methods for sampling follow Shannon's theorem, which states that the sampling rate should be at least twice the signal bandwidth; this is called the Nyquist rate. In simpler terms, based on Shannon's theorem, $m$ linearly independent rows are required in matrix $A$. However, based on compressive sensing, a signal can be recovered from far fewer samples than those needed to meet the Nyquist rate under certain conditions. CS performance on sub-Nyquist rate recovery relies on the fundamental principle of *sparsity*. Sparsity states that the "information rate" [42] of a continuous signal is smaller than its bandwidth. Put more simply, the sparsity condition requires that there be few non-zero elements in an unknown matrix, $x$, and that they be located in sparse locations of the representation domain [41–43].

When $n \geq m$, the columns of $A$ are linearly independent, and $x$ can be obtained by minimizing the quadratic loss $\|Ax - y\|_2^2$, where $\|u\|_2 = (\sum_i u_i^2)^{1/2}$ is the $l2$-norm of matrix $u$.

However, if the number of observations, *m*, is smaller than *n*, simple least square method leads to the over-fitting issue [41]. This is the situation in which the continuous proposed function has large deviations from the unknown function, though at sampled points they come very close to each other. One solution introduced to tackle the over-fitting issue is called *l2* or the Tikhonov regularization, which is described as follows:

$$minimize\ \|Ax - y\|_2^2 + \lambda\|x\|_2^2\ , \tag{2-1}$$

where λ is a positive number as the regularization parameter [41].

In the above equation, *Lagrange multipliers* have been deployed to solve an optimization problem. The term to be minimized is $\|x\|_2^2$, and the constraint to be satisfied is $\|Ax - y\|_2^2 = 0$. Using Lagrange multipliers, we can rewrite the equation as to minimize $\|Ax - y\|_2^2 + \lambda\|x\|_2^2$ [44]. The Lagrange method is a commonly used one for handling optimization problems and has been deployed in the following optimizations in compressive sensing. Minimizing the summation of quadratic loss and quadratic amplitude in the Lagrangian format ( $\|Ax - y\|_2^2 + \lambda\|x\|_2^2$) is called the *l2*-regularized least square program (LSP) and has this closed-form analytical solution [41]:

$$x = (A^T A + \lambda I)^{-1} A^T y. \tag{2-2}$$

There is a need to solve this equation for fluorescent imaging cases that contain fluorescent beads or particles spread over a large field of view. In such applications, a method that can provide sparse solutions is much needed. The $l_1$-regularized least square ($l_1$-LS) method is the technique proposed to minimize:

$$minimize\ \|Ax - y\|_2^2 + \lambda\|x\|_1\ , \tag{2-3}$$

where $\|x\|_1 = \sum_i^n |x_i|$ is the *l1* norm of *x*, and $\lambda > 0$ is the regularization parameter. Typically, $l_1$-LS yields a sparse vector, that is, one that has relatively few nonzero coefficients [41] , [06]. A

solution always exists for $l_1$-LS, but because of the degree of freedom to choose $\lambda$, it is not necessarily a unique one. We set the parameters based on the problem we sought to solve, and it provides the best answer. Compared to the solutions obtainable by loss minimization alone, its vector is sparse enough and more similar to the original $x$-vector [41].

We used CS codes provided by Professor Stephen Boyd of Stanford University that can be downloaded from this link: http://www.stanford.edu/~boyd/papers/l1_ls.html.

## 2.3 Lensfree Onchip Imaging Using Nanostructured Substrates[3]

In this part, I explain the proof-of-concept for the incoherent on-chip microscopy platform that uses nanostructured surfaces together with a compressive-sampling algorithm [17], [41], [45] to perform digital microscopy of samples without the use of any lenses, mechanical scanning, or other bulky optical or mechanical components. In this lensfree imaging modality (see Fig. 2-1), the emitted incoherent light from the sample plane is spatially modulated by a nanostructured surface (e.g., a thin metallic film that is patterned) placed directly underneath the sample plane. This modulated light pattern then diffracts over a distance of $\Delta z \sim 0.1$-$0.2$ mm to be sampled by an opto-electronic sensor array such as a CCD or a CMOS chip. The main function of the nanostructured surface is to encode the spatial resolution information into farfield diffraction patterns that are recorded in a lensfree configuration, as shown in Fig. 2-1. This spatial encoding process is calibrated after the fabrication of the nanostructured surface by scanning a tightly focused beam on the surface of the chip. For each position of the calibration spot on the patterned chip, the diffraction pattern in the farfield is measured as shown in Figs. 2-1 and 2. For spatially incoherent imaging (e.g., for fluorescent objects on the chip), these

[3] Reprinted with permission from [32], Copyright (2010), American Institute of Physics

calibration frames provide a basis that permits spatial expansion of any object distribution as a linear combination of these calibration images.

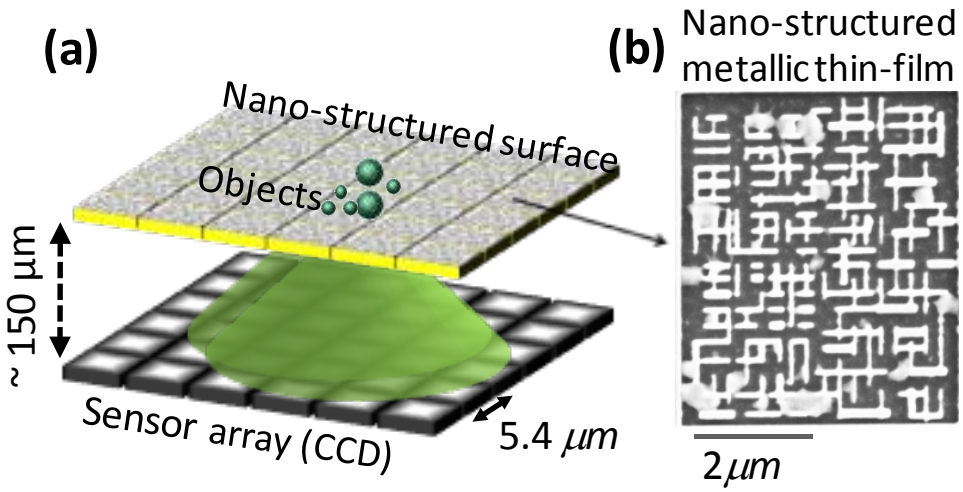


**Figure 2-1 | (a) Schematic diagram of lensfree on-chip imaging using a nanostructured surface. (b) SEM image of a structured chip. Figure reprinted with permission from [32], copyright (2010), American Institute of Physics.**

To gain a detailed sense of the system we used, assume that a metallic thin film, deposited on, for example, a glass substrate, is structured at the nano-scale (see Fig. 2-1). Let us also assume that the transmission of this structured thin-film slab is denoted with $t(\mathbf{r}_a,\ \mathbf{r}_b,\ \lambda)$, where $\lambda$ refers to a wavelength of light, and $\mathbf{r}_a$ and $\mathbf{r}_b$ refer, respectively, to the x-y coordinates at the top and bottom surfaces of the structured thin film. Accordingly, for a point source (i.e., the calibration spot) located at $\mathbf{r} = \mathbf{r}_a$, the detected signal at the m$^{th}$ pixel of the sensor array can be written as

$$I_m(\mathbf{r}_a) = \int_\lambda d\lambda \cdot q(\lambda) \cdot S(\lambda) \int_{\boldsymbol{A}} d\mathbf{r}' \cdot |t(\mathbf{r}_a, \mathbf{r}', \lambda) \otimes h(\mathbf{r}', \lambda, \Delta z)|^2, \qquad (2\text{-}4)$$

where $h(\mathbf{r}',\ \lambda,\ \Delta z)$ denotes the coherent point-spread function of free-space diffraction over a distance of $\Delta z$ (which refers to the distance between the detector surface and the bottom plane of the structured slab); $\boldsymbol{A}$ represents the effective area of pixel #$m$; $S(\lambda)$ is the power spectrum of the calibration point source; $q(\lambda)$ is a spectral function that includes other sources of wavelength dependency in the detection process, such as the quantum efficiency of the detector array; and $\otimes$ denotes the 2D spatial convolution operation. Essentially, Eq. 2-4 describes the formation of the calibration images (see Fig. 2-2), where a complex field, $t(\mathbf{r}_a, \mathbf{r}_b,\ \lambda)$, generated by a point source at $\mathbf{r} = \mathbf{r}_a$ propagates coherently over a distance of $\Delta z$ to be sampled by the detector array.

For an arbitrary 2D incoherent object distribution on the structured substrate, we can in general write the object function as $o(\mathbf{r}_a, \lambda) = S'(\lambda) \sum_n c_n \delta(\mathbf{r}_a - \mathbf{r}_n)$, where $c_n$ values represent the object emission strength at $\mathbf{r}_a = \mathbf{r}_n$, and $S'(\lambda)$ is the object power spectrum. Following a similar derivation as in Eq. 2-4, one can show that the detected object signal at the m$^{th}$ pixel of the sensor array can be written as

$$O_m = \sum_n\ c_n \cdot I_m(\mathbf{r}_n)\ . \tag{2-5}$$

For the derivation of Eq. 2-5, we have assumed $S'(\lambda) = S(\lambda)$, which achieved straightforwardly by appropriately controlling the calibration process.

The above equations indicate that for an arbitrary incoherent object distribution on the structured chip, each pixel value at the detector array ($O_m$) is actually a linear super-position of the calibration values of the same pixel (#$m$) acquired for N different point-source positions, each of which corresponds to an object location on the chip. The simultaneous solution of this linear set of equations for M different pixels should enable the recovery of $c_n$, which is equivalent to imaging of the 2D intensity distribution of the incoherent object on the chip. If M > N, there are more equations than the number of unknowns, and it becomes an over-sampled

imaging system. However, if N > M, then it is an under-sampled imaging system. In this project, we examined the imaging performance of the lensfree system for both under-sampled and over-sampled conditions, within the context of compressive sampling theory [17], [45] which will be further discussed in the experimental results.

It is important to note that Eq. 2-5 also holds for a non-structured transparent substrate. However, such a bare substrate, without the nano-patterning on it, would be of limited use in lensfree incoherent imaging. For a bare substrate, the calibration images at the detector, $I_m(\mathbf{r}_n)$, become highly correlated, especially for closely spaced $\mathbf{r}_n$. This unfortunately makes the solution of Eq. 2-5 for spatially close $c_n$ values almost impossible, limiting the spatial resolution that can be achieved. *Therefore, the function of the nanostructured substrate in this technique is to break this correlation among* $I_m(\boldsymbol{r}_n)$ *for even closely spaced* $\boldsymbol{r}_n$ *values through the creation of unique* $t(\boldsymbol{r}_n, \boldsymbol{r}_b, \lambda)$ *functions at the nano-scale.* As a result of this, the numerical solution of Eq. 2-5 now becomes feasible to improve the resolution of the lensless system, which I demonstrate next through experimental results.

## 2.4 Fabrication Method and Experimental Results

To validate the above predictions experimentally, we used a structured metallic thin-film slab composed of an array of nanoislands (see Fig. 2-2). These nanostructures were fabricated using focused ion-beam milling (FIB - NOVA 600) on borosilicate cover slips (150 μm thick) that were previously coated with 200-nm gold using electron beam metal deposition (CHA Mark 40).

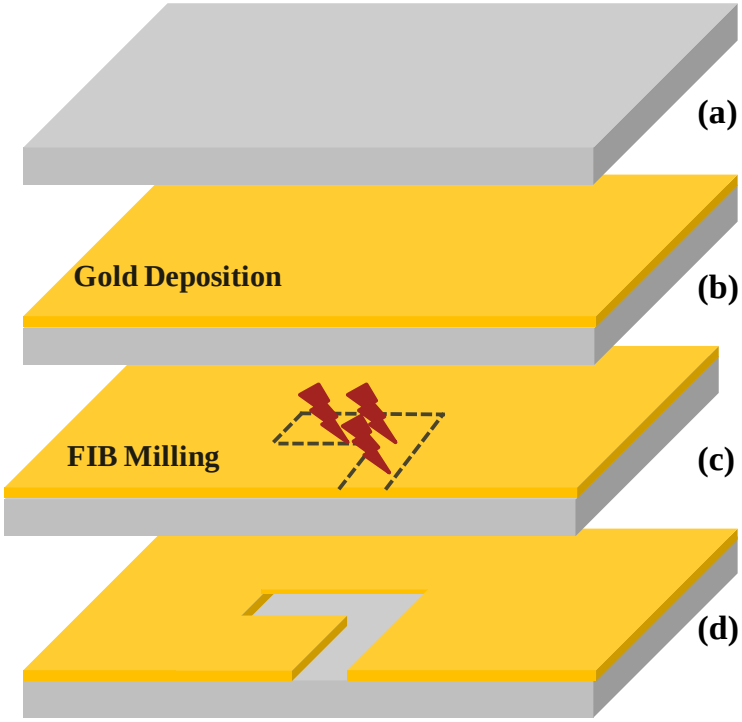


**Figure 2-2 | Schematic showing the fabrication steps of the nanostructured substrate. (a) A 150-µm glass substrate. (b) Gold coating using E-beam evaporation. (c) Bombarding the coated surface with the FIB machine. (d) The patterns are etched through the gold layer.**

The design of the nanostructures was made using finite-difference time-domain (FDTD) simulations (FullWAVE from RSOFT) with the aim of reducing the spatial correlation among $I_m(\mathbf{r}_n)$ for closely spaced points on the chip.

To calibrate the nanostructured chip of Fig. 2-1, we measured $I_m(\mathbf{r}_n)$ using a fiber-coupled light-emitting diode (at 530 nm with a bandwidth of ~ 30 nm) focused to a spot size of < 2 µm (FWHM) on the top surface of the chip. In these calibration experiments, the detector array (Kodak, KAF 8300, pixel size: 5.4 µm) was scanned using a Piezo stage controlled by a LabVIEW code. Using a step size of ~ 0.5 µm in both x and y directions, we acquired a total of N = 120 calibration frames over a 6-µm-x-5-µm area of the structured surface. Figure 2-4 illustrates a diagram of this scanning procedure and presents samples of lensfree calibration

images acquired at the CCD. These calibration frames were then digitally stored for use in the image-decoding process.

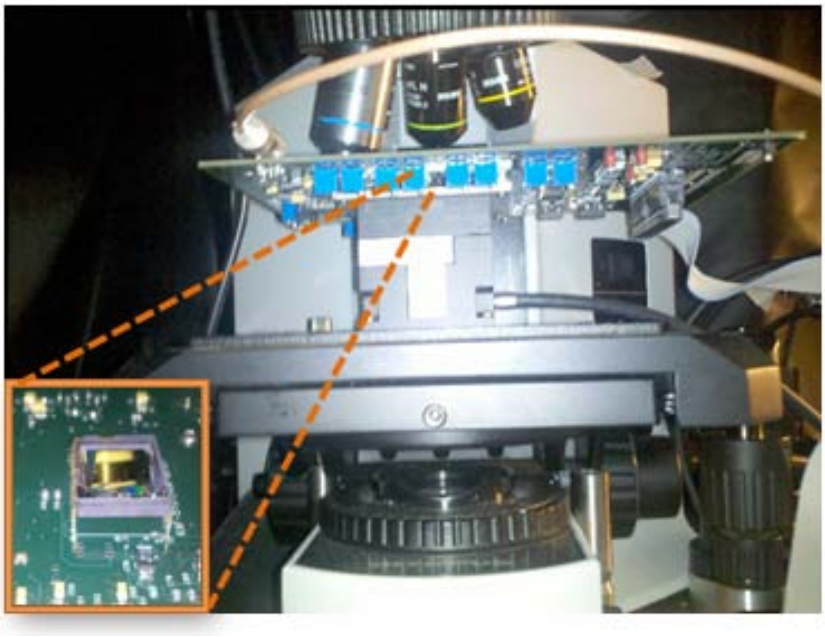

**Figure 2-3 | Experimental setup depicting the circuit board installed on a XYZ scanning Piezo stage. As shown in the inset image, the structured substrate is placed directly on the CCD image sensor.**

Quite importantly, for each nanostructured chip, this calibration process was performed only one time, after which any arbitrary object on the chip could be imaged from just a single lensfree diffraction image and by using the compressive-sampling algorithm based on $l_1$-LS.

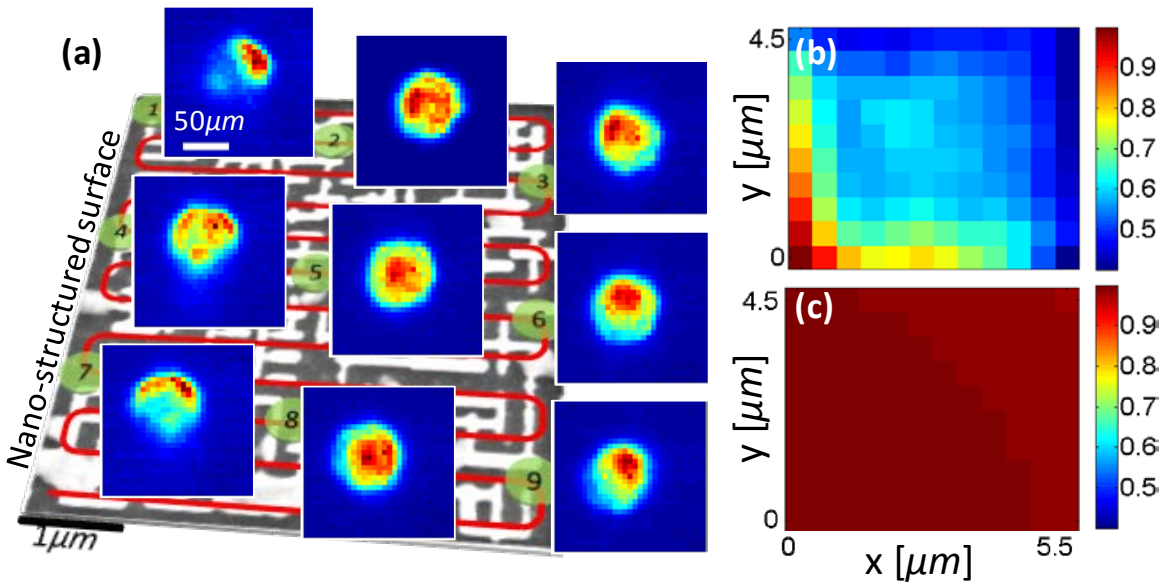


**Figure 2-4 | (a) Calibration process of a nanostructured transmission surface is outlined. Several far-field calibration images of the patterned chip shown in Fig. 2-1(b) are also provided. (b) Cross-correlation coefficients of the first calibration frame against all the other calibration images of the same chip are illustrated. Such correlation maps are computed for all the calibration images of a chip to ensure proper encoding of spatial resolution information into far-field diffraction patterns. (c) Same as part (b), except this time it is measured for a bare glass substrate without the nano-pattern. Significantly higher cross-correlation observed in (c) for closely spaced points is the reason for limited spatial resolution of conventional lensfree incoherent imaging without the nanopattern. Nanostructured surfaces break this correlation as shown in (b) to achieve a significantly better resolution. Figure reprinted with permission from [32], copyright (2010), American Institute of Physics.**

To demonstrate the proof-of-concept and the resolving power of this lensfree imaging modality, we illuminated the calibrated nanostructured chip with two closely spaced incoherent spots, as shown in Fig. 2-5. In these experiments, the center-to-center distance of the object spots was varied between ~ 2 μm and ~ 4 μm, which were all sub-pixel because the pixel size at the CCD was already 5.4 μm. As illustrated in Fig. 2-5, the diffraction images of these sub-pixel objects (after a propagation distance of $\Delta z$ = 150 μm) showed a single large spot at the CCD. To

the bare eye, such a lensfree diffraction image in the farfield obviously did not contain any useful information to predict the sub-pixel object distribution. *However, the nano-structuring on the chip surface enabled imaging of the objects at the sub-pixel level using a compressive-sampling algorithm*. The 2D sparse output of the decoder was then convolved with the calibration spot to create the image of the object. For example, using M = 355 pixels of the CCD image, we reconstructed N = 120 coefficients on the structured chip, resolving sub-pixel objects as demonstrated in Fig. 2-5. The decoding results matched quite well to regular reflection microscope images of the objects, as shown in the inset images of Fig 2-5. The computation times of these decoded images were all between 0.8 and 1.2 sec. using a dual-core processor (AMD Opteron 8218) at 2.6 GHz.

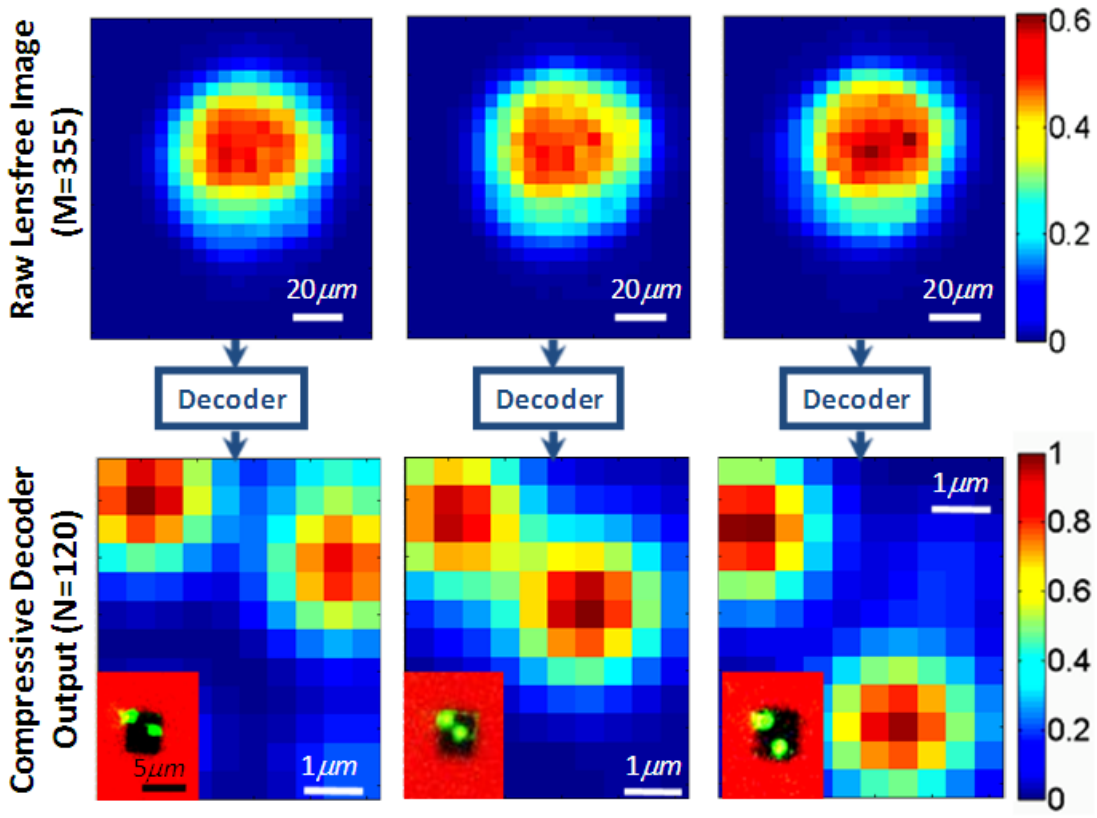


**Figure 2-5 | Experimental proof-of-concept of lensfree on-chip imaging using the nanostructured surface is demonstrated. Top row shows the lensfree diffraction images of the objects sampled at the CCD for three different incoherent objects. Each diffraction image contains M=355 pixels. Bottom row shows the compressive decoding results of these raw diffraction images to resolve subpixel objects on the chip. For comparison, the inset images in the bottom row show regular reflection microscope images of the objects, which very well agree with the reconstruction results. Note that the red colored regions of the inset images refer to the gold coated area with no transmission, and therefore the reconstructions only focus to the dark regions of the chip (at the center of the inset images) that are nanopatterned. Figure reprinted with permission from [32], copyright (2010), American Institute of Physics.**

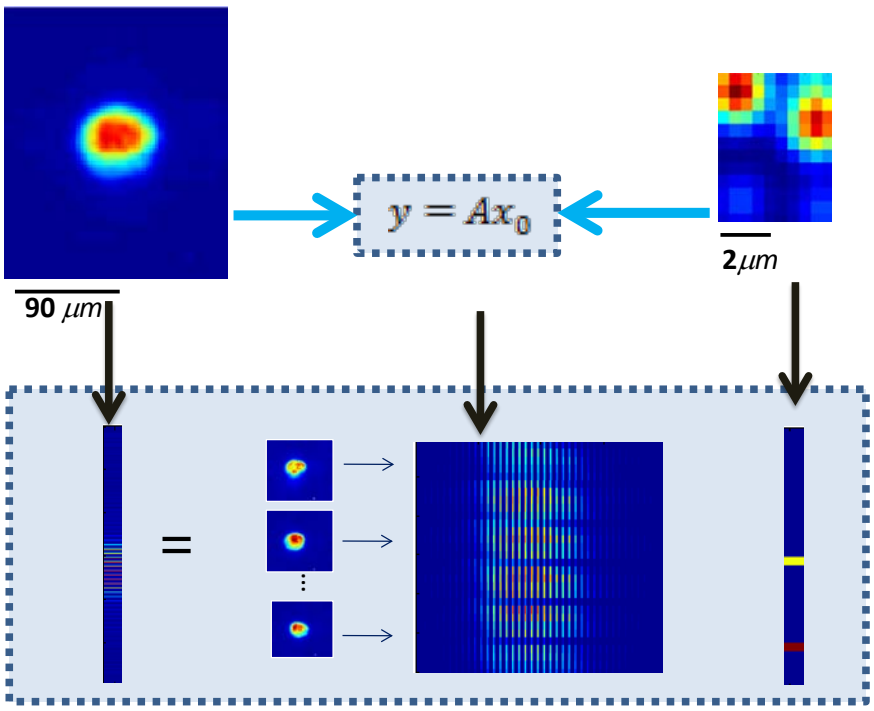


**Figure 2-6 | Recovery process using compressive sensing and lensfree modulated diffraction patterns. The matrices to be used for recovery are replaced with calibration, input, and output matrices of the common CS equation.**

In the image reconstruction or decoding process shown in Fig. 2-5, because M > N, the solution of Eq. 2-5 was an over-sampled problem. Surely, there was no "compression" here. However, the strength of this approach lay in the fact that we could actually achieve almost the same recovery performance using an under-sampled imaging condition, where N > M. To validate this, as indicated in Fig. 2-7, we used many fewer pixels of the diffraction images at the CCD to reconstruct the same N = 120 pixels at the object plane. As evident in the decoding results of Fig.2-7, the sub-pixel object could still be resolved even for M < N. For example, when compared to the M = 355 case of Fig. 2-5, the decoding results of the M = 36 case utilize N = 120 calibration images, each with M = 36 pixels, and a single diffraction image of the object with, again, M = 36 pixels, saving a total of 121 x (355-36) = 38599 pixels from the computation

load. As a result, the decoding time for these images was reduced by ~ 10 fold, achieving ~ 0.1 sec.

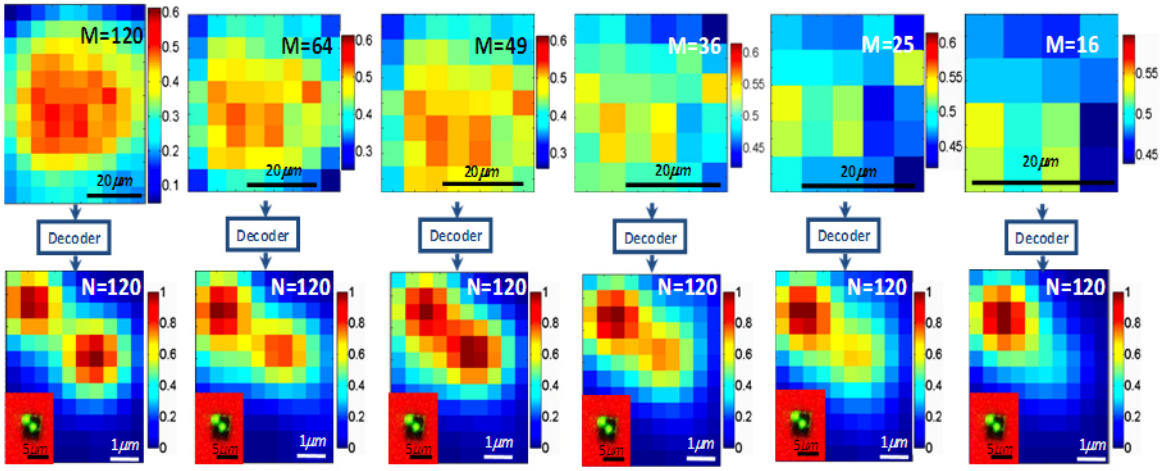


**Figure 2-7 | This is the same as the middle column of Figure 2-5, except for the different M values. This figure indicates that compressive decoding of a sub-pixel object can be achieved from its diffraction pattern at the farfield even for an under-sampled imaging condition where N > M. Therefore, far fewer pixels of the diffraction pattern can enable the reconstruction of sparse incoherent objects on the nanostructured chip. Figure reprinted with permission from [32], copyright (2010), American Institute of Physics.**

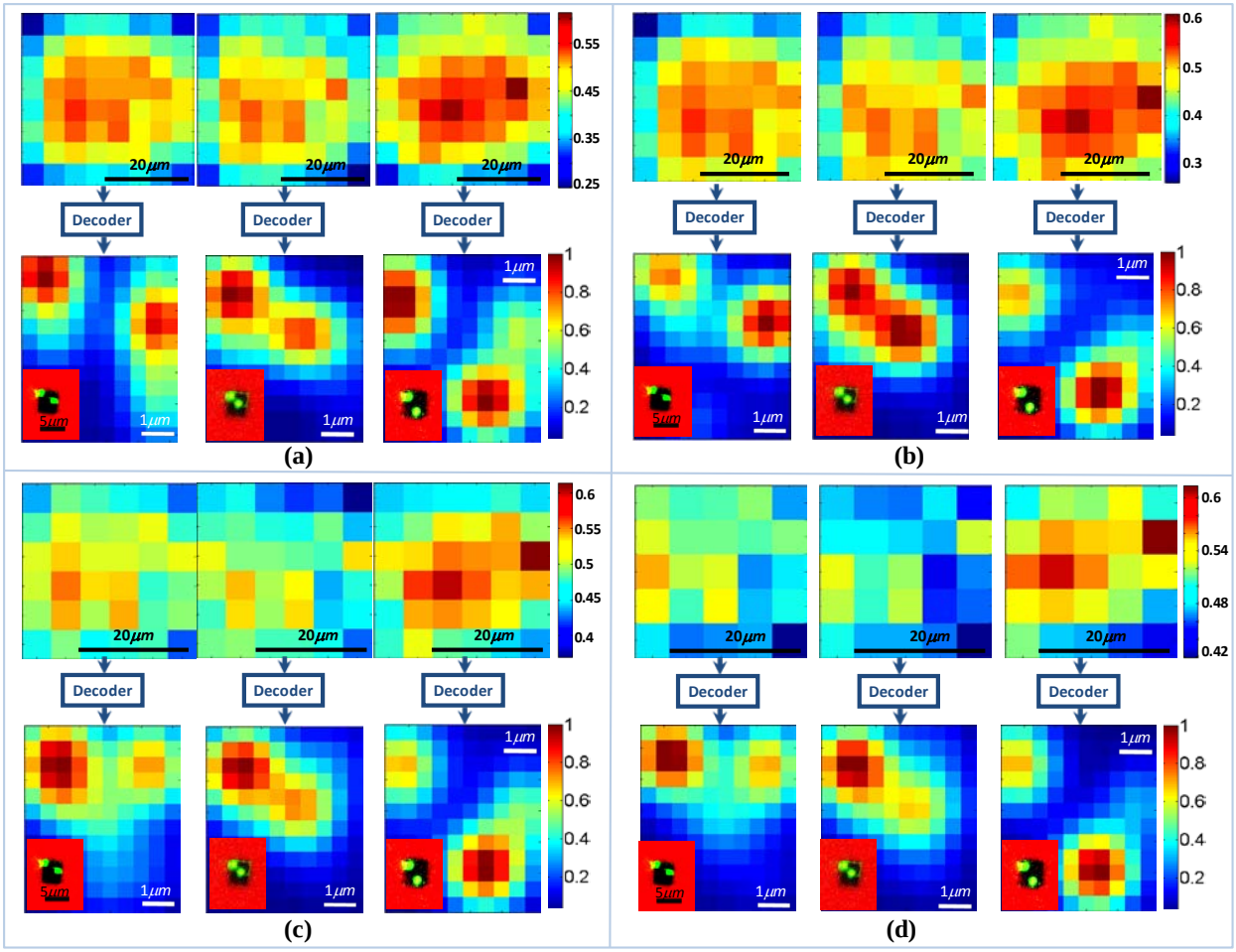


**Figure 2-8 | Recovery results for under-sampled data when using 120 calibration frames for (a) M = 64, (b) M = 49, (c) M = 36, and (d) M = 25 pixels. The top images in each set show the lensfree farfield diffraction pattern, and the bottom images are the recovered images. The red inset images are microscope comparison images, proving the strength of the CS algorithm for proving sub-pixel resolution in cases when the number of known values is less than one third of the unknown elements.**

## 2.5 Lensfree On-Chip Color Imaging Using Structured Substrates[4]

In the previous part, I demonstrated lensfree incoherent imaging on a chip using nanostructured substrates. This on-chip imaging modality involved the spatial modulation of the diffraction

[4] Reprinted with permission from [33], Copyright (2010), American Institute of Physics

pattern for each point at the object plane, which created a calibrated and yet spatially varying lensfree point-spread function (PSF) between the object and the sensor planes. In this part, I will discuss sub-pixel color imaging capability in lensfree incoherent on-chip microscopy. If this spatial modulation is color sensitive (as one would observe in, e.g., plasmonic substrates), then a multicolor incoherent object on the chip could be imaged by calibrating the PSFs of the nanostructured chip at three major wavelengths, corresponding to red, green, and blue, to decode the objects' diffraction patterns into a true-color lensfree image. While this would be feasible by designing, for example, appropriate plasmonic nanostructured substrates, such a color-sensitive resonant transmission behavior would potentially be affected by the presence of the objects on the chip, which could make the lensfree PSFs of the structured substrate object dependent. As this is an undesirable feature for a microscope in general, instead of taking this plasmonic approach, we used a color sensor-chip for recording the lensfree diffraction patterns of multicolor objects. This opto-electronic sensor chip had red, green, and blue (RGB) filters installed at the pixels, such that each period contained one red and one blue pixel, together with two green pixels, to form a repeating RGB pattern across the sensor's entire active area. With this configuration, the spatially varying PSFs of a nanostructured substrate exhibited color sensitivity that was then independent of the object or its near-field, such that an *arbitrary* multicolor incoherent emission from the object plane could be decoded into three distinct colors (RGB), yielding a lensfree color image at the sub-pixel level. This digital imaging approach would be especially important to create compact fluorescent on-chip microscopes that can simultaneously image various colored fluorescent probes [33].

## 2.6 Experimental Setup and Colorful Image Recovery Results

To confirm this novel approach experimentally, we used the structured metallic thin-film slab that was used in monochrome imaging. Fig. 2-9 schematically presents the experimental setup. The incoherent light emitted from a multicolor object is transmitted through the nanostructured substrate and propagates a vertical distance of ~ 0.15 mm to be sampled by an RGB opto-electronic sensor array (i.e., a charge-coupled device (CCD-Kodak, KAF 8300, pixel size: 5.4 µm). Due to the color filters installed on the pixels, each sampled lensfree diffraction image was actually composed of three raw images corresponding to red, green, and blue channels. These lensfree RGB diffraction images, along with the calibration data of the nanostructured chip, were used to reconstruct a multicolor image of the object on the chip.

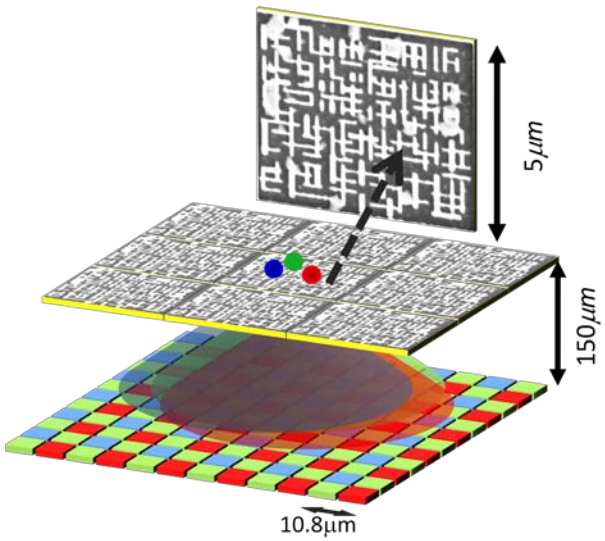


**Figure 2-9 | Schematic diagram of the lensfree incoherent color imaging platform is shown. This setup achieves subpixel level color resolution based on spatial modulation that is introduced using nanostructured substrates. Notice that the diffraction pattern of a multicolor subpixel object that is sampled at the detector plane unavoidably loses its original colors, which in general makes lensfree color imaging at the subpixel level**

**rather challenging to achieve. Figure reprinted with permission from [33], copyright (2010), American Institute of Physics.**

To calibrate the spatially varying color-sensitive PSFs of the fabricated nanostructured chip, wemeasured the lensfree diffraction patterns of a point source that was scanning the chip surface, as illustrated in Fig. 2-9. This calibration process was repeated for each one of the three filter colors (red, green, and blue), and quite conveniently, needed to be performed only once for each nano-chip. For the calibration point source, we used fiber-coupled light-emitting diodes (at 470 nm, 530 nm, and 670 nm with a bandwidth of ~ 20-30 nm each) focused to a spot size of < 2 μm (FWHM) on the top surface of the nanostructured chip. In these calibration experiments, the detector array was scanned using a Piezo stage controlled by a LabVIEW code. Using a scanning step size of ~ 0.5 μm in both x and y directions, we acquired a total of N = 3 × 120 calibration frames over a 6 μm × 5 μm area of the nanostructured surface. Fig. 2-10 exhibits representative sets of diffraction patterns for each color channel captured for different points on the nano-chip. As expected, these lensfree diffraction images at each color channel were significantly different from one another, validating the spatially varying color-sensitive nature of the lensfree PSF, which is a key feature for achieving sub-pixel color imaging on a chip.

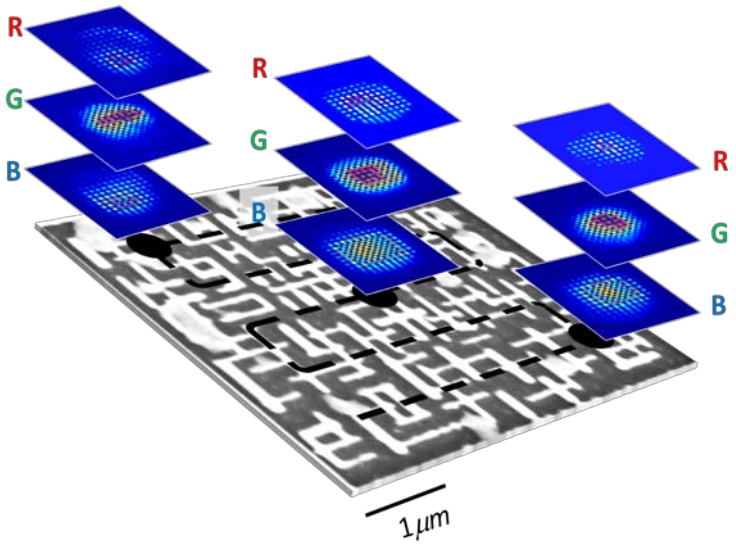


**Figure 2-10 | Schematic representation of the calibration procedure. A point source is scanning the structured surface. The scan is performed for different-colored sources. The figure also depicts various point-spread function images for different colors (*R*, *G*, and *B* stand for red, green, and blue), as indicated by the black spots. Figure reprinted with permission from [33], copyright (2010), American Institute of Physics.**

After this calibration step (which involved the capture of N = 3 × 120 different space-and color-encoded PSFs), to demonstrate the resolving power of this lensfree color imaging modality, we illuminated the same nanostructured chip with a multicolor object containing three spots at red, green, and blue, respectively, that were spatially separated by ~ 2 μm (which implies a sub-pixel object because the pixel period at the CCD chip is 10.8 μm). The results of this lensfree color imaging experiment are summarized in Fig. 2-11. For comparison purposes, conventional reflection microscope images of the same multiobjects are shown in Fig. 2-11(d); these were acquired using a 40X objective lens (numerical aperture: ~0.6). For these sub-pixel multicolor objects, the raw lensfree diffraction patterns that were sampled at the CCD chip are shown in Fig. 2-11(a). Due to diffraction, they were quite broadened, to an extent of ~ 100 μm. Because of the color filters installed at each pixel, these raw images in Fig. 2-11(a) exhibit a

mosaic pattern (also known as the Bayer pattern), but they are normally demosaiced to yield regular color images. The output of this digital demosaicing process is illustrated in Fig. 2-11 (b), images that now indicate an almost uniform white diffraction spot, spanning ~ 100 µm. This was expected since a closely packed set of red, green, and blue spots at the sub-pixel level would look white in the farfield (assuming similar power levels in each color).

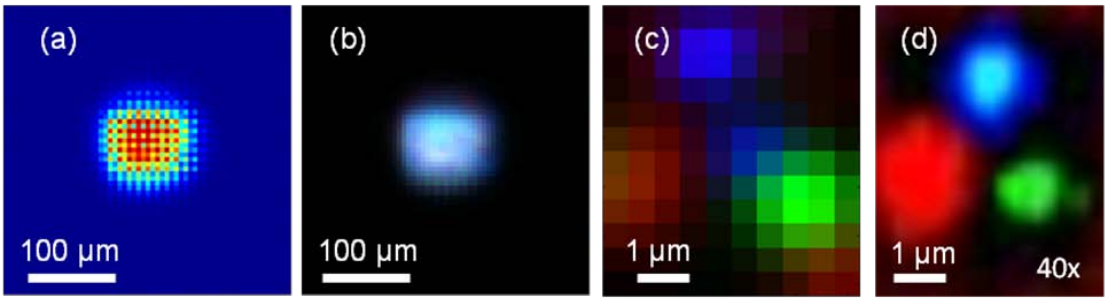


**Figure 2-11 | (a) Images of the scenes captured by the CCD sensor depicted in (d), as captured by the structured-surface lensfree imaging system. (b) Colored images constructed using the raw data from (a), respectively. (c) Reconstructed images using compressive sensing. Figure reprinted with permission from [33], copyright (2010), American Institute of Physics.**

I would like to emphasize that neither Fig. 2-11 (a) nor Fig. 2-11 (b) exhibits any visible sign or trace of the sub-pixel multicolor objects located at the structured surface. While this is true for the bare eye, it is actually feasible, using a compressive-sampling algorithm, to decode the raw lensfree diffraction image of Fig. 2-11(a) into a much higher-resolution image to recover the sub-pixel multicolor object distribution located at the structured chip. The result of this numerical decoding process is illustrated in Fig. 2-11 (c), in which the three distinct sub-pixel sources at each color are now clearly resolved, providing a decent match to the reflection image of the same chip acquired with a conventional microscope (Fig. 2-11[d]).

My experimental demonstration of this lensfree color imaging platform achieved a spatial resolution of ~ 2 µm, which was around five times smaller than the resolution that the pixel

period at the CCD chip (10.8 μm) would normally permit in direct-contact color imaging. We believe that this lensfree computational imaging platform could be quite useful in creating a compact fluorescent on-chip microscope with true-color imaging capability.

The computation time of this decoded image was < 10 sec. using a dual-core processor (AMD Opteron 8218) at 2.6 GHz, which can be significantly improved by employing a graphics processing unit (GPU).

## 2.7 Lensfree Near-Infrared (NIR) Imaging Using Nanostructured Surfaces

In this part, I demonstrate lensfree sub-pixel resolution imaging for the near-infrared regime. We used a pulsed laser lasing at $\lambda = 1.55$ μm due to this tool's availability; however, this technique can be used for resolution enhancement in infrared thermal imaging too. Using sub-pixel resolution in the infrared range has various advantages. For instance, some biological phenomena, such as cancer markers, can become visible in infrared [46]. Also, providing smaller pixel size for IR and NIR cameras is highly desirable due to complexities in reducing the pixel size in this wavelength regime.

Note that turning to higher wavelengths makes fabrication of the nanostructured surface easier and more cost effective, as the limitation on the feature size is looser [47].

## 2.8 Experimental Setup and Fabrication Details

The main differences between the setup used for NIR imaging and the previous setup used for visible light imaging were the image sensor installed in the system and the illumination light source. The NIR image sensor we deployed utilizes a CCD that has been specially treated with a phosphor coating that emits visible radiation when illuminated with wavelengths between 1460 nm and 1625 nm at a cost much lower than that for other detector technologies

(http://www.edmundoptics.com/imaging/cameras). The sensor pixel size is 8.4 μm × 9.8 μm, and there is a 700-μm-thick protective glass layer on the pixel array. For the illumination, we used a pulsed laser with a lasing point wavelength at 1550 nm. We designed and fabricated a dense array of submicron features on a gold-coated substrate that provided unique diffraction patterns for each point of the substrate. The main design mask was based on a digital mask originally designed using a random function generator in MATLAB with a 50% blocking or transmitting ratio. The final mask was milled on a 200 nm gold-coated 150-μm glass substrate using FIB. We placed an infrared illuminating sample on top of the substrate so that the modulated diffraction patterns could be captured by the CCD camera.

To calibrate the nanostructured chip, we used a focused spot of ~ 2.5 μm (FWHM) on the surface of the structured substrate. In these calibration experiments, the detector array was scanned using a Piezo stage controlled by a LabVIEW code. Using a step size of 1 μm for 24 steps in both x and y directions, we acquired a total of N = 576 calibration frames for M = 34200. The large area for farfield patterns resulted from a large gap between the aperture plane and the pixel frame due to a glass protective (~ 700 μm) layer and phosphor coating (~ 6-7μm).

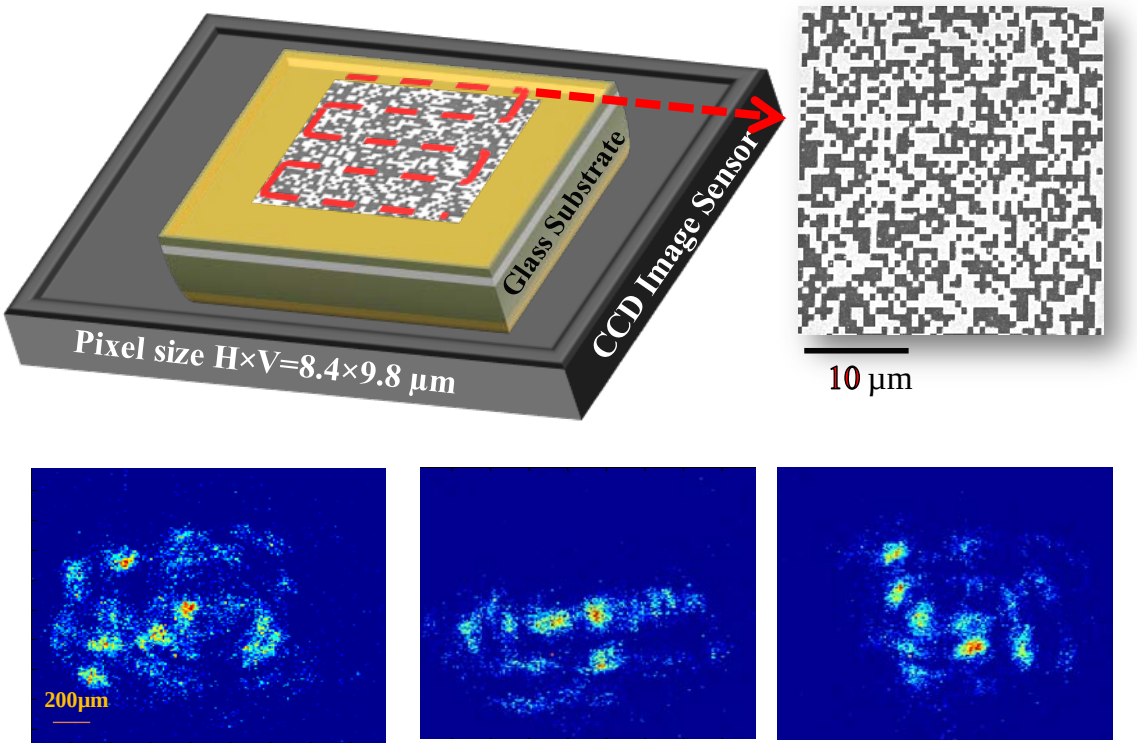


**Figure 2-12 | The top image depicts the structured substrate fabricated for NIR imaging that is placed on top of the CCD pixel array. The bottom images are three samples (out of 576 total) of calibration frames.**

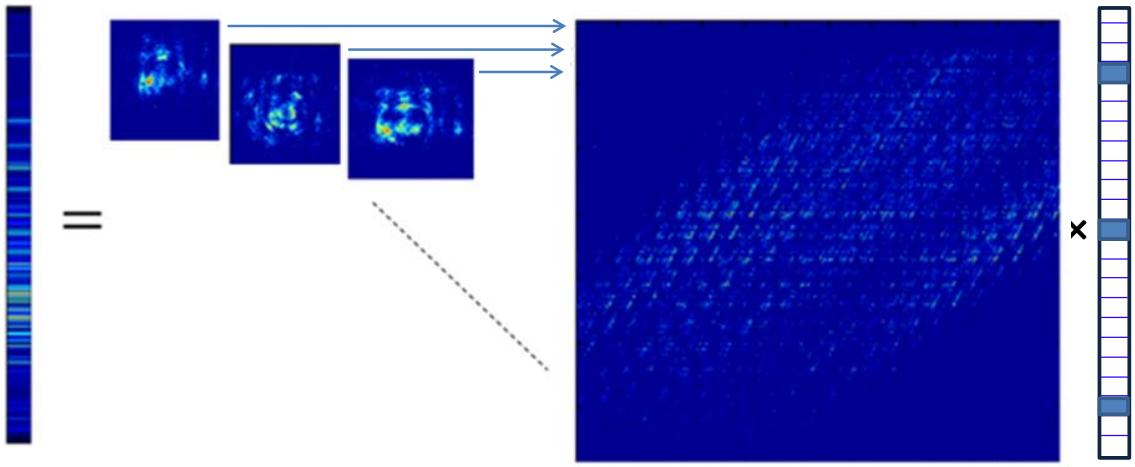

**Figure 2-13 | Calibration frames along with a compressive-sensing algorithm are used to locate and recover the object placed on the image sensor's surface.**

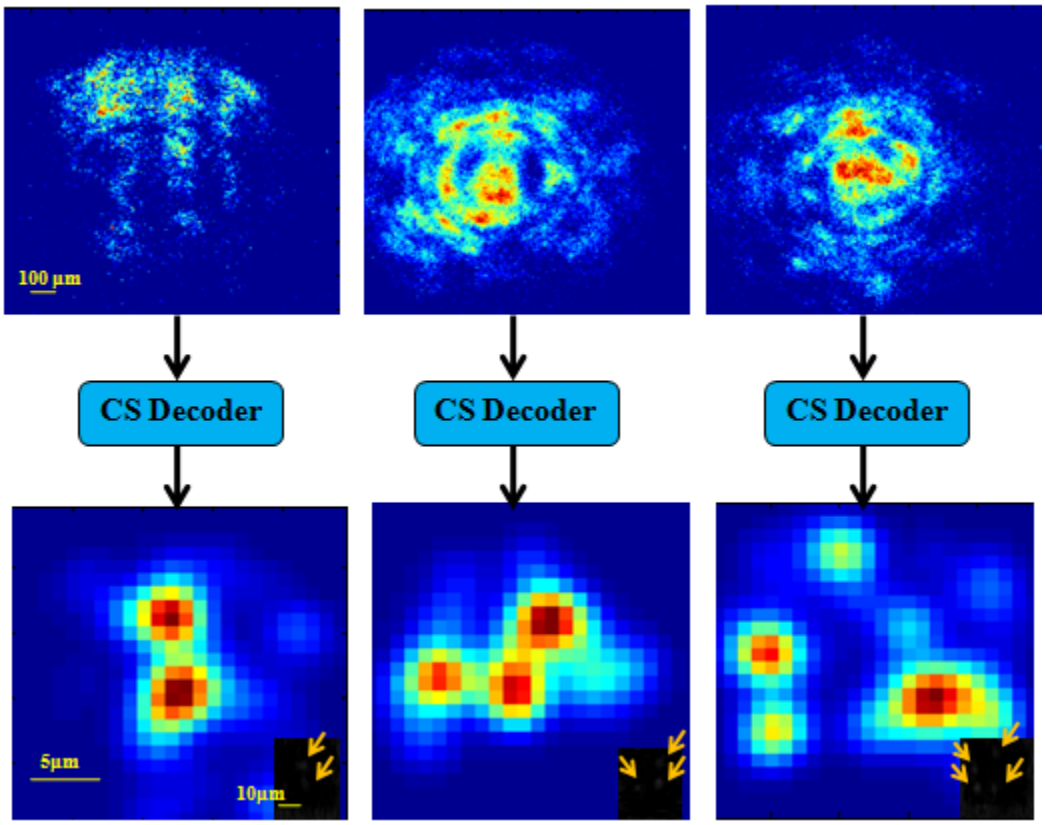


**Figure 2-14 | The real image of the NIR object that was projected on the surface of the CCD image sensor can be recovered (bottom images) through compressive sensing using the diffraction pattern of the object and the lensfree calibration patterns (top images). As shown in the inset image with a black background in the left set of images, the distance between two recovered spots is approximately 6 µm; this validates sub-pixel resolution imaging using the structured substrate technique.**

As you see in Fig.2-14, the spots with a distance around 5-6 µm are clearly resolved. This proves the feasibility of this approach at both visible and near-infrared wavelengths for increasing the pixel density of the sensor array without scanning or a multiframe capturing method [47].

## 2.9 Conclusion

In conclusion, I presented a sub-pixel color imaging scheme using lensfree incoherent on-chip microscopy. We utilized a nanostructured substrate that spatially modulated the farfield diffraction patterns corresponding to each point at the object plane. These lensfree diffraction patterns were sampled using an opto-electronic sensor array, in which the pixels had three different types of color filters (red, green, and blue). To reconstruct an arbitrary multicolor object located on the nanostructured chip, calibration of the spatially varying color-sensitive PSFs of the nano-chip was required.

After this proof-of-concept demonstration, for the next steps, we envision extending the FOV by tiling several of these nano-patterns on the same chip to cover a much larger imaging area. For this task, a periodic chip that repeats an appropriate design of nanostructures in x-y will be sufficient since lensfree incoherent imaging has its own resolution that can spatially separate one period from another if the periods are made larger than, for example, ~ 50 μm.

# Chapter 3 Plasmonic Nano-Apertures for Lensfree On-chip Sensing[5]

## 3.1 Introduction[6]

Over the last few decades, extensive work has been done in building up affinity biosensors, especially for medical and biological applications. An affinity biosensor is a transducer system containing an electrochemical, piezoelectric, or optical mechanism to detect the existence of a selected molecule in an analyte. A variety of affinity biosensors based on optical methods have been implemented. Noteworthy among these are plasmon resonance (SPR) sensors and fluorescence biosensors [49]. Although fluorescence sensors provide a high level of sensitivity, they necessitate a time-consuming and costly labeling process. SPR sensors perform based on a refractive index of samples and provide label-free and real-time detection of biolomolecular interactions [21]. There are several categories of plasmonic sensors, such as those based on the Kretschmann configuration [22] or nanohole array-based biosensors, which have less sensitivity than the Kretschmann configuration and carry the disadvantage of nanofabrication complexity [50]. Several methods have been utilized to increase the throughput of plasmonic sensing devices [27] or to make the platforms more compact [28], but the

[5] Reprinted with permission from [48], Copyright (2010), American Institute of Physics

[6] The content of this chapter has been published in or presented at the following: Khademhosseinieh, B., Biener, G., Sencan, I., Su, T., Coskun, A. F. & Ozcan, A., "Lensfree sensing on a micro-fluidic chip using plasmonic nano-apertures," *Applied Physics Letters* 97 (2010); Khademhosseinieh, B., Sencan, I., Biener, G. & Ozcan, A., "Use of nano-structured surfaces to enable higher resolution detector arrays for lensfree imaging and sensing on a chip" (invited talk), Nanoelectronic Devices for Defense and Security Conf. (Nano DDS), New York, USA, 29 Aug.-1 Sept. 2011; Khademhosseinieh, B., Biener, G., Sencan, I., Su, T., Coskun, A. F. & Ozcan, A., "Plasmonic nano-apertures for lensfree on-chip sensing" (paper #CTuZ4), in proceedings of OSA Conf. on Lasers and Electro-optics (CLEO '11), 1-6 May 2011, Baltimore, MD, USA; Khademhosseinieh, B., Biener, G., Sencan, I., Su, T., Coskun, A. F. & Ozcan, A., "Lensfree sensing on a chip using plasmonic nano-apertures" (paper # 8024-8), SPIE Defense, Security, and Sensing Conf., 25-29 April 2011, Orlando, FL, USA.

throughput was not scaled up to the plasmonic sensing area without the scanning process. This issue becomes critical when there is an enormous need for a compact and high-throughput platform capable of rapidly analyzing different cellular and chemical processes occurring in one sample of a biological liquid.

In this chapter, I introduce a new compact and lensfree plasmonic sensing platform capable of providing high-throughput detecting capability by means of deploying a particular design of nanoslits in a lensfree system. Our proposed sensing modality has a platform similar to the one utilized in a nanostructured substrate for lensfree imaging, as introduced in Chapter 2. The lensfree diffraction patterns of that metallic nanostructured substrate are sensitive to the refractive index of the dielectric material inside and around the subwavelength features; therefore, when the patterns are properly designed, the analogous structure can be used to track the permittivity change of the dielectric material. As with the imaging platform that included no lens in the optical path, far-field diffraction patterns overlap each other on the image sensor plane. The overlapped patterns cannot be separated with the compressive algorithm due to the coherency of illumination light that hits the aperture plane; instead, they need to be processed, using phase recovery techniques, to back-propagate the optical fields to an arbitrary depth, creating digitally focused complex transmission patterns.

At the beginning of this chapter, I will talk about fundamentals of surface plasmons and their impact on light transmission through nanoapertures. Afterwards, the new lensfree plasmonic sensing platform will be introduced. Initial results confirming the refractive index change with a precision of $2 \times 10^{-3}$ have been obtained in both far-field patterns and segregated near-field ones close to the aperture plane.

## 3.2 Surface Plasmons

The electrons on a metal surface can show harmonic fluctuations called surface plasmons. Their existence has been both theoretically and experimentally proved. These charges can be localized to within a short distance from the surface and show maximum electric field amplitude at the boundary between the metal and surrounding medium. As shown in Fig. 3-1, the electric field oscillation of plasmons existing in the interface of two media can be described as $\vec{E} = \vec{E}_0^{\pm}\exp\left[+i(k_x x \pm k_z z - \omega t)\right]$. In this equation, $k_z$ has an imaginary form that causes exponential decay in the direction perpendicular to the surface [22].

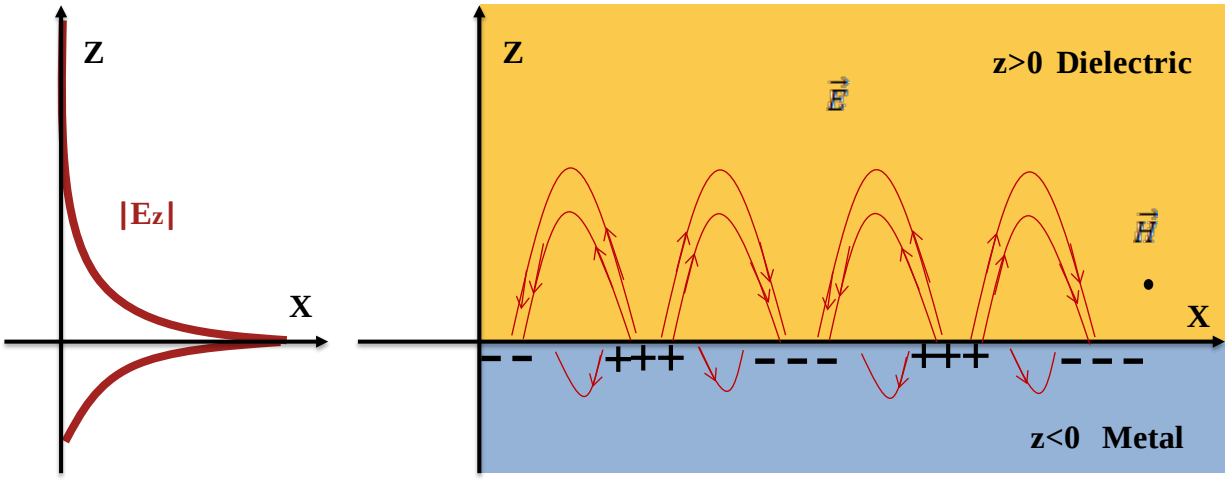


**Figure 3-1 | This shows the electric field of surface plasmons, which are bound to the interface between the metal and dielectric layer and decay exponentially as they get farther from the surface [51].**

When Maxwell equations are solved with the boundary conditions [22] that the dielectric function of the dielectric layer is $\varepsilon_{r2}$ and that a complex value for the metal layer complex dielectric permittivity value is $\varepsilon_{r1}$ $(\varepsilon_{r1} = \varepsilon_{r1}' + i\varepsilon_{r1}'')$ with $\varepsilon_{r1}'' < |\varepsilon_{r1}'|$ , the complex value for the lateral component of wave vector ( $k_x$ ) can be obtained as

$$k'_x = \frac{\omega}{c}\sqrt{\left(\frac{\varepsilon_{r1}'\varepsilon_{r2}}{\varepsilon_{r1}'+\varepsilon_{r2}}\right)} \tag{3-1}$$

$$k''_x = \frac{\omega}{c}\sqrt{\left(\frac{\varepsilon_{r1}'\varepsilon_{r2}}{\varepsilon_{r1}'+\varepsilon_{r2}}\right)^3}\frac{\varepsilon_{r1}''}{2(\varepsilon_{r1}')^2} \tag{3-2}$$

In the case that we are searching for plasmon modes that are bound to surface, we search for an imaginary value for $k_z$ and real $k'_x$, and it is required to have a negative value for $\varepsilon_{r1}'$ and that $|\varepsilon_{r1}'| > \varepsilon_{r2}$. This condition can be satisfied in a real metal in optical frequencies [22].

The Drude model [22], [52], which relates optical properties of metals to their atomic properties by treating metal as a gas of electrons, has been used in this equation to obtain value metal permittivity. Using this model, it can be shown [22] that the frequency-dependent complex permittivity of metals ($\varepsilon = \varepsilon' + i\varepsilon''$) in optical frequencies can be interpreted as

$$\varepsilon(\omega) = 1 - \frac{\omega_p^2}{\omega^2 + i\Gamma\omega} \tag{3-3}$$

where $\omega_p$ is the volume plasma frequency depending on the free electron density in metal, and Γ in relative to the damping factor of collisions between electrons and

$$\omega_{p=}\sqrt{\frac{ne^2}{m\varepsilon_0}} \tag{3-4}$$

where *n* is the number of free electrons in metals per volume and *m* is the efficient electron mass [52].

There is an enhancement mechanism defined as the ratio between the intensity of the surface plasmon wave and the illumination wave, and it reaches its maximum level when the reflection from the metal surface is at the minimum. The amount of the enhancement factor for the magnetic field can be expressed as

$$\left|\frac{H_{sp}}{H_{inc}}\right|^2 = \frac{\varepsilon_{r2}}{\varepsilon_{r0}}\left|\frac{E_{sp}}{E_{inc}}\right|^2 = \frac{\varepsilon_{r2}}{\varepsilon_{r0}}T_{max}^{el}\,, \tag{3-5}$$

where

$$T_{max}^{el} = \frac{1}{\varepsilon_{r2}} \frac{2|\varepsilon'_{r1}|^2}{\varepsilon''_{r1}} \frac{a}{1 + |\varepsilon'_{r1}|} \tag{3-6}$$

and

$$a = \sqrt{|\varepsilon'_{r1}|(\varepsilon_{r0} - 1) - \varepsilon_{r0}} \tag{3-7}$$

In these equations, $H_{sp}$ ($E_{sp}$) refers to the magnetic field (electric field) phasor of surface plasmons and $H_{inc}$ ( $E_{inc}$ ) is that of incident light illumination. For instance, if $\varepsilon_{r1} = 1$ (vacuum or air), $\varepsilon_{r0} = 2.2$ (quartz), and illumination wavelength λ = 600 nm, the enhancement factor for electric field intensity on gold surface is about 30 [22].

Surface plasmons can exist on a surface of a curved or scattering object whose edges or local corrugations can be approximated by tiny spheres. This effect is known as localized surface plasmon resonance, or LSPR. The polarization of a sphere (radius *a*) can be shown as [22]

$$\vec{P}(\omega) = \frac{3}{4\pi} \frac{\varepsilon_{r1}(\omega) - \varepsilon_{r0}}{\varepsilon_{r1}(\omega) + 2\varepsilon_{r0}} \overrightarrow{E_0}, \tag{3-8}$$

where $\overrightarrow{E_0}$ is the uniform electric field hitting the sphere whose radius is much smaller than λ ($a \ll \lambda$). This can lead to enhancement of the electric field intensity at the surface of the sphere in the case of having a small value for $\varepsilon_{r1}(\omega) + 2\varepsilon_{r0}$. For a small silver sphere at $\lambda = 350\ nm$ ($\varepsilon'_{r1} \approx -2$ and $\varepsilon''_{r1} \approx 0.28$) . With spheres located in a vacuum ($\varepsilon_{r0} = 1$), we have the enhancement factor for electric field intensity approximately equal to 480 [22].

The enhancement factor is an important characteristic of LSPR, and due to its sensitivity to the refractive index of the surrounding medium, together with its large local amplitude, it can be used for sensing purposes [53], [54]. With LSPR sensing, compared to methods based on plane surface interactions, in cases when the proper particle type and size have been chosen, less

interference between the sensing device and the material has been seen, as has higher detection resolution [24]. The effects of surface plasmons in the interaction of electromagnetic illumination in optical frequencies and subwavelength features, such as thin ($<< \lambda$) dielectric slits in metal thin films, have been discussed and proved before [55]. For instance, a great amount of research has been done to attribute the effect of surface plasmons to transmission through tiny apertures in real metal. It has been shown that light impinging on isolated subwavelength holes in real metal film excites localized surface plasmon modes on the aperture ridge. Their activation results in optical tunneling through apertures and enhanced light transmission in corners and edges [55].

## 3.3 Label-Free Sensing Using Surface Plasmons

As mentioned before, surface plasmon excitation is highly dependent on the refractive index of the medium surrounding the metallic structures. These can be regarded as permittivity sensors because they monitor the electric field interaction with the structures [22]. The most commonly used surface plasmon resonance sensing structure is called the Kretschmann configuration, which requires a p-polarized light (the magnetic field is parallel to the metal surface) to hit the metal-dielectric interface. Based on variation in the dielectric refractive index in the vicinity of the metal surface, the angle of maximum coupling or minimum reflection changes. The effective refractive index of the medium corresponding to the amount of a particular biomolecule can be calculated by either of two methods: by scanning the wavelength and tracking the reflected light at a fixed angle, or by keeping the wavelength fixed using a laser and scanning the angle at which the minimum reflection occurs. If we name the complex dielectric constant of the metal as $\varepsilon_m$and the refractive index of the sample medium as $n_s$ and

that of the prism as $n_p$, in the case that the incident light's wavelength hits the surface where angle θ is λ, the equation expresses the maximum coupling based on the wave vector of incident light is ($\vec{k} = (k_x, 0, k_z)$), where [56]:

$$k_x = \frac{2\pi n_p}{\lambda} sin\theta \approx \frac{2\pi}{\lambda}\sqrt{\frac{\varepsilon_m n_s^2}{\varepsilon_m + n_s^2}} \tag{3-9}$$

As a result, knowing the angle or incident wavelength, we can calculate the unknown refractive index, which has quantification and mass spectroscopy applications [56].

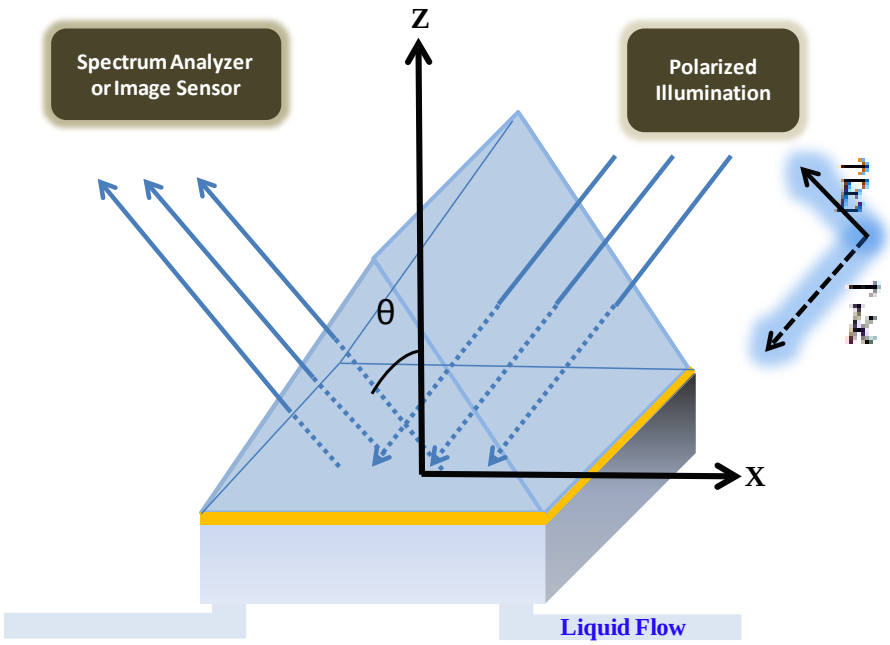


**Figure 3-2 | The reflected light intensity in the total internal reflection condition is dependent on the total amount of biomolecules attached to the metal-dielectric interface, which can be used as a sensing tool for excistingand quantifying biomolecules [26].**

Another group of plasmonic optical sensors are subwavelength structures, which can be single or array-based components that show extraordinary transmission phenomena. Because these components are highly sensitive to the refractive index surrounding the medium, they can

be applicable for sensing purposes [26], [57], [58]. The effect of surface plasmons on enhanced transmission from a single subwavelength hole or an array of them has been discussed in literature [26], [57], [59]. Though a single subwavelength aperture is sensitive to the refractive index and can be regarded as a sensing element, low transmission intensity makes it an unsuitable tool for a complete sensor.

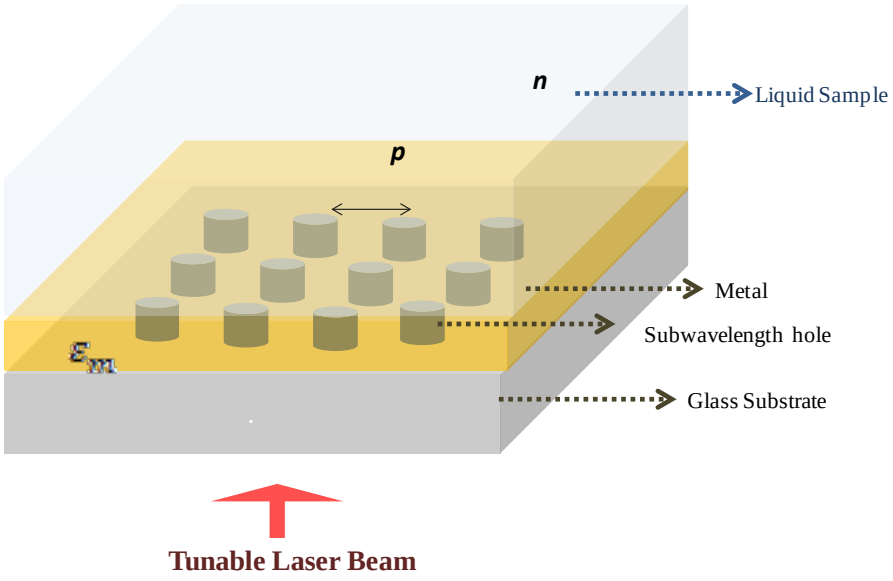


**Figure 3-3 | Tunable laser light exciting surface plasmons in a 2D array of subwavelength holes in the vicinity of a liquid sample. The light transmission from apertures (detected after modulation by aperture) is highly sensitive to plasmonic waves affected by the liquid sample. The refractive index was used to detect the liquid permittivity change [60].**

The development of a state-of-the-art fabrication technique for subwavelength structures using nanoimprinting, self-assembly, and E-beam lithography has helped make new designs feasible.

## 3.4 Lensfree Onchip Sensing Using Plasmonic Nanoapertures

In this part, I introduce an alternative technique for using metallic nanoapertures as optical sensing elements on a chip [48]. In this approach, as opposed to in the prior art, lensfree diffraction patterns of plasmonic nanoaperture arrays located on a microfluidic chip were utilized for sensing. For this purpose, we used spatially incoherent quasimonochromatic illumination, which picked up partial spatial coherence during its propagation that was sufficiently large (e.g., 14 μm x 14 μm; see Fig. 3-4) to illuminate each nanostructured aperture region coherently. Under this illumination condition, the coherent diffraction pattern of each nanoaperture region could be sampled using an optoelectronic sensor array, for example, a CCD or CMOS chip. This lensfree pattern was then digitally processed to retrieve the missing phase of the optical diffraction rapidly, enabling back-propagation of the fields to an arbitrary depth below the nanoaperture plane [3], [39]. When the plasmonic apertures were suitably designed, these lensfree diffraction patterns reconfigured their transmission behavior in response to the local refractive index surrounding the apertures' near-field. Therefore, when these reconstructed diffraction patterns were cross-correlated, lensfree on-chip sensing of minute local refractive index changes was feasible.

A major advantage of this lensfree on-chip sensing platform over existing approaches is that it significantly increases throughput since the entire active area of the optoelectronic detector (e.g., a CMOS chip) can now be utilized with unit magnification (see Fig. 3-4). This makes it feasible to multiplex literally thousands of plasmonic aperture arrays on a standard CMOS chip with an active detector area of, for instance, > 20-100 $mm^2$, which could be especially useful in designing label-free DNA or protein microarrays. Furthermore, this platform's lensfree on-chip architecture makes it rather compact and lightweight, which is important in practical

implementations of the same platform for point-of-care and field uses aimed at, for example, various global health challenges including water quality screening and the diagnosis of infectious diseases. Particularly notable is the compatibility of this on-chip plasmonic sensing approach with the recently demonstrated lensfree holographic telemedicine microscopes [3], [61], which would make it possible to put together a more complete solution (involving both lensfree microscopy and on-chip sensing) within the same field-portable telemedicine unit. This could potentially create new opportunities for health-care delivery, especially in resource-limited settings.

## 3.5 Experimental Setup

To implement the lensfree on-chip sensing architecture discussed above, we chose to work with a plasmonic aperture-array design [62] composed of *varying* widths of sub-wavelength apertures/slits that spanned an area of ~ 14 μm x 14 μm, as illustrated in Fig. 3-4. A similar nanoaperture array has been previously utilized to design planar lenses by exploiting the linear relationship between the width of the sub-wavelength slit and the phase of the transmitted optical field [62]. It has been shown that the phase delay caused by each aperture is dependent on each aperture's width as well as the refractive index of the material surrounding the apertures.

In the on-chip sensing implementation for this research, the function of this array of sub-wavelength slits with varying widths was to introduce different diffraction patterns as a function of the local refractive index. This plasmonic structure (see Fig. 3-4) was fabricated using focused ion-beam milling (FIB - NOVA 600) on borosilicate cover slips (150 μm thick) coated with an ~ 200-nm gold layer using electron beam metal deposition (CHA Mark40, UCLA Nanofab). The prepared chip was then used as the bottom substrate of a custom-designed microfluidic device, as

illustrated in Fig. 3-4,5. The liquid samples having different refractive indices were flushed into the microfluidic chamber to interact with the near-field of the nanoapertures by means of an automated syringe pump.

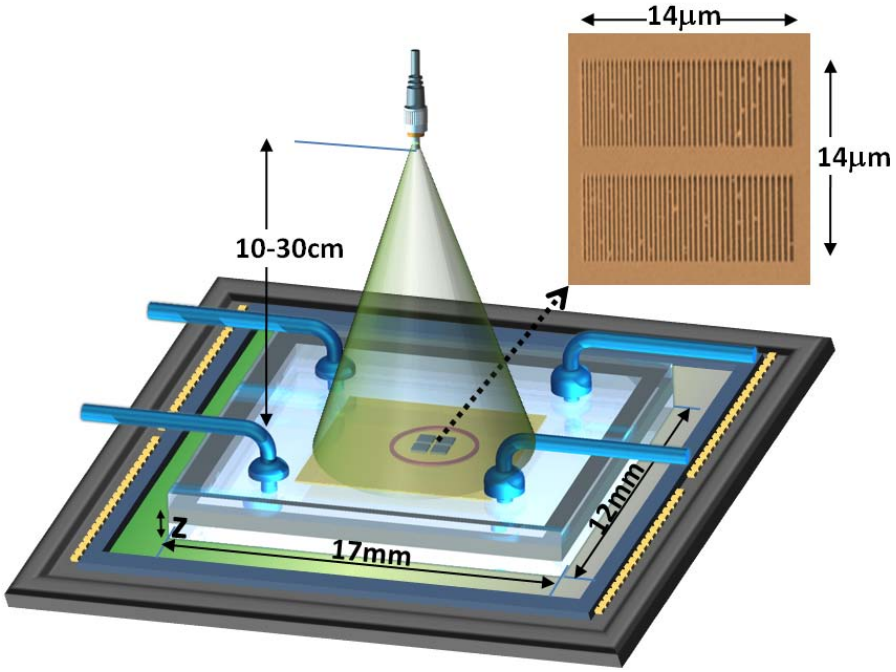


**Figure 3-4 | Lensfree on-chip sensing setup. A plasmonic nanoaperture array, as shown in the SEM image at the top right corner, was illuminated with a quasimonochromatic source, e.g., a 550-nm center wavelength with a 20-nm bandwidth located ~ 10–30 cm away from its surface. The lensfree transmission pattern of this plasmonic structure was sampled by a CMOS chip placed at z ~ 1 mm away from the aperture plane. The yellow surface indicates the detector active area, which was ~ 6 × 4 mm$^2$. The plasmonic nanoaperture array shown above was composed of uniformly spaced slits, each with a length of 6 m, where the slit width varied from left to right between ~ 80 and ~ 200 nm in discrete steps of ~ 20 nm. The physical gap between two neighboring slits was kept constant at ~ 200 nm. Figure reprinted with permission from [48], copyright (2010), American Institute of Physics.**

Lensfree diffraction patterns corresponding to each refractive index value were continuously captured on a chip at a frame rate of ~ 2-3 fps, using a CMOS image sensor while

the liquid was flowing through the microfluidic channel (see Fig. 3-4). The illumination was achieved using a monochromator at 550 nm with a spectral bandwidth of ~ 20 nm, which indicates that a standard light-emitting diode could also be used for both spatial and temporal coherence properties. We also used an inexpensive plastic polarizer in front of the illumination source to create a linear polarization that was orthogonal to the slit direction. This ensured that the transmitted fields from the plasmonic nanoapertures contained only a single polarization component, which was important for the phase recovery steps, as will be outlined later on. This polarization behavior was also confirmed through finite-difference time-domain (FDTD) simulations.

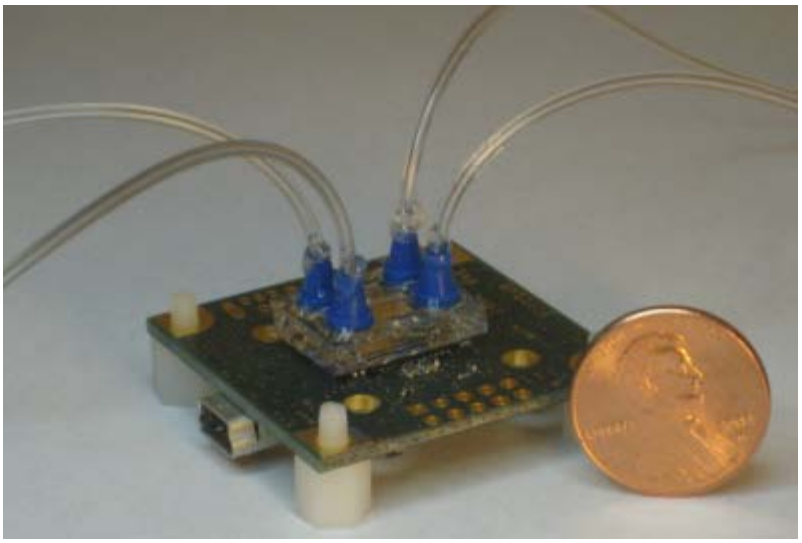

**Figure 3-5 | The microfluidic device whose bottom surface contains the apertures is placed directly on a CMOS image sensor array. The CMOS image sensor is connected to the computer via a micro-USB cable.**

For the liquid needed to validate the lensfree platform, we used saltwater with well-controlled concentrations such that the exact value of the liquid refractive index could be extracted from a look-up table [63]. In Figures 3-8 (a, b, c), the top left images illustrate the lensfree diffraction patterns of the nanoaperture array (sampled at z = 1100 μm, as shown in Fig.

3-4) for three different refractive index values respectively: n = 1.333 [corresponding to deionized (DI) water], n + 3 x $10^{-3}$, and n + 5 x $10^{-3}$. To better quantify the numerical differences among these lensfree diffraction patterns and relate them to refractive index changes ( $\Delta$n) within the microchannel, we calculated 2D cross-correlation coefficients between the first lensfree pattern (corresponding to DI water) and the rest of the acquired diffraction images. In Figure 3-9(a), the bottom left plot illustrates the results of these cross-correlation calculations with a dotted blue curve for ~ 2000 consecutive lensfree diffraction patterns, which were captured while the refractive index within the microchannel was changed according to the following discreet steps:

(1) n = 1.333, (2) n + 3 x $10^{-3}$, (3) n + 5 x $10^{-3}$, (4) n + 3 x $10^{-3}$, (5) n = 1.333.

The solid black curve in the same figure, 2(a), also illustrates a running average of the cross-correlation coefficients for a window size of ~ 50 frames (corresponding to an image acquisition time of < 4 sec.). As illustrated in these results, by recording the lensfree diffraction patterns of this plasmonic aperture array on a compact chip, we was able to track refractive changes as small as $\Delta n = 2 \times 10^{-3}$ faithfully. To further validate the results, we also performed FDTD simulations of the same plasmonic structure, the results of which are summarized in Fig. 3-9. According to these FDTD simulations, the far-field lensfree diffraction patterns of the nanoaperture array closely matched the experimental results presented in Fig. 3-8(a, b, c). Furthermore, the same FDTD results also indicate that, as desired, the response of the 2D cross-correlation coefficient of these lensfree diffraction patterns was linear over a large refractive index range spanning from 1.33 to 1.35.

While these experimental and FDTD simulation results both demonstrate the useful sensitivity of the proposed lensfree on-chip sensing scheme, there is still room for further

improvement that can be implemented by utilizing more advanced digital processing of these diffraction patterns. In particular, due to the plasmonic aperture array's lensfree operation, the sampled transmission patterns spread over a large area on the sensor chip. Although this had no negative consequences for a low number of spots on the same chip, it would create significant limitations as one aims to increase the density and hence the throughput of sensing. In other words, as more and more independent plasmonic spots are placed on the same chip (for a label-free DNA or protein microarray sensing design), their lensfree diffraction patterns will start to overlap with each other at the detector plane, which will degrade the sensitivity of the lensfree sensing platform.

To mitigate this problem and increase the density of the sensing spots on the same microfluidic chip, we used an iterative phase recovery technique [3], [39], [61] to reconstruct the complex wave corresponding to the transmission pattern of each nanoaperture array. In this numerical approach, we treated the detected lensless pattern as the intensity of a complex optical wave whose phase was lost during the image acquisition. To recover this lost phase, we started with an arbitrary phase distribution at the detector plane and back-propagated this complex wave to the plasmonic aperture plane [64].

## 3.6 Back-Propagation and the Gerchberg_Saxton Phase Recovery Algorithm

The Gerchberg_Saxton algorithm [64] was deployed to reconstruct the phase distribution utilizing intensity measurements. In this case, we captured intensity distribution over the image sensor plane and aimed to reconstruct the field distribution on the nanoaperture plane. For this purpose, it was necessary to apply the recovery algorithm in an iterative form; this process involved propagating and back-propagating over large distances. One accurate way to perform

wave propagation in a linear system when the distance from the observation plane to the original field distribution plane is larger than a wavelength is by using the Rayleigh-Sommerfield diffraction integral. If, as shown in Fig. 3-6, the field distribution in the original field plane is $E_1(x_1, y_1, 0)$ and that of the far-field plane with distance $z$ from the first plane is $E_2(x_2, y_2, z)$, we can relate these two complex field distributions as [7], [65]

$$E_2(x_2, y_2, z) = \int_{-\infty}^{\infty}\int_{-\infty}^{\infty} E_1(x_1, y_1, 0)\frac{\exp(i2\pi r_1/\lambda)}{r_1}\frac{z}{r_1}\left(\frac{1}{2\pi r_1}+\frac{1}{i\lambda}\right)dx_1 dy_1\,, \tag{3-10}$$

where $r_1$ is the distance between each two points in two planes:

$$r_1 = \sqrt{(x_2-x_1)^2+(y_2-y_1)^2+z^2}\,. \tag{3-11}$$

The integral can be regarded as a two dimensional convolution form of two functions,

$$h(x, y, z) = \frac{\exp(i2\pi r/\lambda)}{r}\frac{z}{r}\left(\frac{1}{2\pi r}+\frac{1}{i\lambda}\right) \tag{3-12}$$

$$E_2(x_2, y_2, z) = h(x, y, z) * E_1(x_1, y_1, z)\,, \tag{3-13}$$

by assuming

$$r = \sqrt{x^2+y^2+z^2}. \tag{3-14}$$

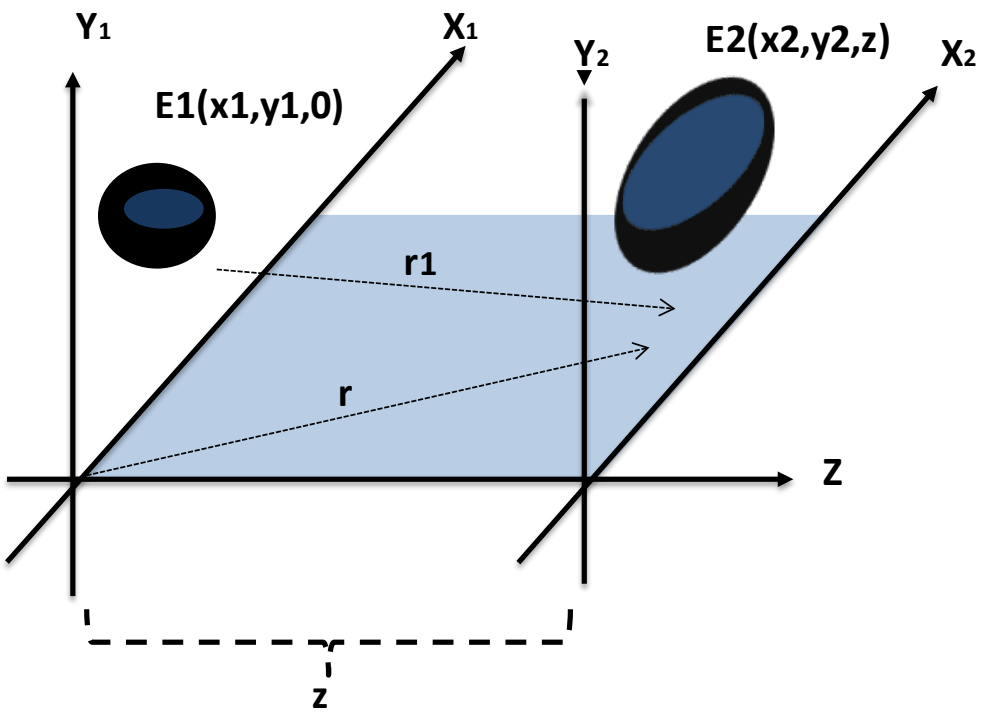


**Figure 3-6 | Far-field propagation of the object field (E1(x1, y1, 0)) from (X1, Y1, Z1) plane to field distribution E2(x1, y1, 0) in (X2, Y2, Z2).**

Based on the relation between convolution and the Fourier transform, we can rewrite the integral equation as

$$E_2(x_2, y_2, z) = F^{-1}\{F\{h(x, y, z)\} \times F\{E_1(x_1, y_1, 0)\}\}. \quad (3\text{-}15)$$

The Fourier transform of *h* function can be obtained with

$$F\{h(x, y, z)\} = \exp(i2\pi f_z z), \quad (3\text{-}16)$$

where $f_z$ is defined as

$$f_z = \begin{cases} \sqrt{\lambda^{-2} - f_x^2 - f_y^2} & when\ \ f_x^2 + f_y^2 \geq \lambda^{-2} \\ 0 & when\ f_x^2 + f_y^2 < \lambda^{-2} \end{cases} \quad (3\text{-}17)$$

and where $f_x$ and $f_y$ are frequencies corresponding to *x* and *y* in the Fourier domain [7], [65].

Thus, the calculation is easier and faster if we obtain the Fourier transform of field distributions

before propagating so that we can multiply the transformed expression to free space transfer function in the Fourier domain, instead of solving a convolution integral in the space domain.

The following summarizes the steps for utilizing the modified form of Gerchberg_Saxton phase recovery algorithm [3], [61]:

1- The Fourier transform of the amplitude distribution (with an initial value for phase distribution) that is captured by the image sensor.
2- Back-propagate the field distribution by multiplying to the *conjugate* free space propagation function exp $(i2\pi f_z z)^*$= exp $(-i2\pi f_z z)$.
3- Inverse Fourier transform of the object plane field distribution and multiply it by a zero-one mask obtained by knowing the size of the arrays of nanoapertures. This step should be done in order to enforce the constraint in the sensor plane. This step provides zero intensity in the areas out of the aperture array.
4- Fourier transform of the field distribution after the masking process.
5- Propagate the transformed field distribution by multiplying the Fourier transform of the field distribution to exp $(i2\pi f_z z)$.

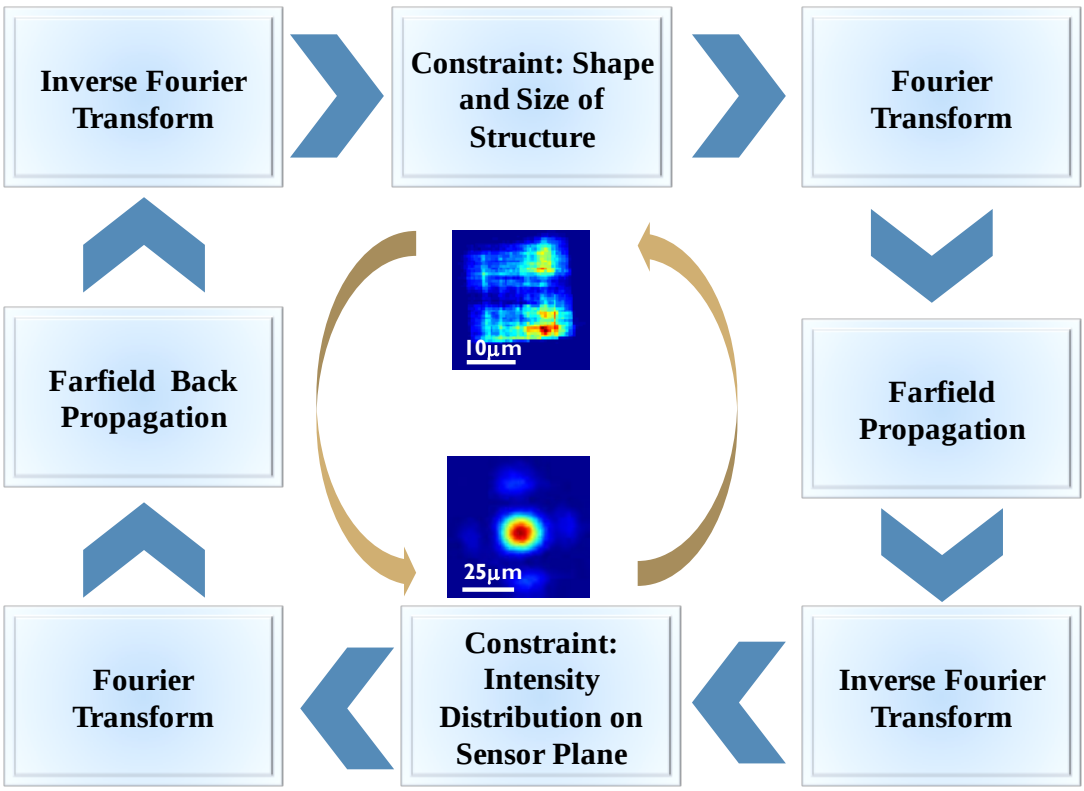


**Figure 3-7 | Block diagram of the iterative algorithm for recovering the field distribution in the aperture plane.**

## 3.7 Applying the Modified Gerchberg_Saxton Phase Recovery Algorithm on Lensfree Plasmonic Sensing

Since the physical boundaries of the aperture region (e.g., ~ 14µm x 14 µm in Fig. 3-4) were known *a priori*, we could enforce this size information as a spatial filter for the complex fields at the aperture plane and forward-propagate the filtered fields back to the detector plane, where the optical phase then changed to a new 2D function. By replacing the intensity at the detector plane with the measured one and keeping the new phase distribution, we were able to start a new iteration to estimate more accurately the phase of the diffracted field after each cycle. This iterative approach rapidly converged to a unique solution after, typically, 10-15 iterations,

which took < 1 sec., using a standard graphics processing unit.

To illustrate the method's success, Figs. 3-8(d, e, f) demonstrate the iterative reconstruction results of the field intensity at the plasmonic aperture plane using the raw lensfree diffraction patterns shown in Figs. 3-8(a, b, c). Calculating the 2D cross-correlation coefficients among these reconstructed patterns resulted in a new sensing curve, as illustrated in Fig. 3-8(b) in the bottom right plot. Once again, similarly to what is shown in Fig. 3-8(a), we were able faithfully to track refractive changes as small as $\Delta n = 2 \times 10^{-3}$, this time using the reconstructed optical intensity patterns at the aperture plane. The major advantage of this phase-recovery based approach is that it would enable multiplexing more densely packed plasmonic spots such that the overall throughout of on-chip sensing could be significantly increased without affecting the sensitivity of the platform.

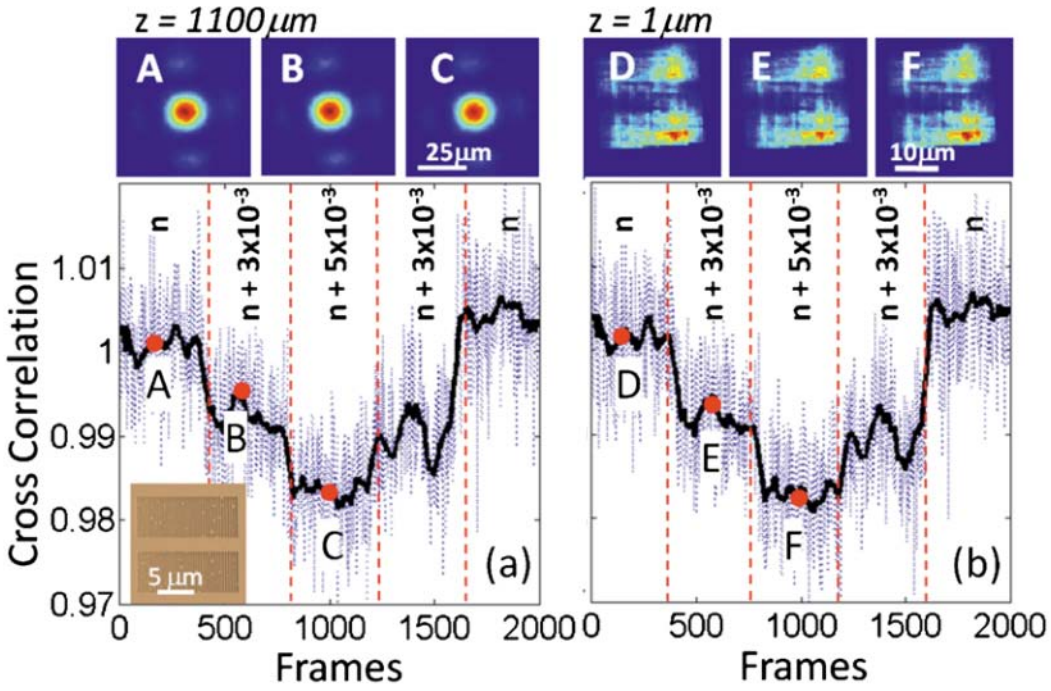


**Figure 3-8 | Cross-correlation coefficients are calculated between the first lensfree transmission pattern and the subsequent patterns for (a) the detector plane (z = 1100 μm), and (b) z = 1-μm reconstruction plane, as**

**illustrated with the blue dotted lines. The same plots also show the running averages of these cross-correlation coefficients over ~ 50 frames (corresponding to < 4 sec of image acquisition), as shown with the black solid lines in (a) and (b). The intensities of the lensfree transmission patterns used in (a) and (b) are normalized to the instantaneous illumination intensity, which is also detected using the same CMOS chip through a large aperture. The initial refractive index of these sensing experiments (n) is 1.333, corresponding to DI water. Top row: Images (a), (b), and (c) illustrate the raw lensfree diffraction patterns of the nanoaperture array at three different refractive indices within the microfluidic channel (n, n + 3 x $10^{-3}$, and n + 5 x $10^{-3}$, respectively), where all the lensfree transmission patterns extend over a width of > 50 μm. Images (d), (e), and (f) illustrate the reconstructed transmission patterns of the same nanoaperture array at z = ~ 1 μm plane, right underneath the aperture region. Figure reprinted with permission from [48], copyright (2010), American Institute of Physics.**

We also conducted FDTD simulations to calculate the field patterns close to the aperture plane. These results, summarized in Fig. 3-9, nicely match the experimental results shown in Fig. 3-8, further supporting my conclusions.

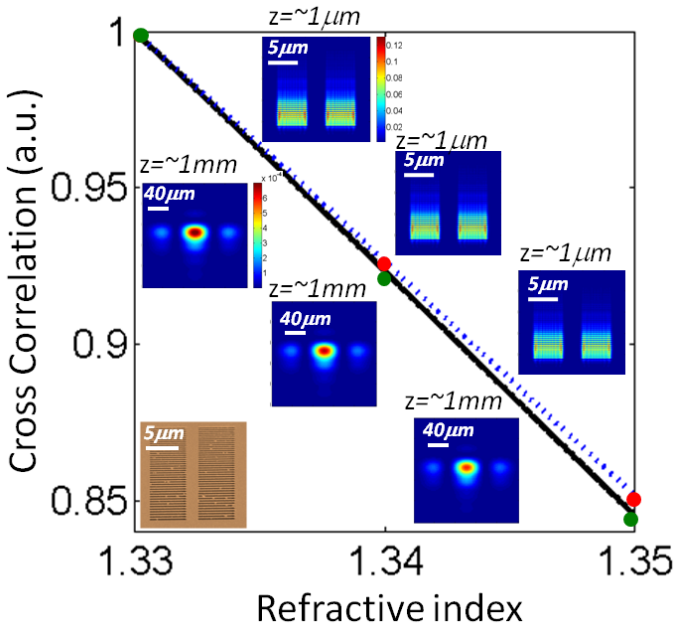


**Figure 3-9 | Based on FDTD simulation results, the cross-correlation coefficients among lensfree transmission patterns of the same nanoaperture array shown in Figs. 3-4 are calculated as a function of the refractive index within the microchannel. These calculations were performed for both z = ~ 1 mm (solid line) and z = ~ 1μm (dotted line) planes. The false color insets depict the 2D transmission patterns for three different refractive index values (1.33, 1.34, and 1.35, respectively), where the upper (lower) ones are calculated at z = ~ 1 μm (z = ~ 1 mm). Figure reprinted with permission from [48], copyright (2010), American Institute of Physics.**

Note that it was impractical to obtain a far-field complex field distribution by FDTD, due to the heavy computational load that FDTD carries. As a result, we needed to simulate field distribution in a space close to (~ 1μm from) the aperture plane and propagate the field in the free space to obtain the field distribution on the image sensor plane, using the far-field propagation method (see Eq.3-6). It is rather important to emphasize that the formerly discussed iterative phase-recovery approach worked well even when the diffraction patterns of neighboring plasmonic spots overlapped at the detector plane. See, for example, Figs. 3-8 (d, e, f), which

illustrate that the transmission patterns of the top and bottom aperture arrays were resolved from each other, whereas these normally entirely overlapped at the detector plane, as shown in Figs. 3-8 (a, b , c). In addition to this, as the sensing field of view increased to cover the entire detector active area (e.g., > 20 $mm^2$), the requirements for spatial and temporal coherence of illumination would not change, which is quite important for scaling this platform to extreme throughputs without changing the illumination conditions. In this sense, the operation principles of this phase-recovery approach are quite similar (although not identical) to recently demonstrated partially coherent lensfree holographic telemedicine microscopes [3], [61] for which the lensfree cell holograms over a large field of view cannot coherently interfere with each other due to the limited spatial coherence diameter at the detector plane. The exact value of the spatial coherence diameter in the lensfree platform we used can be precisely tuned by controlling the aperture size of the source or by controlling the propagation distance between the source and the plasmonic aperture planes.

I should note finally that the fabrication imperfections of the plasmonic nanostructures in the design do not constitute a fundamental challenge in this lensfree on-chip sensing approach, since the cross-correlation of the lensfree diffraction patterns of the plasmonic apertures were effectively measured as a function of the local refractive index. This differential correlation measurement makes the scheme robust in the face of potential fabrication imperfections, which is especially important for wide field-of-view implementations of this platform for increased throughput in sensing.

## 3.8 Conclusion

In conclusion, I introduced a lensfree sensing platform on a microfluidic chip using plasmonic nanoapertures. This sensing method provides detection of refractive index differences as low as 0.002. Apart from its sensitivity, such an on-chip sensing modality can also provide a large dynamic range for refractive index sensing. This lensfree approach could be quite useful in the development of label-free microarray technologies because it could multiplex thousands of plasmonic structures on the same chip, which would significantly increase the throughput of sensing. In addition to this, the platform's lensfree on-chip architecture also makes it comparatively compact and lightweight and both these qualities would be significant in practical implementations of this sensing platform for point-of-care and field use related to, for example, various global health objectives including water-quality screening and infectious-disease diagnoses.

# Chapter 4 Lensfree Incoherent Imaging Using Pixel Super Resolution Technique

## 4.1 Introduction

The smallest feature visible with a regular lens-based optical instrument capturing farfield propagating components is limited due to the diffraction of the point-source object. The Abbe diffraction limit states that with the illumination wavelength λ propagating in medium with the refractive index *n,* the smallest spot diameter obtainable for a point-like object in a focal plane is

$$d_r \approx \frac{\lambda}{2nSin(\theta)} \tag{4-1}$$

where $\theta$ is the capturing angle of the lens [66], [67].

This equation shows that the smallest distance between two adjacent features that can be resolved is around half of the illumination wavelength. This amount is often enough to satisfy imaging and diagnosis applications of biological samples, as when distinguishing and counting different blood cells [67]. However, due to imaging systems' physical limitations, such as optical and mechanical noise, we cannot always reach this limit. There has been a great effort to make optical microscopy more powerful and capable of resolving smaller parts of cells and subcellular components. One excellent example of this advancement is confocal microscopy [68], [69], which, because it uses an aperture in the detector plane, can eliminate out-of-focus light and provide high-resolution diffraction-limited images [66].

In addition to diffraction-limited systems, a number of methods have been introduced that push the resolution limit below the diffraction limit and that are generally called *super-resolution*

techniques [66]. Among these methods are ones that use nonlinear illumination or temporally engineered excitation to make features smaller than the diffraction limit. Examples include [66] stimulated emission depletion (STED) microscopy [70], ground-state depletion microscopy [71], saturated structured illumination microscopy (SSIM) [72], photoactivation localization microscopy (PALM) [73], and stochastic optical reconstruction microscopy (STORM) [74].

The super-resolution methods mentioned above rely on lens-based common microscopy technique, and thus, they require complicated, bulky, and expensive systems to beat the diffraction limit. Another process of resolution enhancement that provides higher resolution than what a regular microscopy or a lens-based imaging system can provide is called *pixel super resolution.* This is the core of the imaging technique I will introduce in this chapter. It should be noted that the best resolution achievable with this technique is limited to the diffraction limit and should not be confused with sub-diffraction super-resolution methods in microscopy. Pixel super resolution method is still extremely useful in large field-of-view incoherent imaging, especially fluorescent microscopy.

## 4.2 Pixel Super-Resolution Algorithm

An image detector system is composed of a series of pixels that sample the image projected by optical components, such as lenses. It is always very advantageous to acquire higher resolution since it contains more valuable information. To improve resolution, it is necessary to improve the quality of the optics as well as to decrease the pixel size (i.e., increase the pixel density in a fixed detecting area). There are, however, some drawbacks to decreasing the pixel size. In addition to the technological challenges in fabricating small-pixel-size image sensors, when the pixel size is decreased, the amount of light hitting each pixel is reduced, and thus, the

signal-to-noise ratio (SNR) is degraded. This is mainly due to the fact that the SNR is a parameter that is dependent on the signal strength: having a lower-intensity signal results in having a lower SNR. One solution to mitigate the pixel size limitation in order to obtain an image with higher density is to apply a signal-processing technique that utilizes a series of frames that are shifted spatially in relation to each other. This technique is called *pixel super resolution* (pixel SR) and is a known method in the optics community [14], [75].

SR works by using multiple low-resolution images that are shifted with respect to each other by a fraction of the pixel size of low resolution. In Fig.4-1, the physical pixel is indicated by dark blue borders, while the virtual smaller pixels are represented by the light blue grid. For each horizontal shift $h_k$ and vertical shift $v_k$, the output of the real physical image is obviously a linear super position of the embedded low-resolution (large pixel size) images [14].

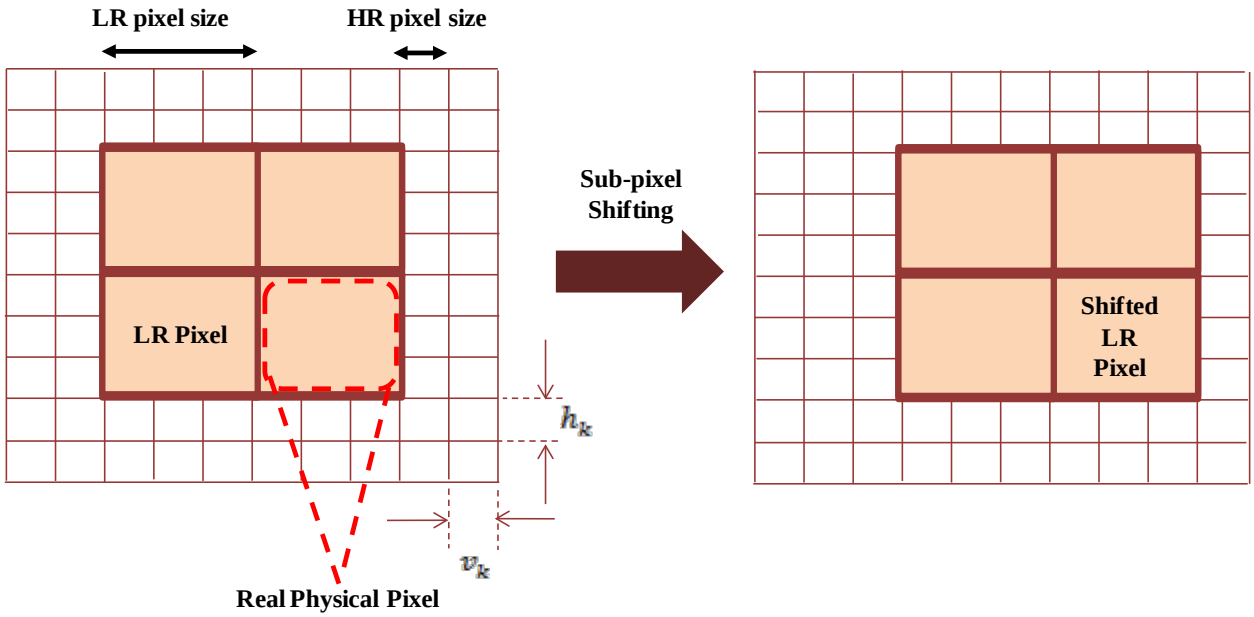


**Figure 4-1 | Covering a grid of HR pixels with bigger LR pixels [14], [75].**

## 4.3 Shift Estimation and Image Registration

To calculate the high-resolution frame from a series of low-resolution ones, an estimation of how much the sub-pixel images shift in relation to each other is needed [76]. The first step is to calculate shifts larger than the size of one pixel. This is necessary because, unlike a sub-pixel shift, a shift that is an integer of the pixel size does not carry any information, and the sub-pixel shift estimation is based on the assumption that all the shifts are very small relative to the pixel size. After this stage, each image is shifted *back* to a degree equal to the number of whole pixels shifted compared to the base image. Consequently, from here on, all shifts can be presumed to be sub-pixel.

We assume that at each shift there are horizontal, vertical, and rotational movements that occur with the center of $x = 0, y = 0$. The shifted image ($\tilde{o}_k$) with respect to the first image ($\tilde{o}_1$) can be written as:

$$\tilde{o}_k(x,y) = \tilde{o}_1(xcos\theta_k - ysin\theta_k + h_k, ycos\theta_k + xsin\theta_k + v_k) \tag{4-2}$$

In the case of very small rotational angles ($\theta$), we can make first-order approximations of sinusoidal functions as follows [76]:

$$sin\theta_k \approx \theta_k \text{ And } cos\theta_k \approx 1 \tag{4-3}$$

By applying the Taylor series expansion, we can then rewrite the former equation as

$$\tilde{o}_k(x,y) \approx \tilde{o}_1(x,y) + (h_k - y\theta_k)\frac{\partial \tilde{o}_1(x,y)}{\partial x} + (v_k + x\theta_k)\frac{\partial \tilde{o}_1(x,y)}{\partial y} \tag{4-4}$$

The unknowns in this equation are $\theta_k$, $v_k$ and $h_k$, and can be calculated by minimizing the error function with respect to each of the parameters:

$$E_k(\theta_k, v_k, h_k) = \sum_{(x,y)\in S}\left(\tilde{o}_k(x,y) - \tilde{o}_1(x,y) - (h_k - y\theta_k)\frac{\partial \tilde{o}_1(x,y)}{\partial x} - (v_k + x\theta_k)\frac{\partial \tilde{o}_1(x,y)}{\partial y}\right)^2 \tag{4-5}$$

In the relationship expressed above, $h_k$, $v_k$, and $\theta_k$ can be estimated by minimizing all $E_k(\theta_k, v_k, h_k)$ error functions. The detailed method of calculating the former equation and obtaining $h_k$ , $v_k$, and $\theta_k$ is explained in [76], [77].

In the cases of no rotational shift in the images with respect to each other, such as the situation we had in our experiments, the shift estimation task can be simplified by calculating only horizontal and vertical shifts using a transformation method [78].

## 4.4 Image Reconstruction Techniques

There are several methods for image reconstruction in SR, among which we present below nonuniform interpolation and the inverse problem [79].

### 4.4.1 Multiframe Nonuniform Interpolation

Multiframe nonuniform interpolation is the simplest method for HR image reconstruction [79]. There are three fundamental steps in the interpolation process: (a) motion estimation, (b) nonuniform interpolation to provide the HR image, and (c) the denoising and deblurring process. The final step can be accompanied by using a deconvolution algorithm with the denoising step embedded. The interpolation technique does not include any optimization process; therefore, the resolution enhancement is not comparable to what is achieved with the optimization-based methods. The advantage of the interpolation method is that it is computationally simple, which makes possible the real-time reconstruction of a series of images. However, the quality of reconstruction is not optimal, and the reconstruction method ignores the error added to the system by interpolation [79]. This technique has not been utilized in my images, and the interpolation that we have used for some of my results is based on single-frame Spline interpolation that doesn't provide any resolution enhancement.

### 4.4.2 Inverse Problem Method

Inverse problem method is another SR approach for image reconstruction [79]. In this part, I describe the way the pixel SR that was utilized in our project works [14], [76]. Assume that low-resolution (LR) images are identified by $X_k(n_1, n_2)$, $k = 1, 2, \dots, p$. These are shifted images with size $M = N_1 \times N_2$. For the high-resolution (HR) image $Y(n_1, n_2)$, the image size $N$ is equal to $LN_1 \times LN_2$, where $L$ is the number of shifted mages in each direction. Any given low-resolution image ($Y$) can be described as a linear super position of all high-resolution images. Assume that we vectorize the pixels of the k-th low-resolution image in a row as $X_k = [x_{k,1}, x_{k,2}, \dots, x_{k,M}]$ and, for a high-resolution image, as $Y = [y_1, y_2, \dots, y_N]$. Based on these definitions, each pixel in an LR image is a weighted super position of HR pixels such that [14]

$$\tilde{x}_{k,i} = \sum_{j=1,2,\dots,N} W_{k,i,j}(h_k \; v_k).\, y_j \tag{4-6}$$

In this equation, $W_{k,i,j}$ is a "physical weighting coefficient" [14], representing the effect of blurring, motion, and under-sampling, and it can be determined by a light-intensity map covering the sensor array [14], [79]. By assuming $Y_{fil}$ as the high pass filtration (using Laplacian operator) of the LR image ($Y$), minimizing the error function, $C(Y)$:

$$C(Y) = \frac{1}{2} \sum_{\substack{k=1,2,\dots p \\ i=1,2,\dots,M}} \left(x_{k,i} - \tilde{x}_{k,i}\right)^2 + \frac{\alpha}{2}\left(Y_{fil}^T.\, Y_{fil}\right) \tag{4-7}$$

provides the high-resolution image [14].

The first term of this equation is to minimize loss error in the $[x] = [W][y]$ equation and is equivalent to the maximum likelihood estimation, assuming that we have uniform Gaussian noise. However, the second term is the regularization part of the optimization problem that contributes the high-frequency components of the reconstructed image, $Y_{fil}$. As you can see from

the equation, the value of $\alpha$ , determines the amount of high spatial frequency components by the cost of tolerating high frequency noise in the recovered image [14], [75], [79], [80].

In our super-resolution imaging project, we used the code from the Milanfar Group at the University of California, Santa Cruz (UCSC). The algorithms implemented in the graphic user interface (GUI) are designed based on the papers mentioned at the end of the manual. The code can be downloaded from their academic website: http://users.soe.ucsc.edu/~milanfar/software/superresolution.html. Among different algorithms, we have worked with "Iterative Norm II" which is generally based on the optimization explained before (with an iterative matrix analysis), and its implementation is explained comprehensively in [80].

## 4.5 Simulations of the Pixel Super-Resolution Technique

As mentioned above, the purpose of this project was to improve the resolution in incoherent imaging systems where diffraction is negligible and the limitations in the resolution are the pixel size and noise. Thus, the preliminary simulation was designed to mimic the situation of having several low-resolution images that have shifted with respect to each other. For this reason, we chose an image containing an adequate number of features smaller than the pixilation size. Then the image was pixilated (blurred) by a factor of 3; in other words, the number of pixels in the image became three times smaller. To provide an adequate number of LR frames, the high-resolution image was scanned in a 10 × 10 grid array. With the aim of simulating real conditions, we added 10 dB of random noise to the images and then used the noisy low-resolution images as input for the code to provide the high-resolution output:

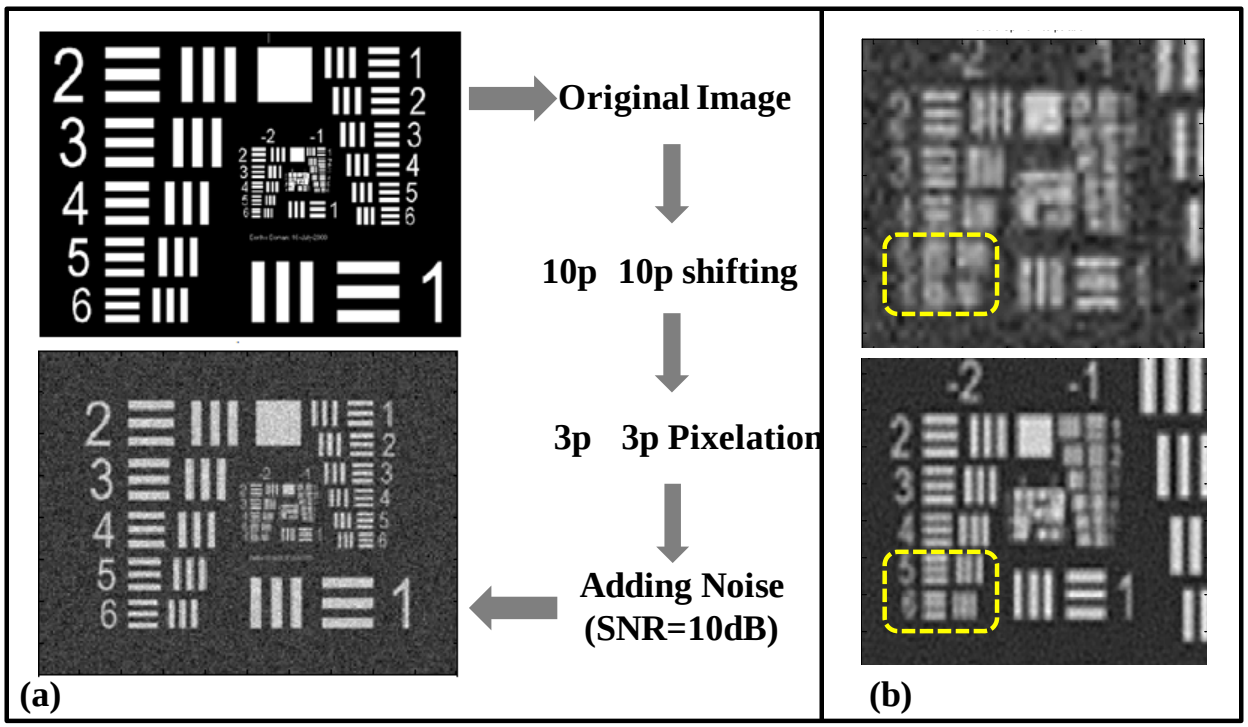


**Figure 4-2 | (a) The left image shows the way we provide artificial low-resolution and noisy images out of the pure high-resolution image. (b) The right image (bottom) depicts the high-resolution recovery out of a noisy and low-resolution image (top) using the iterative norm II method from [80].**

## 4.6 PSR Experimental Setups and Bright Field-Imaging Results

In order to have sub-pixel shifting, a scanning mechanism that shifts the imaging system versus the object (e.g., a fluorescent sample) is needed. For this reason, we used a NanoCube® XYZ Piezo-stage compact multiaxis Piezo system for nano-positioning and fiber alignment. The precision of this machine is 2 nm in each of its three axes. This stage was controlled by a LabVIEW code that synchronized it with the CCD stage attached directly atop it.

For the first experiment, the image sensor we used was the same as what is described in Chapter 2 (Kodak, KAF 8300, pixel size: 5.4 μm). For the object, an Air Force target image was projected and demagnified on the surface of the moving system to provide a zero-friction setup.

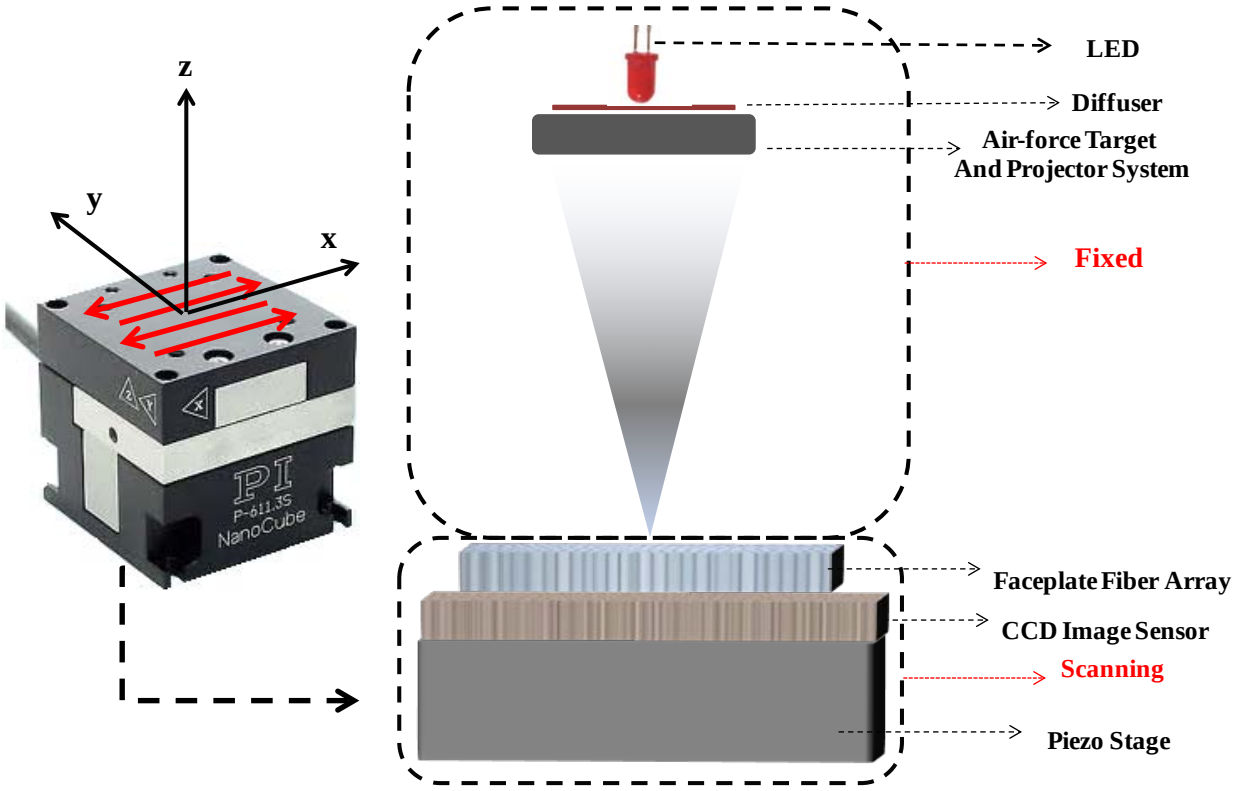


**Figure 4-3 | Experimental setup, using a faceplate.**

The faceplate has a negative effect on resolution, due not only due to the larger faceplate pixel size but also to the fact that the larger period size (the faceplate pitch size ~ 6 um) is not a multiple integer of the smaller one. This fact results in *location-dependent pixel function* on the surface of the CCD image sensor.

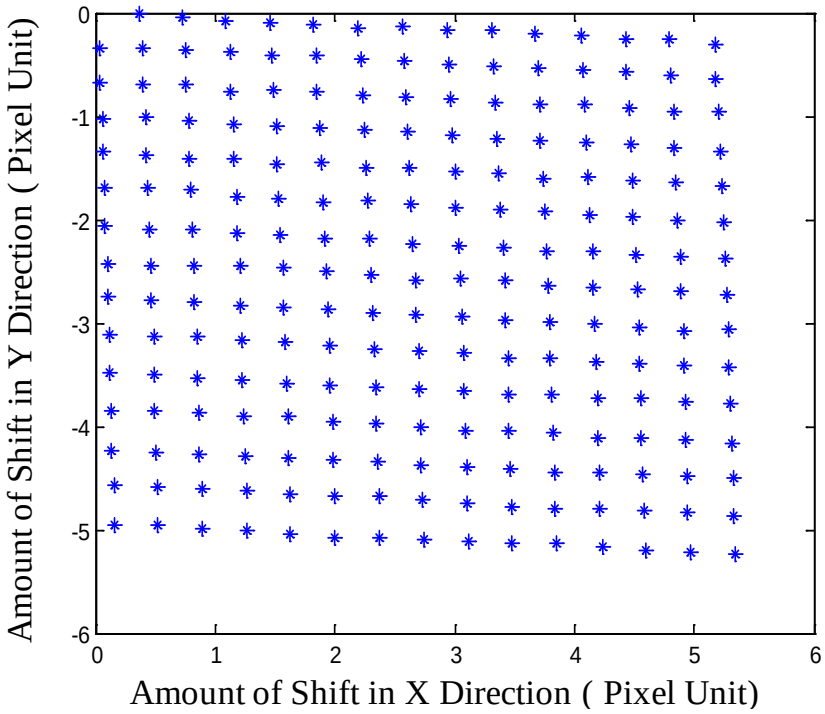


**Figure 4-4 | Shift estimation obtained from the software when the Piezo was programmed to span a uniform grid with the step size of 2 um. As indicated, the grid resulting from the code is very similar to a uniform pattern. This shows the accuracy of the shift estimation code in dealing with the amount of noise that occurred in the imaging system.**

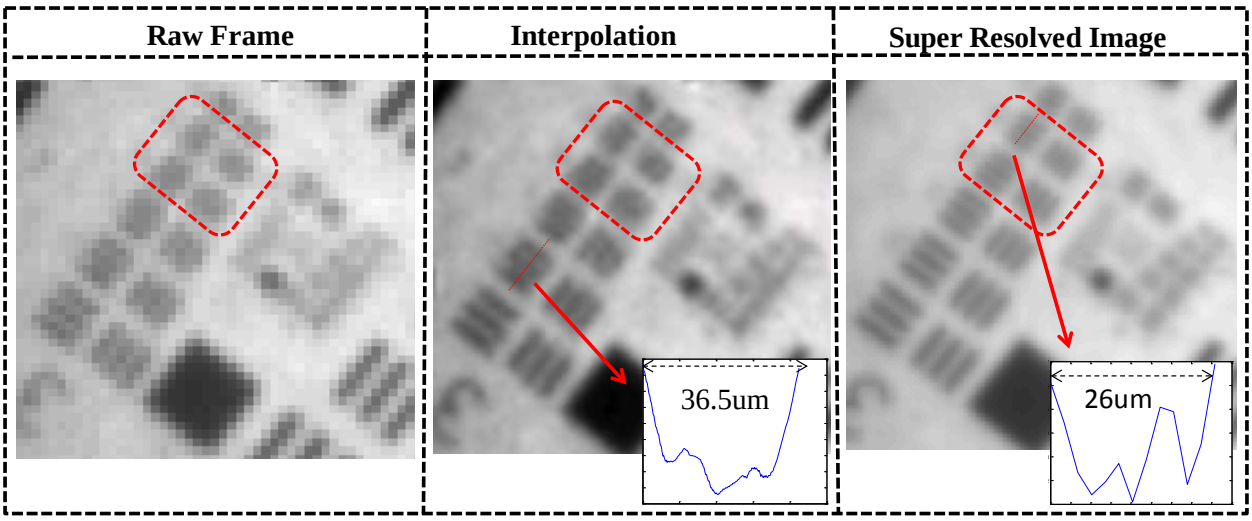


**Figure 4-5 | The image on the left is the raw frames obtained by using the image sensor. The image in the middle shows the interpolated form of the raw image. On the right is a processed image after applying the iterative super-resolution algorithm.**

The quantified resolution in this system is 5.2 µm (87% of faceplate pitch size).

## 4.7 Experimental Setup for Pixel Super-Resolution Fluorescent Imaging

For the fluorescent imaging, we used a setup similar to the one explained in the previous part but with some modifications. For the illumination, we positioned light-emitting diodes (LEDs) parallel to the sample substrate. As a result, the refractive index contrast between the glass and air made the substrate act as the waveguide to transfer the LED light to the entire glass area. The sample was held tightly parallel to the compound of the image sensor and the Piezo stage so that, when a particular area was scanned by the stage, there would be sub-pixel shifting between the sample and the CCD.

An absorption filter in the form of a thin film with a thickness of around 20 µm was coated [81], [82] on the faceplate's surface. This absorption layer was needed to facilitate in blocking the ambient light and the scattered light from reaching the image sensor. The faceplate

was used to protect the image sensor's surface from friction and thus to prevent damage to this sensor. In addition, it was needed to shield the fluorescent sample thermally from the warmth of the circuitry. The faceplate pitch size was around 6 µm, with a thickness of 3mm, and the core or cladding ratio of 70:30. For this experiment, we used 10 µm red fluorescent beads (with the emission peak at 605 nm). For the excitation, we chose blue LEDs with an excitation peak at 470 nm. For the shift estimation, 25 images were captured; however, due to the large amount of noise and some friction remaining in the system, the effective grid that resulted had only 2×2-point shifting points.

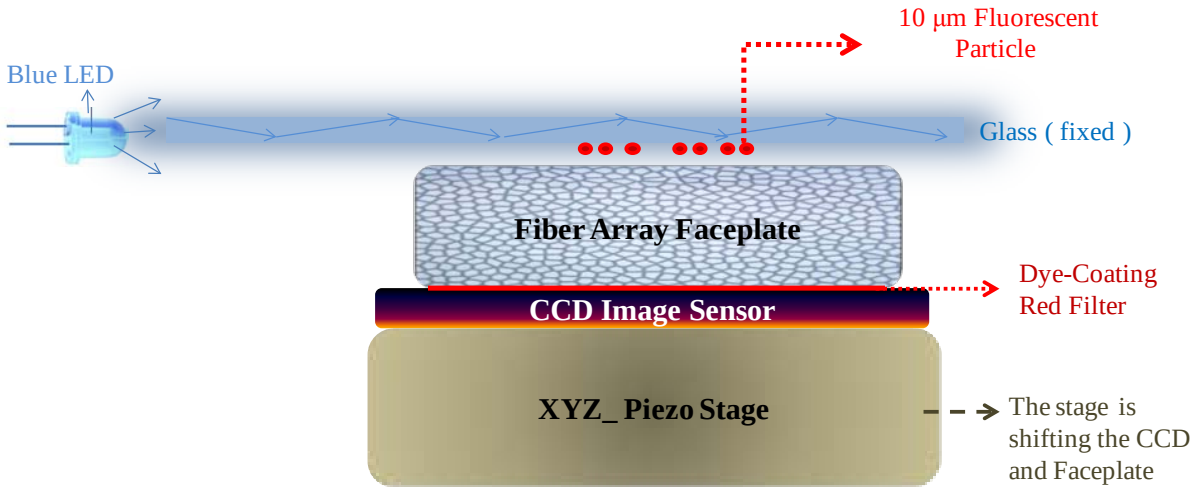


**Figure 4-6 | Schematic of the super-resolution imaging setup.**

To minimize the friction between the smeared glass and the faceplate fiber array, between each two frame-capturing moments, the stage pulled down the faceplate-CCD compound so that the lateral shifting occurred when there was a large gap between the fluorescent beads and the compound. After this movement, the stage rose up, captured the image, and then moved back for another move. All scanning and shifting were done automatically using the LabVIEW code. Fig.4-7 shows the preliminary result for fluorescent imaging. Although the current system is not improving the resolution considerably, it shows the potential of the method for fluorescent

imaging application. Note that the resolution in fluorescent imaging was lower than what occurred in test objects, as with Air Force target imaging. There are two main reasons for this: (a) the larger gap and more diffraction due to the 20-μm absorption filter coating and (b) the lower SNR of the emitting beads and the considerable amount of background light caused a large amount of noise on the raw frames. In addition, each small region of a raw frame needed to be processed separately since shift estimation varies greatly from point to point on a raw frame.

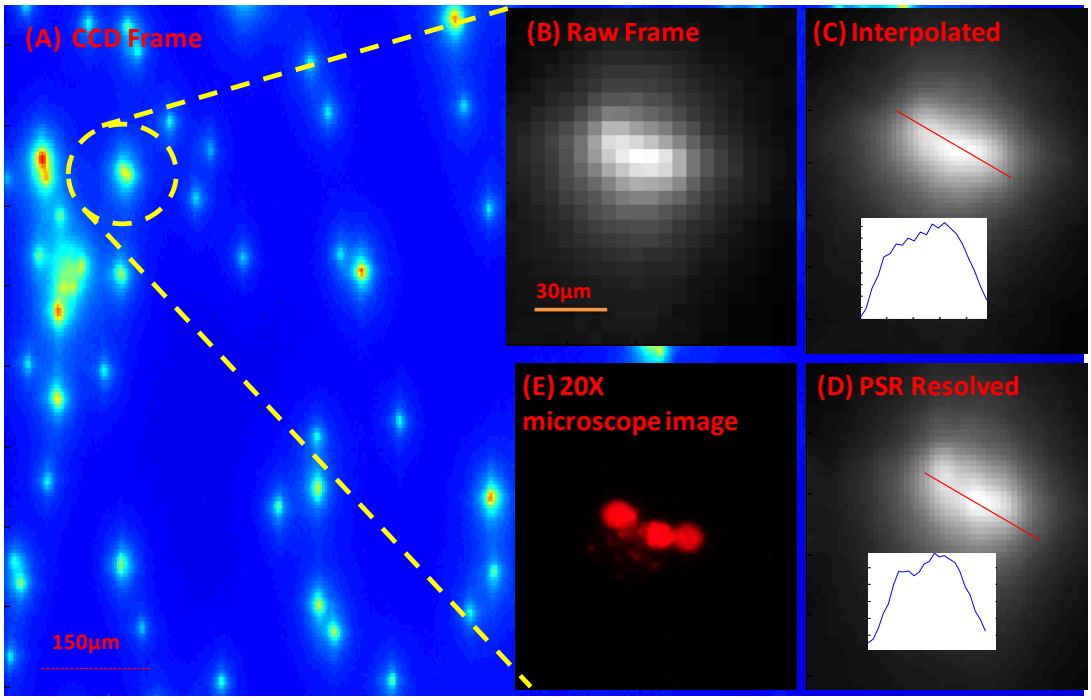


**Figure 4-7 | Lensfree super-resolution fluorescent imaging results. (a) The blue background depicts a large area of a frame captured by the CCD. (b) The cropped region from the large area of the CCD frame. (c) The interpolated image. (d) Super-resolved reconstruction of the cropped region using 25 raw frames provided a 2 × 2 matrix for shift registration. The gap between two beads has appeared. (e) A small gap between two adjacent beads appears in the final image.**

## 4.8 Experimental Setup Using Tapered Fiber Array

Tapered fiber array is a component containing an array of optical fibers that are stretched in such a way that cladding and the core diameter size are scaled down in one surface of the object compared to the other. Consequently, the optical pattern on one side is transferred to the other surface with a magnification or demagnification factor equal to this stretching factor. In one sense, the application of this device is very similar to that of a lens; however, unlike with lenses, there is a fixed magnification factor for tapered fiber arrays. Another limitation of tapered fiber arrays is the minimum feature that can be obtained with this device, which is dependent on the cladding diameter. These limitations come, however, with advantages. There is very low aberration with tapered fiber arrays, whereas it is a serious problem in lens-based imaging systems. In addition, these arrays are compact compared to lenses [19].

The tapered that we used was an array of fibers for which the ratio of the whole diameter of the large size to that of the small size was 18:8 mm; the magnification factor was therefore 2.25. This tapered, which was placed directly on top of the complex of the faceplate and CCD image sensor, translated the magnified object sitting on top of it into an array of CCD pixels. In my experiment, we projected the pattern of the Air Force target onto the smaller facet of the tapered.

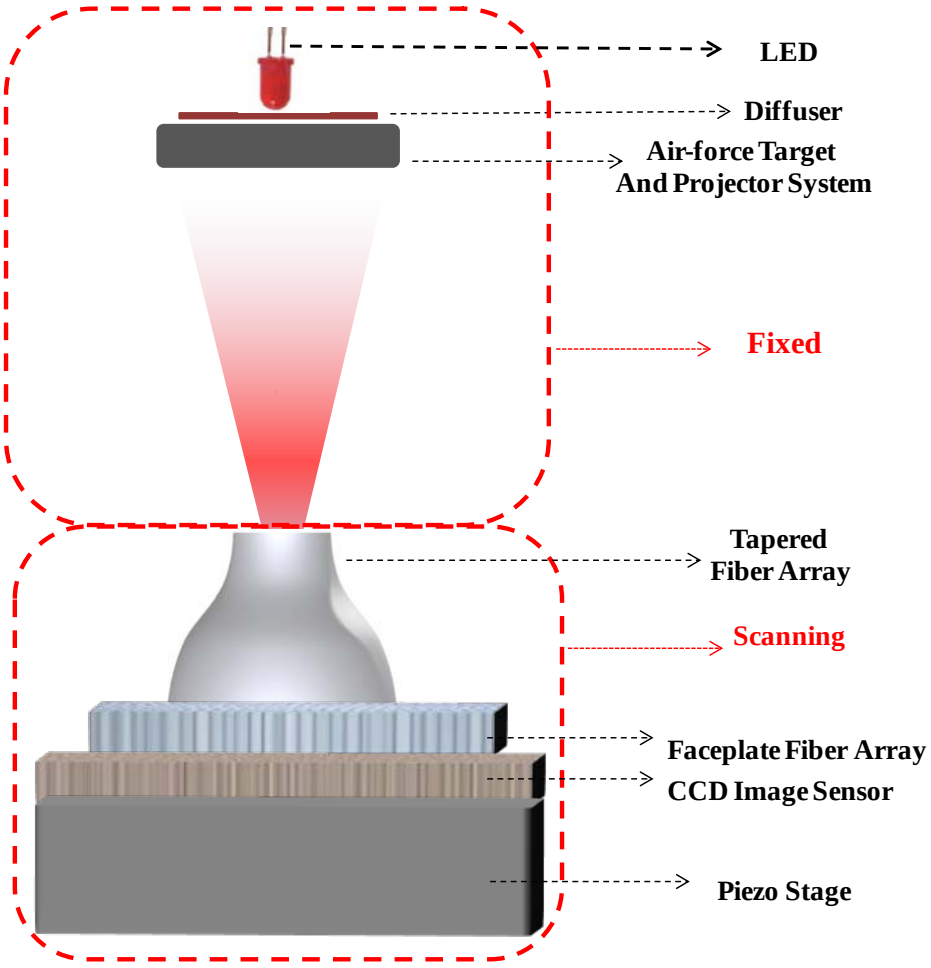


**Figure 4-8 | The schematic of the lensfree super-resolution imaging using the complex of the faceplate and tapered fiber array. The LED and the projected pattern are fixed while the tapered-faceplate-CCD compound scans using the Piezo stage. The inset illustration on the left depicts the actual Piezo stage.**

Fig.4-9 represents the shifting pattern estimated by the code when we scanned a uniform array, 14 × 14 with the step size of 0.5 μm, with the Piezo stage. The shifts were estimated based upon the pixel size unit. The estimation shows a highly nonuniform array with an unexpected amount of shift and direction. This is due to the insufficient amount of friction between different components, especially between the tapered and the faceplate. This resulted in a slight sliding of one surface on the other, and consequently, the tapered did not shift as programmed via LabVIEW.

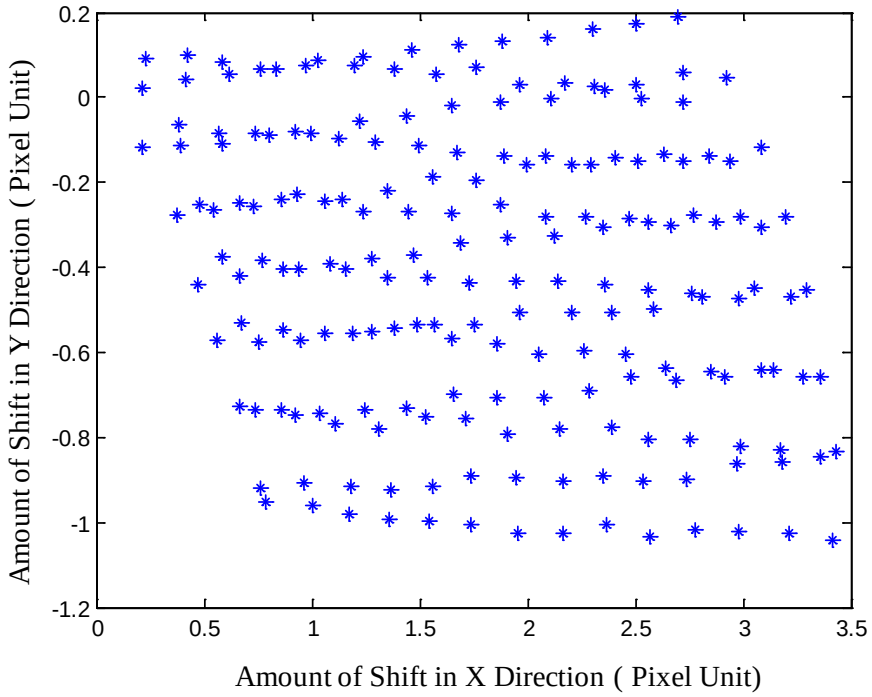


**Figure 4-9 | Shift estimation calculated by the code when the Piezo was programmed to span 14 × 14 points with the step size of 0.5 µm. The nonuniform arrangement of the points is the result of deficiencies in tightening all touching surfaces.**

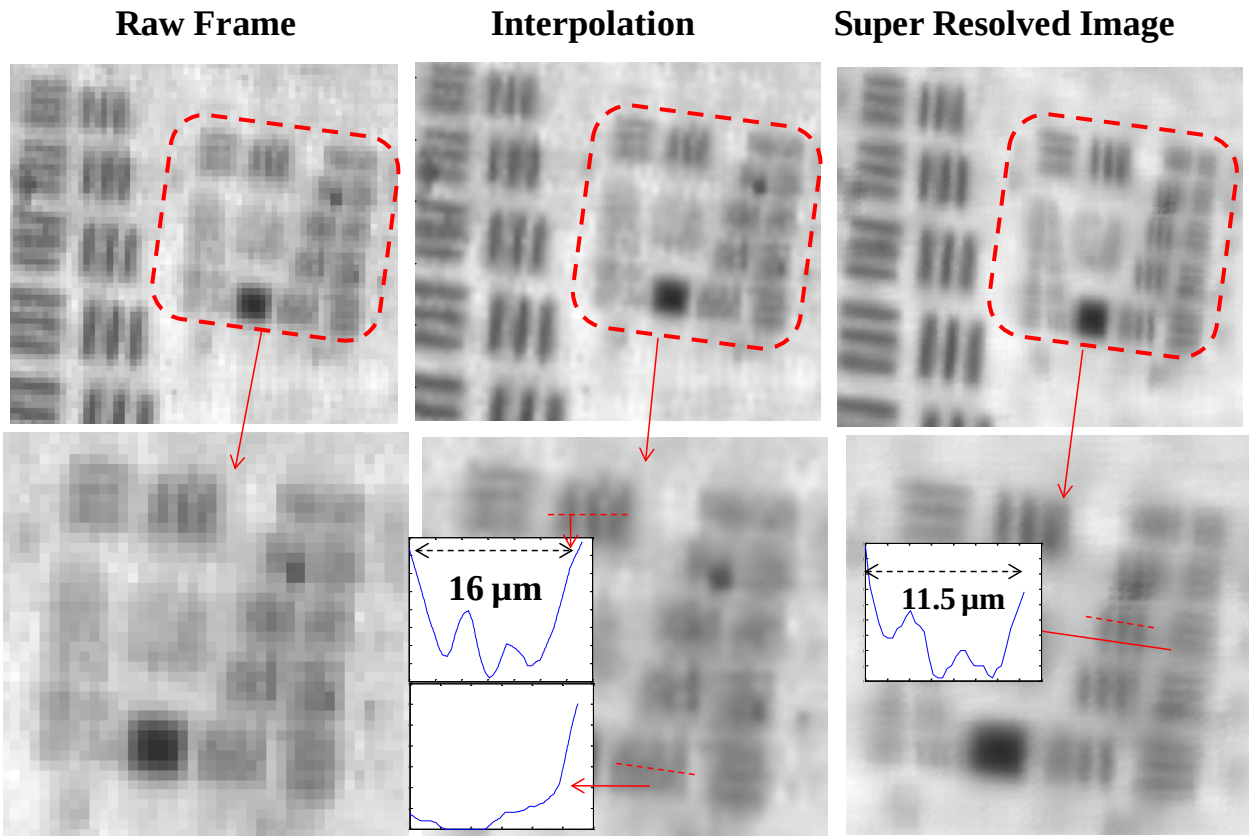


**Figure 4-10 | The left column shows the raw frame from the CCD with 3.2-um resolution. The middle column is an image produced by interpolating all the points from all the frames with the same resolution as the raw frame. The right image is the super-resolved image, which contains finer features with 2.3-um resolution.**

## 4.9 Conclusion

In this chapter, I introduced lensfree super-resolution techniques for large field-of-view incoherent imaging. These techniques were implemented both with and without a tapered and with different shifting mechanisms. In all cases, sub-pixel size resolution for incoherent objects achieved. It was shown that adding extra components, such as a faceplate and tapered, adds diffraction to the system, which, because there is no lens, makes the final resolution worse than the expected value.

I provided a demonstration of lensfree super-resolution fluorescent imaging, which can be a powerful technique for thin (2D geometry) samples.

# Chapter 5 Conclusion[7]

## 5.1 Conclusion and Summary

In the first part of this thesis, we introduced the use of nanostructured surfaces for lensfree on-chip microscopy. In this incoherent on-chip imaging modality, the object of interest was positioned directly onto a nanostructured area fabricated using FIB. The emitted light from the object plane was modulated by the nanostructures, and it then diffracted over a short distance of glass thickness to be sampled by a CCD image sensor without there being any lenses in the optical path. Thus, the function of the nanostructures was to modulate the transmission light and encode point spread functions (PSFs) in such a way that they formed a matrix in which each row was unique and referred to a particular point of the substrate. This matrix was obtained through the calibration step in which a focused spot size was used to scan the nanostructured substrate area. At each scanning point, the lensfree far-field diffraction pattern was captured and recorded by the CCD image sensor. The detected far-field diffraction was given to the CS algorithm as the input, knowing the calibration matrix to achieve imaging at the sub-pixel level. We used this technique for multicolor imaging as well. Instead of relying on the highly dispersive behavior of noble metals, such as gold or silver, we deployed an RGB image sensor to sample different colors with different pixel types in optical frequencies that could provide wavelength-sensitive diffraction frames. In this case, diffraction patterns were then sampled in the far-field using a color-sensor array, in which the pixels had three different types of colorfilters at red, green, and blue (RGB) wavelengths. The recorded RGB diffraction patterns (for each point on the structured substrate) formed a basis that could be used to reconstruct digitally any arbitrary

[7] Reprinted with permission from [32], Copyright [2010], American Institute of Physics, and [33], Copyright [2010], American Institute of Physics and [48], Copyright [2010], American Institute of Physics

multicolor incoherent object distribution at sub-pixel resolution, using a compressive-sampling algorithm [32], [33]. We experimentally demonstrated the practicability of this lensfree method at various wavelength ranges, improving the resolution by ~ 9 fold for single color and colorful objects. This imaging modality based on nanostructured substrates can be especially useful in creating lensfree fluorescent microscopes or lens based systems that suffer from large pixel size on a compact chip [48], [83].

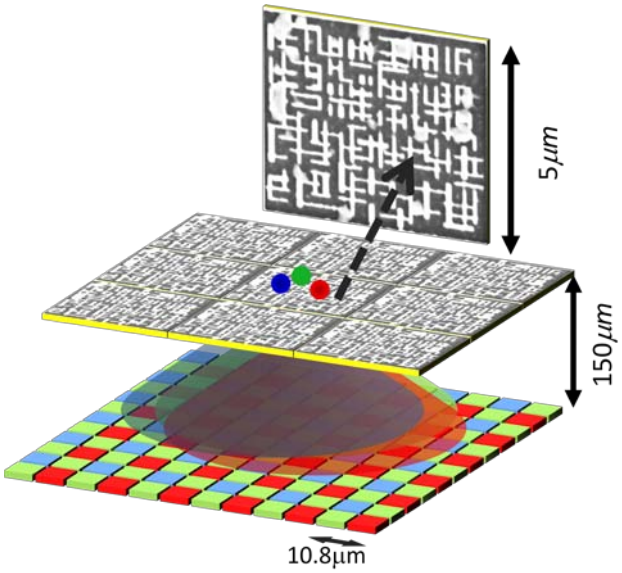


**Figure 5-1 | Nanostructured substrate for lensfree color imaging. The lensfree far-field diffraction pattern of each color is captured by a different set of pixels. Figure reprinted with permission from [33], copyright [2010], American Institute of Physics.**

In addition, we demonstrated the application of this lensfree technique for infrared imaging. Providing high-resolution near-infrared (NIR) and infrared (IR) imaging is highly important for both medical applications (as in breast cancer early detection) and surveillance purposes. To address this aim, we demonstrated sub-pixel resolution of NIR objects in a lensfree

system. This method can be used in a regular lens-based camera to increase the pixel density (i.e., decrease pixel size) artificially and thus gain higher-resolution images, which can be extremely important for large-pixel-size and expensive thermal cameras.

The way we used CS for lensfree incoherent imaging is acknowledged among CS community members (http://nuit-blanche.blogspot.com/).

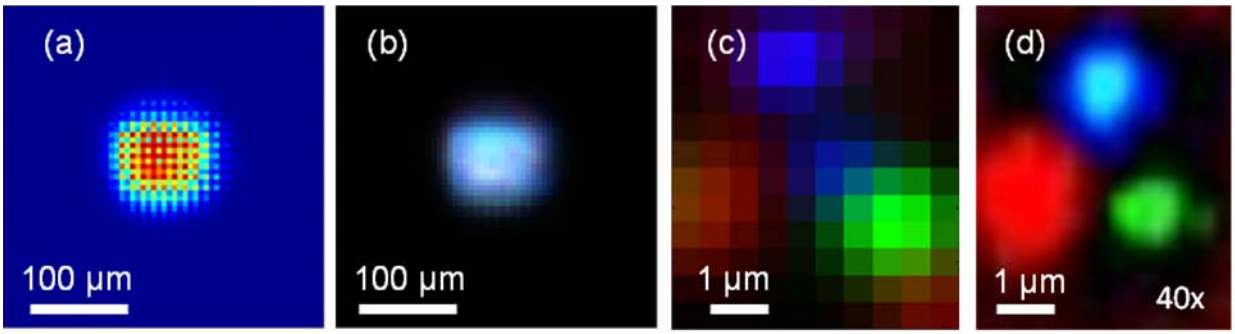


**Figure 5-2 | (a) Far-field diffraction pattern captured by an RGB image of the object shown in (d). (b) Demosaiced pattern of (a). (c) Recovered image using compressive sensing. Figure reprinted with permission from [33], copyright [2010], American Institute of Physics.**

The idea of embedding information in lensfree and far-field diffraction patterns was used for plasmonic sensing as well. We demonstrated lensfree on-chip sensing within a microfluidic channel using plasmonic nano-apertures that were illuminated by a partially coherent light source, which could be a monochromator or a regular LED. In this approach, lensfree diffraction patterns of the transmitted light modulated by metallic nano-apertures located at the bottom surface of the microfluidic channel were recorded with a monochrome CMOS ( 2.2 µm) while the liquid ( and thus, the refractive index) of inside the microfluidic device was changing with a automated syringe pump. These lensfree diffraction patterns were rapidly processed, through phase recovery techniques, to back-propagate the optical fields to an arbitrary depth for creating digitally focused complex transmission patterns by knowing intensity distribution on the sensor

plane. For that, we used a polarized illumination and verified single-polarization output light field, which is essential when utilizing the Gerchberg_Saxton algorithm on vector components. Cross-correlation of these patterns enabled sensing and quantifying the local refractive index change that surrounds the near-field of the plasmonic nano-apertures, which can be used to analyze bio-molecules in a liquid sample. This proposed lensfree plasmonic sensing tool has the sensing area scaled up to the imaging area. Based on this principle, we experimentally demonstrated lensfree sensing of refractive index changes as small as ~ 2 x $10^{-3}$. This on-chip sensing approach could be quite useful for the development of label-free microarray technologies by making an array of plasmonic structures on the same microfluidic chip, which could significantly increase the throughput of sensing without scanning the illumination spot or deploying bulky lenses or collimators [48].

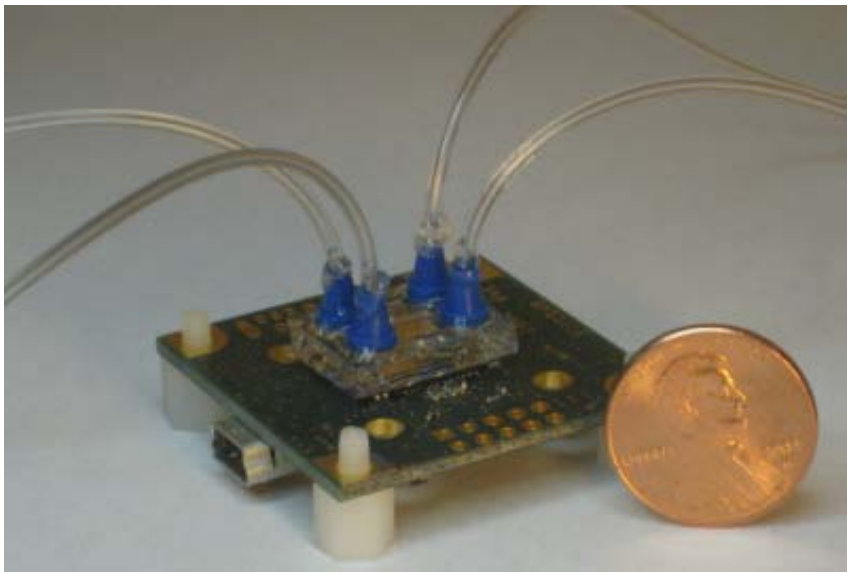

**Figure 5-3 | Implementation of the lensfree plasmonic sensing device placed directly on top of an image sensor.**

These specifications make this device suitable for DNA or protein microarray label-free sensing and imaging. Each DNA spot contains pico-moles of a particular DNA sequence that is

called a probe [84]. Printing micron-size DNA spots on the surface of the array of subwavelength apertures builds an independent sensing element from each set of apertures. Image processing and phase recovery can decompose overlapped far-field diffraction patterns and provide field distribution on the aperture plane. Different antigens can be printed on different sets of apertures fabricated on one substrate to detect and quantify different antibodies in a single experiment.

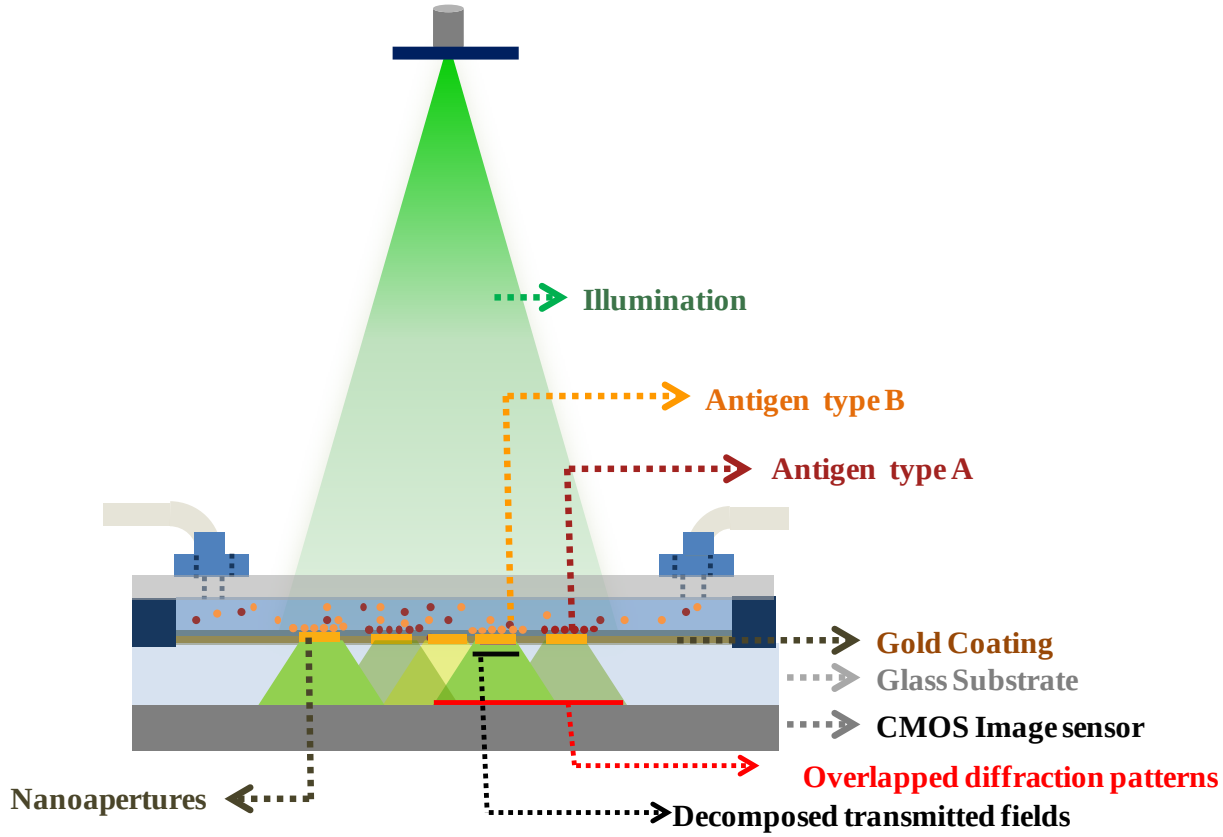


**Figure 5-4 | Schematic of a lensfree plasmonic sensing device used for detecting different antibodies in one microfluidic chamber. For instance, two different antigens, A and B, are printed on nano-apertures. The diffraction pattern captured on the CMOS image sensor plane can be back-propagated on the aperture plane so that binding information regarding each antigen type can be extracted and quantified.**

Another technique we used for proving a high-resolution incoherent imaging technique for lensfree systems was the pixel super-resolution (PSR) algorithm. The PSR technique works

based on having multiple frames of low-resolution samples that shifted with respect to each other [14], [79]. It was shown that inserting extra components, such as a faceplate and tapered fiber array, resulted in additional diffraction to the system and that such modifications, along with there being no lens, caused the final resolution to be worse than expected.

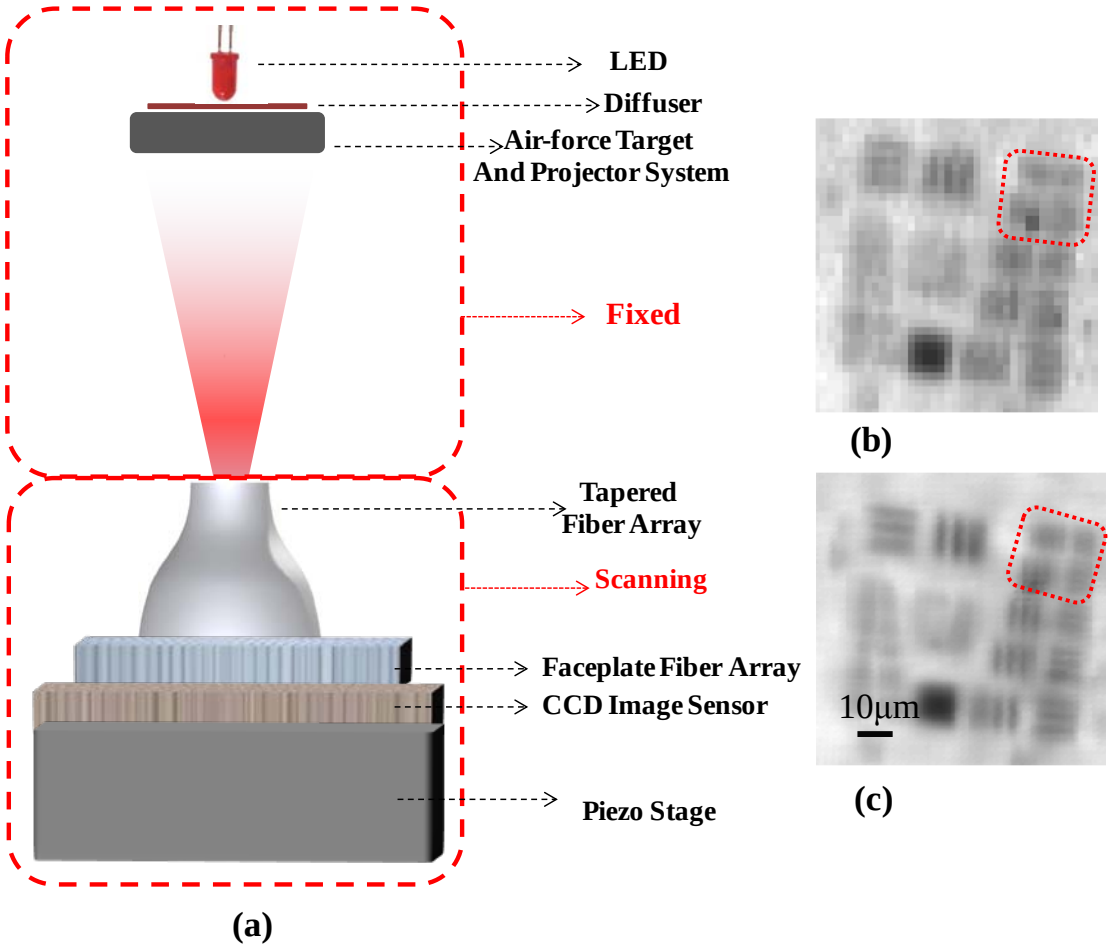


**Figure 5-5 | Pixel super-resolution (PSR) method using a tapered fiber array. (a) Schematic of the setup. (b) Low-resolution raw image with 4.6-μm resolution. (c) Super-resolved high-resolution image with 2.2-μm resolution.**

# Appendix Optofluidic Spectroscopy and Multicolor Flow Cytometry Using the Spectral Imaging Method

## A.1 Introduction

Fluorescent imaging has been the core parts of many research activities because we can detect and sense different biological components simply by labeling different fluoresphores. In the case that we are dealing with single-color labeling, an imaging system can be achieved using a single illuminator, which is usually a single-color laser. However, if a mixture of colors is used, there should be a smart mechanism by which we can decompose overlapped images that occur in the detector. If we need to image and decompose different fluorescently emitting components simultaneously, we need to convert the imaging domain to a spectral domain to translate different parts of the image to their corresponding color components proficiently [85], [86]. The technique that combines imaging and spectral unmixing is called *imaging spectroscopy* and has been used extensively in biological applications. In an imaging spectrometer, the light from the excitation source, which is usually a powerful laser at the blue or ultraviolet wavelength or a filtered light-emitting-diode (LED), strikes the fluorescent particles in a flow [2], [85–87].

The power spectrum from the point object, after being broadened by a dispersive component, focuses on to the detector plane, which can be a photomultiplier, CCD, or CMOS image sensor. The dispersive element's main function is to bring a wavelength-dependent shift of the image; in other words, each image constructed at a particular position represents a specific part of the object's power spectrum [2].

In the first part of this chapter, I will introduce an imaging spectrometer device implemented on an RGB CMOS camera (effective pixel size= 2.8 μm) and that can be easily

applied to a cellphone. In the second part, I will explain how this same device, when implemented on a cellphone, can be used for multicolor fluorescent flow-cytometry. The device can be a handheld and cost effective add-on that can be simply installed on a cellphone to differentiate and count different color particles in a flow.

## A.2 Optofluidic Fluorescent Spectroscopy Using Linear Variable Filters (LVF)

Researchers from Professor Aydogan Ozcan's laboratory at UCLA have introduced the optofluidic cytometry on a cellphone. This is quite a powerful technique for imaging and counting all the fluorescent particles emitted by the light sources used in the system [88]. However, there has been no mechanism to distinguish different color particles emitted at each moment; instead, it has been necessary to deal with the intensity of each signature regardless of its emission spectrum.

To address this issue, we modified the system in such a way that it translated the spectral information of the emitting particle to a parameter that was measureable by our imaging system. The component we added to the system is a linear variable filter (LVF), which is an interference filter with a spectrally unique transmission function at each point along its length. The LVF used was fabricated by the JDSU company (http://www.jdsu.com). The transmitting wavelength linearly varies from 400 nm to 700 nm, with the bandwidth less than 20 nm for each point per wavelength. This component is widely used for spectroscopy, as it provides narrow-band filtering, with an almost flat transmission amplitude across the whole visible spectrum. The LVF was installed directly below the flow-container, a PDMS-based microfluidic device or a glass capillary, so that the fluorescent emission of each flowing particle, after filtering at each point and wavelength, reached the cellphone's CMOS camera.

## A.3 Spectral Imaging Simulation under Noisy Conditions and Spectrum Recovery

To simulate emission spectrum recovery out of the captured light by an image sensor that is modulated by the LVF function and has become noisy, we used the Lorentzian Line Shape [89] to model a bead's emission spectrum. These were the additional assumptions for this set-up: the bandwidth at each point of the LVF was 25 nm, the spectral sampling was 0.2 nm (which is wider than what we can have with 10 µm/sec bead velocity), only blue pixels were chosen for this particular bead type, and the system had 10 dB speckle noise. A simple Gaussian spectrum with 100 nm bandwidth around 450 nm was selected to model the filtering performance of blue pixels. Fig.A-1 (a) demonstrates all the functions dealt with in this simulation.

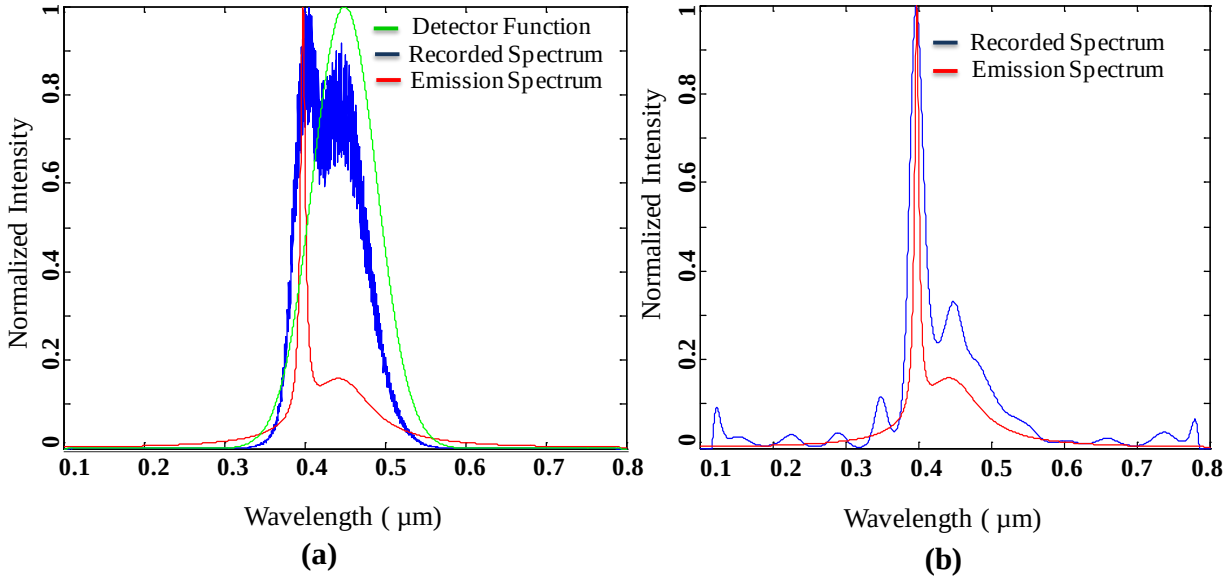


**Figure A-1 | (a) Noiseless emission spectrum of the bead under investigation (red line), noisy recorded spectrum over the length that is directly mapped to the wavelength ( blue line), and detector function for blue pixels (green line). (b) Recovered spectrum using compressive sensing and Lucy-Richardson deconvolution (blue line) vs. noiseless emission spectrum.**

The red curve represents the emission spectrum of a fluorescent bead using the Lorentzian function. The blue curve shows the noisy data over the LVF length (which corresponds to the visible wavelength range), and the green one is the simplified detector function for blue pixels. Recovering the emission spectrum of the bead (the red curve) necessitated knowing the detector function and the LVF transfer function that was demonstrated with a series of Gaussian functions and one step of mathematical analysis. For the recovery algorithm, we used one step of compressive sensing (as explained in chapter 2), followed by a Lucy-Richardson deconvolution. Compressive sensing provides a set of sparse points, instead of a solid curve, but it is a valuable step that, due to the nature of its iterative algorithm, has the functionality of denoising from noisy data.

Fig. A-1 (b) demonstrates the recovered data out of the noisy measurement in simulation. A decent compatibility between the ideal curve and the recovered one is observable especially in the central part of the emission spectrum (300 nm-600 nm).

## A.4 Experimental Set-up for Optofluidic Spectroscopy

In this cytometry system, the liquid sample was delivered to the system using a motorized syringe pump with a speed around 1-1.5 µLit/min. This microfluidic device or the capillary was sitting directly on the surface of the LVF. The glass surfaces and water content of these devices had the functionality of light guiding because of total internal reflection, so most of the excitation light was bound inside the liquid-holding device and the emission light from the labeled particles left the medium and traveled through the optical system. One droplet of index-matching oil connected the LED and the fluidic device to maximize the coupling of the light to the system.

With this method, there was adequate excitation light and no need to use costly and bulky coupling components.

The filtering behavior of the microfluidic-wave-guide in rejecting the excitation light was not perfect; therefore, another filtering mechanism that would prevent the excitation light from being captured by the CMOS camera was needed. For this purpose, we used a low-pass and high-quality glass absorption filter. For the extra lens that we added to the system, the distance between the lens and the particles in the microfluidic component was equal to its focal length. This lens mapped part of the microfluidic device that sat in its focusing domain to an image formed in infinity that was guided by an image sensor lens as the final image to the CMOS image sensor. For the first part of this project with the purpose of spectroscopy, the added lens had a focal length of 12 mm, and because the focal length of the camera lens was around 5 mm, there was a 2.4X demagnification in the system, which made 10 μm fluorescent particles become 4 μm circles in captured frames. In addition, with this demagnification, it was possible to capture an adequate length of spectral distribution on the LVF and spectral information of the fluorescence emission. Since the optical path of the fluorescent particles was perpendicular to the excitation light and sample flow, we could continuously deliver the sample to the system without touching the optics to change the sample solution. As the liquid was moving in the system, the camera captured the movie, showing the images of the fluidic system in real time. These images could then be sent to a calculation station for extracting data from raw frames.

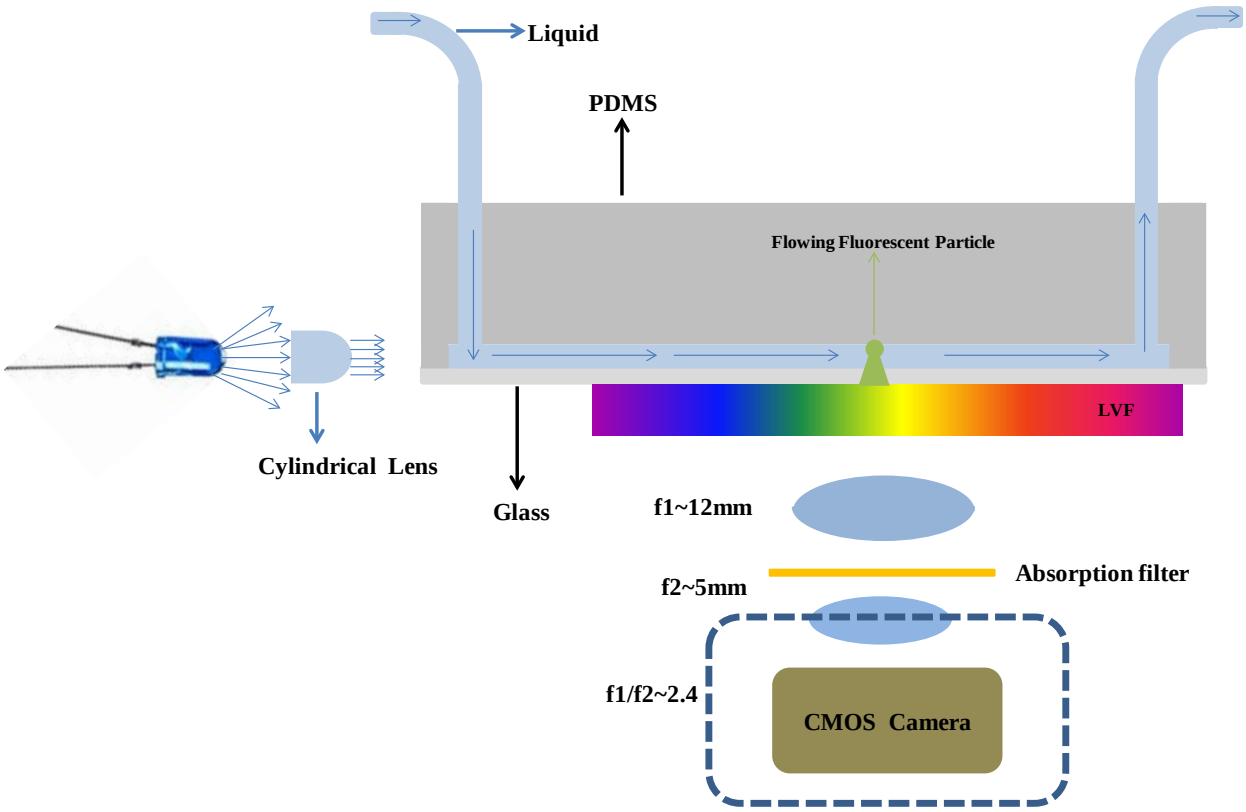


**Figure A-2 | Optofluidic setup, using an LVF and a CMOS image sensor. The LED light is directed to the bottom glass layer of the microfluidic device via a cylindrical lens.**

## A.5 Calibration Process to Eliminate the Dispersive Effect of Imaging Components

As mentioned, the transmission profile of the LVF is flat, which means that the transmitted intensity at each point could represent the value of the power spectrum at that particular wavelength; however, there were many dispersive components in the system that modulated the transmission spectrum in such a way that it was highly wavelength dependent. The main dispersive element was the absorption filter with a non-flat transmission function in the visible spectrum. The second dispersive component in the system was the CMOS image sensor that contained red, green, and blue pixels. In addition to the dispersion caused by pixel arrays, the glass material of the lenses and microfluidic device manipulated the emission spectrum of

flowing particles before reaching the CMOS camera. Moreover, in some image sensors, due to the limited accessibility of the software for modifications, there is no access to the raw frames, and what we obtain from them has modified color distribution over the whole spectrum. As a result, there is unwanted spectral dispersion added to the physical dispersion part. Acquiring the correct transmission function required a calibration process to compensate the dispersion effect by quantifying the coefficient of increasing or decreasing the transmission spectrum versus the wavelength.

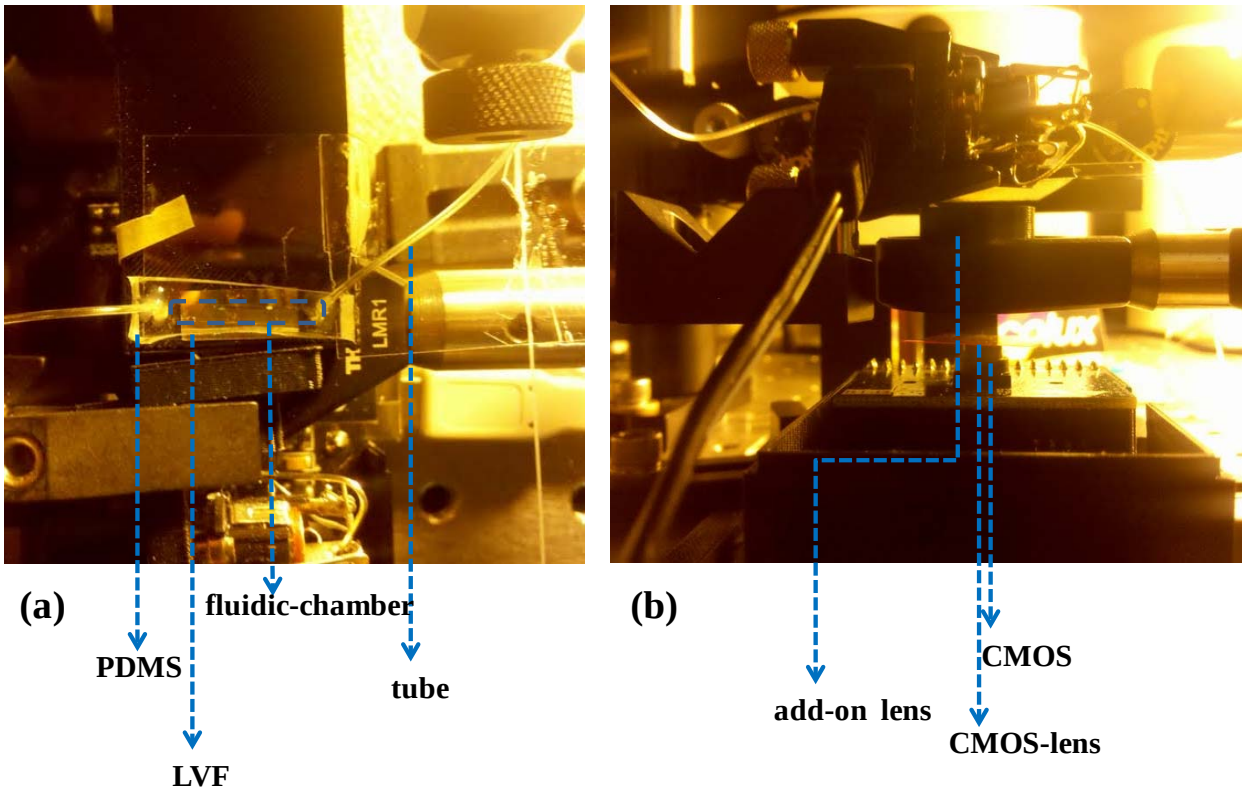


**Figure A-3 | Bench-top optofluidic setup using microfluidic device on an LVF, shown in (a) top view and (b) side view.**

The calibration process was carried out using a wavelength scanning monochromator device. In this way, the light from a monochromator was brought to the set-up via a fiber bundle

and was projected on the surface of the LVF using a beam expander, while all other components were already in the system. A diffuser was placed on top of the microfluidic device to provide spatially incoherent illumination in order to simulate the excitation behavior of fluorescent particles. By scanning the monochromator wavelength over the area expected to cover the emission spectra of fluorescent particles under investigation, we also provided part of the light from the monochromator to a spectrometer using a beam splitter in the path. This method not only supplied the bandwidth of illumination light at each wavelength but also made it possible to record the intensity of the light coming from the monochromator and therefore to neutralize the wavelength dependency of the monochromator light intensity. Having around 2 nm of bandwidth for the monochromator output light made possible 2 nm steps in the scanning range. For each wavelength, we captured a frame by the CMOS camera that represented how a single wavelength excitation was mapped to a particular location with a modulation amplitude factor.

## A.6 Tracking Moving Beads and Calibration Spectra Assignment

This part explains the technique by which the emission spectrum can be extracted out of frames captured by a CMOS camera. To achieve this aim, an algorithm that would track and target flowing beads in movie frames and then assign the spectral transmission function was necessary.

After scanning the wavelengths and capturing corresponding frames, we obtained the calibration frames by wavelength scanning monochromator. For each bead-coordinate in every frame, there was $N$-intensity values ($N$ is the number of wavelengths) obtained from extracting the intensity values from $N$ calibration frames at that location ( see Fig.A-4). Therefore, there was an $M \times N$ calibration matrix in which the spectral transfer function from moving coordinates

was embedded, and an $M \times 1$ matrix containing the intensity values of the fluorescent bead, and the aim was to find the $N \times 1$ emission spectrum of the bead.

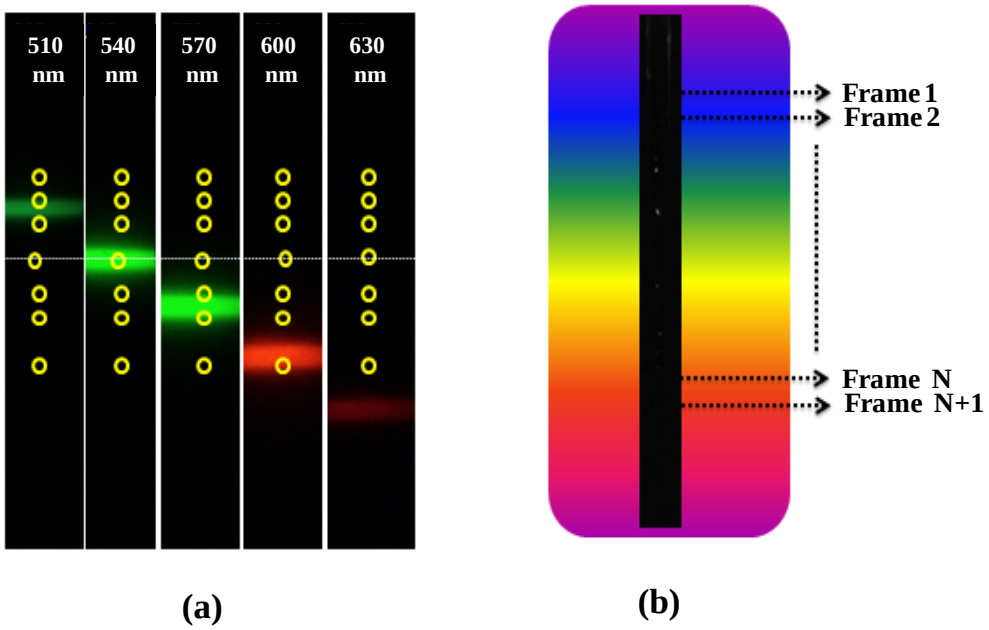


**Figure A-4 | (a) Calibration frames captured by scanning monochromator wavelength. By mapping these frames with the moving particle location, as shown in (b), the calibration spectra can be calculated.**

It should be noted that the transmission spectrum from each point of the LVF to the CMOS had a certain bandwidth for which it was necessary to apply one step of deconvolution analysis in order to recover the emission spectrum.

## A.7 Spectrum Recovery Using Compressive Sensing

To solve the linear matrix equation, an algorithm capable of dealing with noisy known data values with a dimension possibly smaller than the unknown matrix dimension ($M<N$) was needed.

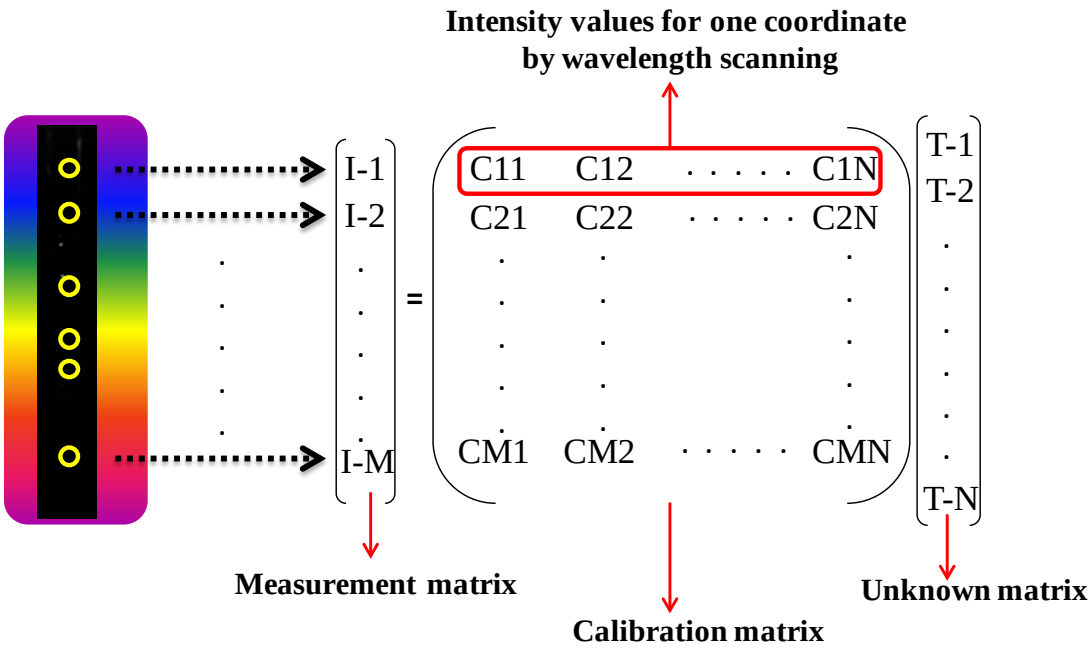


**Figure A-5 | Inverse linear equation, for use when the intensity of bead emission in all frames and calibration spectra are known.**

Compressive sensing could be regarded as a good candidate for this purpose if we can present an unknown data matrix in a sparse domain. Since the emission spectra of beads have a simple shape with one smooth curve, Discrete Fourier Transform (DFT), which provides sparse results on smooth curves, was selected [90], [91].

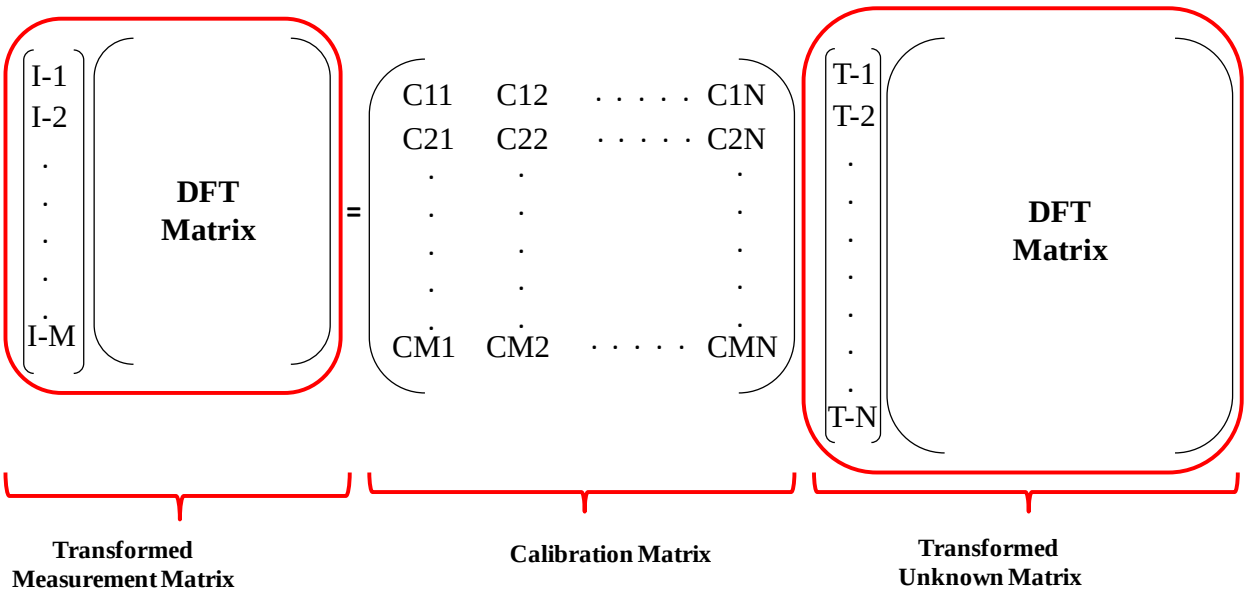


**Figure A-6 | Multiplying components of spectrum recovery equations with DFT matrix transform in order to gain a sparse matrix for an unknown matrix that can be solved using compressive sensing.**

The calibration spectrum that we assigned to each coordinate was similar to the transmission function of the LVF at that point, but it was not the same, in terms of peak wavelength or intensity. One simple way to use calibration spectra to recover the emission spectrum without solving an inverse linear equation is to assign the wavelength corresponding to the peak value for each calibration spectrum to the emission intensity of the flowing bead at that coordinate for the whole travel path. We call this plot method 1-1 mapping since it picks the intensity plot of the emission bead and, just by mapping the location to the wavelength, outputs the emission spectrum.

The plot obtained in this way and the recovery results of the compressive sensing method are shown in the Fig. A-7. For this experiment, by using a similar tracking code to the one that was used in [88], we picked 41 points for 1-1 mapping and 10 points for CS recovery. A good match for the recovery, especially for the peak area, is demonstrated.

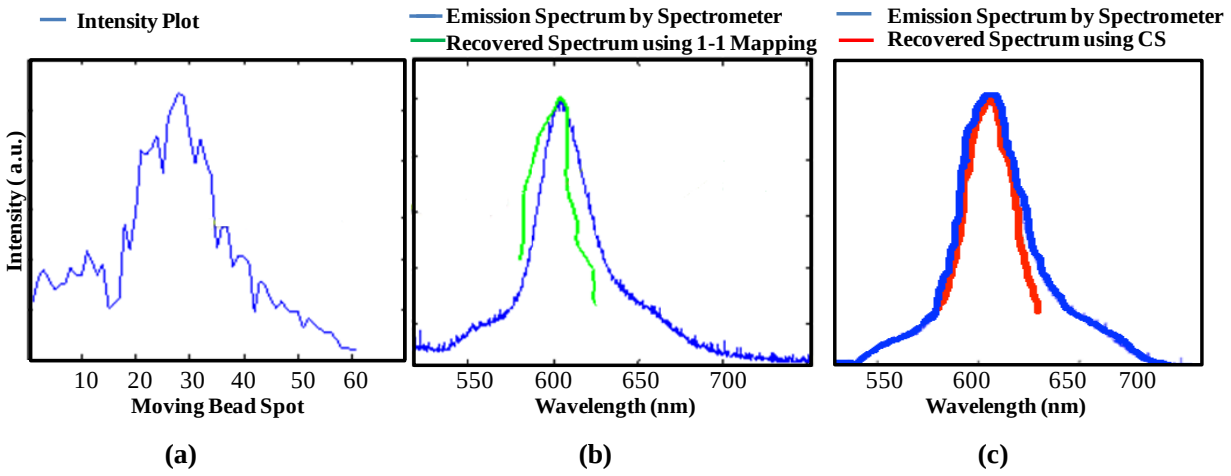


**Figure A-7 | (a) Emission intensity of the moving particle vs. length. (b) Emission spectrum recovery employing 1-1 mapping using calibration spectra. (c) Emission spectrum recovery using compressive sensing and the calibration spectrum.**

## A.8 PDMS-Based Microfluidic Device Fabrication

We used the standard soft lithography process for PDMS-based microfluidic device fabrication [88]. The PDMS polymer and the curing liquid were well mixed at the ratio of 10:1. The many bubbles that resulted from the mixing were eliminated by putting the whole mixture in a stable place for about an hour. A microfluidic mold had been previously made with optical lithography with SU-8 in Nanolab on a 4-inch silicon wafer. The degassed PDMS solution was poured onto the mold surface, and then the mold with the mixture was placed in a 75°C dry bake for two hours. In cases when the exact recommended ratio between PDMS and its agent is attained, the final material can be peeled from the mold without leaving a trace [88].

For the microfluidic device substrate samples, we chose 100 μm-thickness glass, which was very well cleaned with detergent and treated with plasma for one minute to strengthen the adhesion of the glass surface to the PDMS material. Right after the plasma treatment, we placed

the PDMS layer that contains the microfluidic chambers on the surface of the glass so that it stuck to the substrate and formed the microfluidic device. Placing tubes and connecting them to the syringe pump were the next steps to complete the flow system [88].

## A.9 Optofluidic Fluorescent Multicolor Imaging Cytometry on a Cellphone

Cellphones are widely used devices that contain an imaging and processing system as well as wireless technology in one small unit. This fact gave our research group the idea of using this inexpensive and ubiquitous device as a form of biomedical imaging technology, and demonstrations of microscopy [92], [93] and flow cytometry [88] have been presented by the Ozcan Research Group [88]. The whole cytometer is made up of an inexpensive and compact optical attachment that is placed on top of a cellphone. The attachment carries a lens and a sample holder. The lens to be added to the system is intended to bring the image of the biological sample to the farfield so that the camera lens whose focal length is equal to its distance to the cellphone camera will image. There is a demagnification of the object size to the image size, which is equal to the ratio between the focal length of the added lens and the focal length of the cellphone camera lens. With this device, green labeled white blood cells (WBCs) were imaged, with the same resolution and image quality as obtained by a 40X regular fluorescent microscope. In addition, a flow of labeled WBCs were flushed to the system, and using the image-processing algorithm applied on the movie captured by the cellphone, the number of cells was counted with approximately 95% accuracy [88].

Not only can spectroscopy be performed with a cellphone, the same platform can be used for differentiating colorful particles based on their emission spectra. This means that the

emission intensity over the LVF length can be used for labeling and classifying particles without the need for providing the exact spectral information.

The extra lens that we added to the system had the focal length of 4.5 mm. That resulted in almost no demagnification from the particles to the camera image sensor. A glass capillary that was placed directly on top of the LVF had the inner diameter of 0.2 mm and outer diameter of 0.3 mm. The LED light was coupled to the capillary through direct touching, with a droplet of index-matching oil as the interface. As fluorescent particles traveled through the capillary from the sample pool to the syringe pump, they were excited by blue light guided inside the capillary. The emission light by fluorescent beads reached to the CMOS camera, while the blue light not contained in the capillary due to scattering and insufficient blocking was barricaded by an absorption filter placed between two lenses. When there was flow in the system, the cellphone image sensor recorded a movie with 24 fps whose frames could be analyzed in either a cellphone processor or a remote PC.

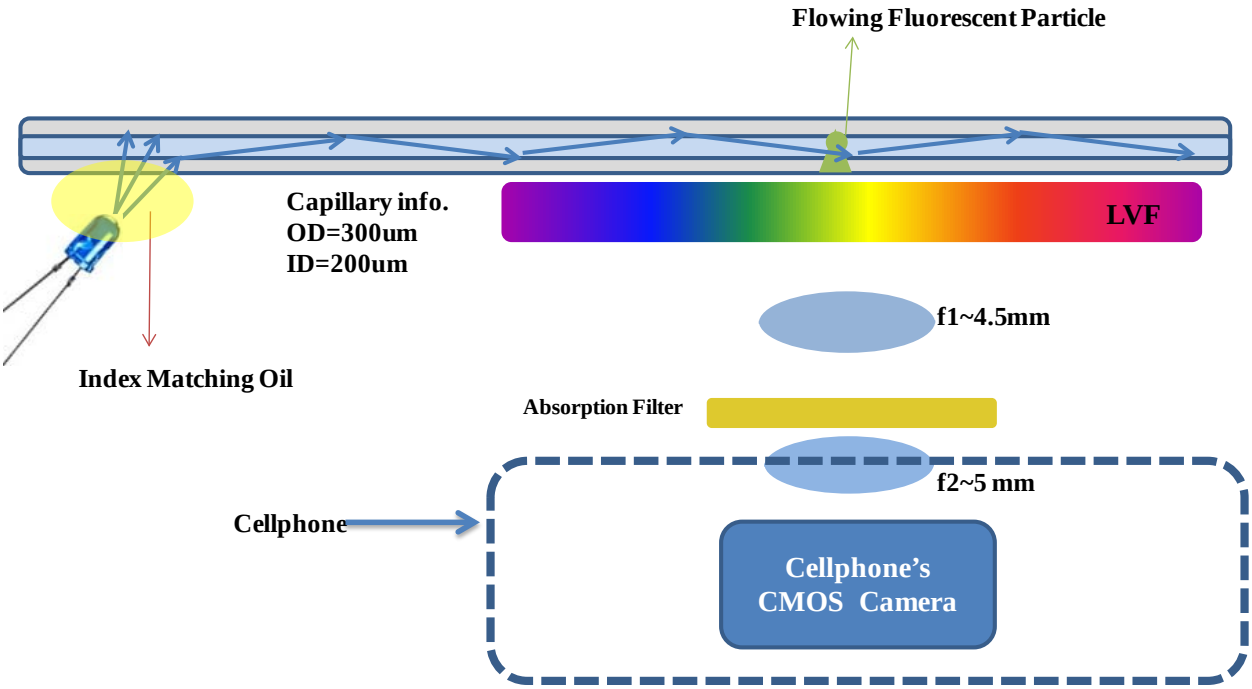


**Figure A-8 | Schematic of the optical components of the optofluidic multicolor imaging cytometry on a cellphone. The capillary is guiding LED light coupled by index-matching oil.**


**Figure A-9 | The entire optofluidic imaging multicolor cytometer on a cellphone.**

## A.10 Bead Detection and Advanced Tracking Algorithm

I mentored and collaborated with an MSc student, Swati Padmanabhan, for the particle counting project. She provided the coding for tracking and classification that I used. Some of the explanations and descriptions about tracking and classification in this chapter have been provided more comprehensively in her final MSc thesis report [94].

The detection algorithm we used here is similar to the algorithm used for single-color cytometry [95], with some advances. The main difference lies in having non-uniform thresholding over the LVF because we had different intensity values transmitted from the LVF, and a single uniform thresholding could not be applicable. After detection, the next step was to apply a tracking algorithm to obtain the spectral information.. For this, we did not rely on the previous code, as there were some problems when using it in cases of high concentrations of solutions. Instead, we chose the *object-oriented* method so that we could save a history of all beads. This helped us avoid counting a bead twice if it became faint or lost in a few frames [94].

One important step in tracking the algorithm was to estimate the location of the bead in the next frame, which is known as *motion estimation* in the video processing community [96]. An algorithm for location prediction based on the correlation method was deployed. When a 2D correlation of a window was applied around one bead position in the current frame and the next frame, the correlated image had the maximum value at the location where the bead was sitting in the next frame. Afterwards, by filtering the correlated image with a 2D Gaussian image centered at the roughly estimated bead location, we could achieve the final prediction of the bead location, which was used for the bead search (based on local maxima) in the next frame [94], [97].

## A.11 Classification Method Using k-Nearest Neighbor (k-NN) Classification

To differentiate and classify bead spectra corresponding to various particle types, the k-NN classification algorithm was used [94], [98] and applied it on the emission plots. This processing step, along with the tracking and counting method, resulted in counting particles that belonged to one category. One straightforward classifier that assigns an unknown new-coming object to a group is called *k-nearest neighbor*, or *k-NN*. This picked the *k* members in the calibration or training data with the smallest distance from the unlabeled element, and after a voting process based on the majority of known objects that had the minimum distance, we determined the group to which the new objects belonged. As obvious from the explanation, the key parameters of this classifier were (a) a set of labeled or training data from known and already correctly classified data, (b) a measurement metric for defining the distance metric, and (c) *k* as the number of labeled elements to be chosen for the final decision [99–102].

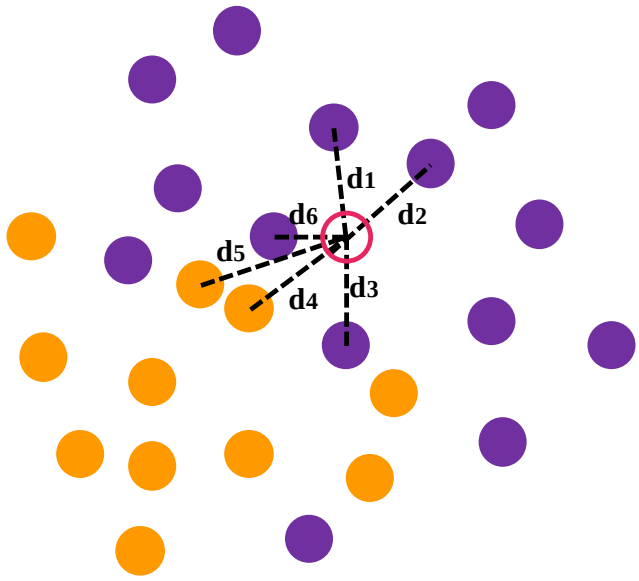


**Figure A-10 | The distance from an unknown object, shown by the empty red circle to six known already labeled beads, for a two-dimensional problem in k-NN classification with k = 6 [101].**

In our work, we defined $\vec{x}$ and $\vec{y}$ as two data sets of interest with vector information represented as follows [98]:

$$\vec{x} = (x_1, x_2, \dots, x_n) \quad and \quad \vec{y} = (y_1, y_2, \dots, y_n)$$

The distance between these two points used in our processing is Euclidean distance, which is defined mathematically as below:

$$D(\vec{x}, \vec{y}) = \sqrt{(x_1 - y_1)^2 + (x_2 - y_2)^2 + \cdots + (x_n - y_n)^2} \tag{5-1}$$

In our classification project, we sampled the LVF length at equal distances in 25 positions, regardless of the number of segments we chose for non-uniform thresholding. This number was chosen based on experimental specifications, and we achieved good results with it.

## A.12 Calibration Procedure and Experimental Results

As explained in the previous section, for the k-NN classification, we needed a set of data whose labels were known. In our experimental set-up, we let a small flow of known bead colors, such as red and green, pass through the capillary volume separately. A movie corresponding to each bead color type was recorded and employed to extract calibration data. This data was then used in analyzing a mixture of different colored beads. The calibration spectra were obtained when the emission spectra of beads of a single color were non-uniformly thresholded and sampled at equal spaces, and the final data set was used for final comparison. The number of fluorescent particles we needed for the calibration spectra could be less than 100, and it could be achieved by a 30-second flow with a reasonable concentration. After the calibration procedure, a mixture of different beads was used for testing purposes. At this stage, two processes needed to run in parallel. The first one involved tracking each bead and taking out its spectral data set to compare with the calibration data for label or color identification.

The second step was to update the number of beads in each group, based upon the decision made in classification. Knowing the concentration of beads in the solution (by previous examination) and the syringe pump liquid flow rate, we could predict the number of beads over the time per frame.

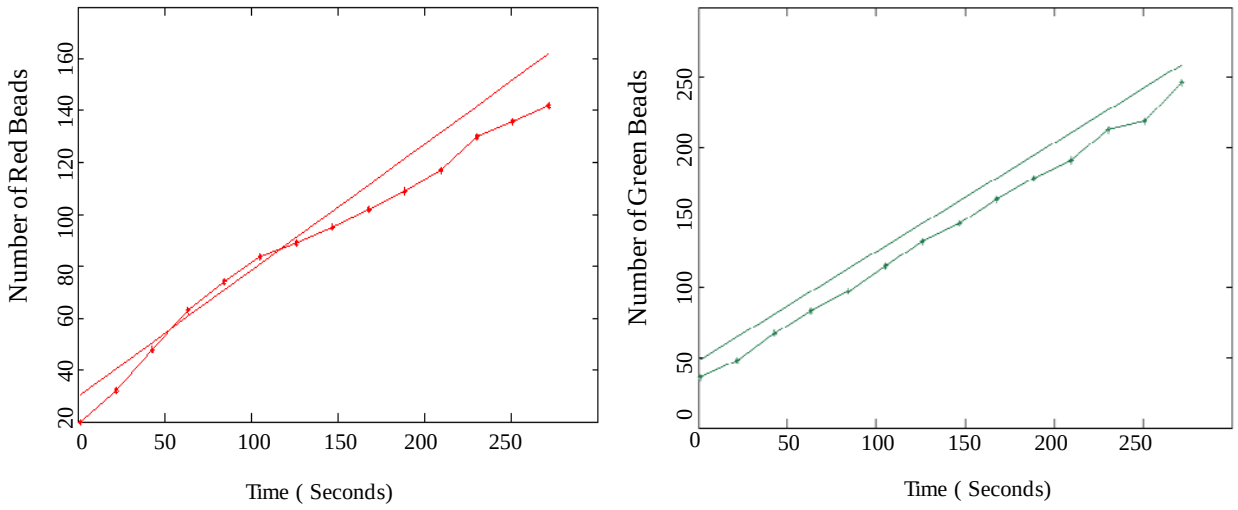


**Figure A-11 | Experimental data comparing the expected number of beads in a solution with the number of beads counted (indicated with '*') for each color.**

## A.13 Conclusion

In this chapter, I introduced an optofluidic multicolor cytometry and spectroscopy device installable on a cellphone. The device, based on advanced tracking and a k-NN classification algorithm, is capable of differentiating fluorescent particles in a liquid flow (based on their emission spectra) and counting the number of particles corresponding to each color. This handheld device can be used for blood analysis when various blood cells, such as CD4 and CD3 cells, are labeled with different fluorescent or quantum dot particles.

# References


[1] M. Vollmer, K. Möllmann, *Infrared Thermal Imaging: Fundamentals, Research and Applications,* Wiley-VCH Verlag GmbH & Co. KGaA, 2010.

[2] D. J. Brady, *Optical Imaging and Spectroscopy*. John Wiley & Sons, Inc., and The Optical Society of America, 2009.

[3] O. Mudanyali, D. Tseng, C. Oh, S. O. Isikman, I. Sencan, W. Bishara, C. Oztoprak, S. Seo, B. Khademhosseini, and A. Ozcan, "Compact, light-weight and cost-effective microscope based on lensless incoherent holography for telemedicine applications," *Lab on a Chip*, vol. 10, no. 11, p. 1417, 2010.

[4] M. Gu, *Advanced Optical Imaging Theory*. Springer, 2000.

[5] S. O. Isikman, A. Greenbaum, M. Lee, W. Bishara, O. Mudanyali, T. W. Su, and A. Ozcan, "Lensfree computational microscopy tools for cell and tissue imaging at the point-of-care and in low-resource settings," *Analytical Cellular Pathology*, vol. 35, no. 4, pp. 229–247, 2012.

[6] D. Gabor, "A New Microscopic Principle," *Nature*, vol. 161, no. 4098, pp. 777–778, May 1948.

[7] Z. Gorocs and A. Ozcan, "On-Chip Biomedical Imaging," *IEEE Reviews in Biomedical Engineering*, p. In Press, 2012.

[8] J. Di, J. Zhao, H. Jiang, P. Zhang, Q. Fan, and W. Sun, "High resolution digital holographic microscopy with a wide field of view based on a synthetic aperture technique and use of linear CCD scanning," *Applied optics*, vol. 47, no. 30, pp. 5654–5659, 2008.

[9] M. F. Toy, S. Richard, J. Kühn, ,A. Franco-Obregón, M. Egli, C. Depeursinge, "Enhanced robustness digital holographic microscopy for demanding environment of space biology," *Biomedical Optics Express*, vol. 3, no. 2, pp. 313–326, Feb. 2012.

[10] J. C. H. Spence, “Diffractive (lensless) imaging,” *Science of Microscopy*, pp. 1196–1227, 2007.

[11] W. Xu, M. H. Jericho, I. A. Meinertzhagen, and H. J. Kreuzer, “Digital in-line holography for biological applications,” *Proceedings of the National Academy of Sciences*, vol. 98, no. 20, p. 11301, Sept. 2001.

[12] C. Oh, S. O. Isikman, B. Khademhosseini, and A. Ozcan, “On-chip differential interference contrast microscopy using lensless digital holography,” *Optics Express*, vol. 18, 2010.

[13] S. Seo, T.-W. Su, A. Erlinger, and A. Ozcan, “Multi-color LUCAS: Lensfree On-chip Cytometry Using Tunable Monochromatic Illumination and Digital Noise Reduction,” *Cellular and Molecular Bioengineering*, vol. 1, no. 2–3, pp. 146–156, Aug. 2008.

[14] W. Bishara, T. W. Su, A. F. Coskun, and A. Ozcan, “Lensfree on-chip microscopy over a wide field-of-view using pixel super-resolution,” *Optics Express*, vol. 18, no. 11, pp. 11181–11191, 2010.

[15] X. Cui, L. M. Lee, X. Heng, W. Zhong, P. W. Sternberg, D. Psaltis, and C. Yang, “Lensless high-resolution on-chip optofluidic microscopes for Caenorhabditis elegans and cell imaging,” *Proceedings of the National Academy of Sciences*, vol. 105, no. 31, pp. 10670–10675, Aug. 2008.

[16] A. F. Coskun, I. Sencan, T. W. Su, and A. Ozcan, “Lensless wide-field fluorescent imaging on a chip using compressive decoding of sparse objects,” *Optics Express*, vol. 18, no. 10, pp. 10510–10523, May. 2010.

[17] D. L. Donoho, “Compressed sensing,” *IEEE Transactions on Information Theory*, vol. 52, no. 4, pp. 1289–1306, Apr. 2006.

[18] A. F. Coskun, T.-W. Su, and A. Ozcan, “Wide field-of-view lens-free fluorescent imaging on a chip,” *Lab on a Chip*, vol. 10, no. 7, p. 824, 2010.

[19] A. F. Coskun, I. Sencan, T.-W. Su, and A. Ozcan, “Wide-field lensless fluorescent microscopy using a tapered fiber-optic faceplate on a chip,” *The Analyst*, vol. 136, no. 17, p. 3512, 2011.

[20] B. Rothenhausler, W. Knoll, “Surface-plasmon microscopy,” *Nature*, vol. 332, pp. 615–617, Apr. 1988.

[21] B. Beusink, “Label-free biomolecular interaction sensing on microarrays using surface plasmon resonance imaging,” PhD dissertation, University of Twente, The Netherlands, 2009.

[22] H. Raether, *Surface Plasmons, on Smooth and Rough Surfaces, and on Gratings*. Springer Verlag, 1986.

[23] P. Englebienne, A. V. Hoonacker, and M. Verhas, “Surface plasmon resonance: principles, methods and applications in biomedical sciences,” *Journal of Spectroscopy*, vol. 17, no. 2–3, pp. 255–273, 2003.

[24] J. N. Anker, W. P. Hall, O. Lyandres, N. C. Shah, J. Zhao, and R. P. Van Duyne, “Biosensing with plasmonic nanosensors,” *Nature materials*, vol. 7, no. 6, pp. 442–453, 2008.

[25] J.-W. Choi, D.-Y. Kang, Y.-H. Jang, H.-H. Kim, J. Min, and B.-K. Oh, “Ultra-sensitive surface plasmon resonance based immunosensor for prostate-specific antigen using gold nanoparticle–antibody complex,” *Colloids and Surfaces A: Physicochemical and Engineering Aspects*, vol. 313–314, pp. 655–659, Feb. 2008.

[26] M. A. Cooper, “Optical biosensors in drug discovery,” *Nature Reviews Drug Discovery*, vol. 1, no. 7, pp. 515–528, Jul. 2002.

[27] Y.-J. Li, J. Xiang, and F. Zhou, “Sensitive and Label-Free Detection of DNA by Surface Plasmon Resonance,” *Plasmonics*, vol. 2, no. 2, pp. 79–87, Jun. 2007.

[28] J. Melendez, R. Carr, D. U. Bartholomew, K. Kukanskis, J. Elkind, S. Yee, C. Furlong, and R. Woodbury, “A commercial solution for surface plasmon sensing,” *Sensors and Actuators B: Chemical*, vol. 35, no. 1, pp. 212–216, 1996.

[29] R. Adato, A. A. Yanik, and H. Altug, “On Chip Plasmonic Monopole Nano-Antennas and Circuits,” *Nano Letters*, vol. 11, no. 12, pp. 5219–5226, Dec. 2011.

[30] H. Schmidt and A. R. Hawkins, “The photonic integration of non-solid media using optofluidics,” *Nature Photonics*, vol. 5, no. 10, pp. 598–604, Aug. 2011.

[31] A. Ashkin, “Optical trapping and manipulation of neutral particles using lasers,” *Proceedings of the National Academy of Sciences*, vol. 94, no. 10, pp. 4853–4860, 1997.

[32] B. Khademhosseinieh, I. Sencan, G. Biener, T.-W. Su, A. F. Coskun, D. Tseng, and A. Ozcan, “Lensfree on-chip imaging using nanostructured surfaces,” *Applied Physics Letters*, vol. 96, no. 17, p. 171106, 2010.

[33] B. Khademhosseinieh, G. Biener, I. Sencan, and A. Ozcan, “Lensfree color imaging on a nanostructured chip using compressive decoding,” *Applied Physics Letters*, vol. 97, no. 21, p. 211112, 2010.

[34] W. S. Haddad, D. Cullen, J. C. Solem, J. W. Longworth, A. McPherson, K. Boyer, and C. K. Rhodes, “Fourier-transform holographic microscope,” *Appl. Opt.*, vol. 31, no. 24, pp. 4973–4978, 1992.

[35] G. Pedrini and H. J. Tiziani, “Short-coherence digital microscopy by use of a lensless holographic imaging system,” *Applied optics*, vol. 41, no. 22, pp. 4489–4496, 2002.

[36] L. Repetto, E. Piano, and C. Pontiggia, “Lensless digital holographic microscope with light-emitting diode illumination,” *Optics letters*, vol. 29, no. 10, pp. 1132–1134, 2004.

[37] X. Cui, L. M. Lee, X. Heng, W. Zhong, P. W. Sternberg, D. Psaltis, and C. Yang, “Lensless high-resolution on-chip optofluidic microscopes for Caenorhabditis elegans and cell imaging,” *Proceedings of the National Academy of Sciences*, vol. 105, no. 31, p. 10670, 2008.

[38] S. Seo, T.-W. Su, D. K. Tseng, A. Erlinger, and A. Ozcan, “Lensfree holographic imaging for on-chip cytometry and diagnostics,” *Lab on a Chip*, vol. 9, no. 6, p. 777, 2009.

[39] C. Oh, S. O. Isikman, B. Khademhosseinieh, and A. Ozcan, “On-chip differential interference contrast microscopy using lensless digital holography,” *Opt. Express*, vol. 18, no. 5, pp. 4717–4726, Mar. 2010.

[40] Ahmet F. Coskun, Ting-wei Su, Ikbal Sencan, and Aydogan Ozcan, “Lensfree Fluorescent On-Chip Imaging Using Compressive Sampling,” *Optics & Photonics News*, pp. 27–27, 2010.

[41] S.-J. Kim, K. Koh, M. Lustig, S. Boyd, and D. Gorinevsky, “An Interior-Point Method for Large-Scale $l_1$-Regularized Least Squares,” *IEEE Journal of Selected Topics in Signal Processing*, vol. 1, no. 4, pp. 606–617, Dec. 2007.

[42] E. J. Candes and M. B. Wakin, “An Introduction To Compressive Sampling,” *IEEE Signal Processing Magazine*, vol. 25, no. 2, pp. 21–30, Mar. 2008.

[43] E. J. Candes, J. K. Romberg, and T. Tao, “Stable signal recovery from incomplete and inaccurate measurements,” *Communications on pure and applied mathematics*, vol. 59, no. 8, pp. 1207–1223, 2006.

[44] S. Boyd, L. Vandenberghe, *Convex Optimization*, Seventh. Cambridge University Press, 2009.

[45] E. J. Candes and T. Tao, “Near-Optimal Signal Recovery From Random Projections: Universal Encoding Strategies?,” *IEEE Transactions on Information Theory*, vol. 52, no. 12, pp. 5406–5425, Dec. 2006.

[46] “Infrared Cameras Inc. at <http://www.infraredcamerasinc.com/>.”

[47] Bahar Khademhosseinieh, Gabriel Biener, Ikbal Sencan, “Lens-free, near-infrared (NIR) imaging using structured substrates and compressive sensing,” *Defense, Security, and Sensing Conference*, Apr. 2012.

[48] B. Khademhosseinieh, G. Biener, I. Sencan, T.-W. Su, A. F. Coskun, and A. Ozcan, “Lensfree sensing on a microfluidic chip using plasmonic nanoapertures,” *Applied Physics Letters*, vol. 97, no. 22, p. 221107, 2010.

[49] J. Homola, “Present and future of surface plasmon resonance biosensors,” *Analytical and Bioanalytical Chemistry*, vol. 377, no. 3, pp. 528–539, Oct. 2003.

[50] C. Escobedo, S. Vincent, A. I. K. Choudhury, J. Campbell, A. G. Brolo, D. Sinton, and R. Gordon, "Integrated nanohole array surface plasmon resonance sensing device using a dual-wavelength source," *Journal of Micromechanics and Microengineering*, vol. 21, no. 11, p. 115001, Nov. 2011.

[51] W. L. Barnes, A. Dereux, T. W. Ebbesen, and others, "Surface plasmon subwavelength optics," *Nature*, vol. 424, no. 6950, pp. 824–830, 2003.

[52] Lukas Novotny, Bert Hecht, *Principles of Nano-Optics*. Cambridge University Press, 2006.

[53] K. A. Willets and R. P. Van Duyne, "Localized Surface Plasmon Resonance Spectroscopy and Sensing," *Annual Review of Physical Chemistry*, vol. 58, no. 1, pp. 267–297, May 2007.

[54] M. Chamanzar, Z. Xia, E. Shah Hosseini, S. Yegnanarayanan, and A. Adibi, "On-chip Localized Surface Plasmon Resonance (LSPR) Sensing using Hybrid Plasmonic-photonic-fluidic Structures," in *CLEO: Science and Innovations*, 2012.

[55] F. García-Vidal and L. Martín-Moreno, "Transmission and focusing of light in one-dimensional periodically nanostructured metals," *Physical Review B*, vol. 66, no. 15, Oct. 2002.

[56] G. D. VanWiggeren, M. A. Bynum, J. P. Ertel, S. Jefferson, K. M. Robotti, E. P. Thrush, D. M. Baney, and K. P. Killeen, "A novel optical method providing for high-sensitivity and high-throughput biomolecular interaction analysis," *Sensors and Actuators B: Chemical*, vol. 127, no. 2, pp. 341–349, Nov. 2007.

[57] F. García-Vidal, E. Moreno, J. Porto, and L. Martín-Moreno, "Transmission of Light through a Single Rectangular Hole," *Physical Review Letters*, vol. 95, no. 10, Aug. 2005.

[58] M. Najiminaini, F. Vasefi, B. Kaminska, and J. J. L. Carson, "Nano-hole array structure with improved surface plasmon energy matching characteristics," *Applied Physics Letters*, vol. 100, no. 4, pp. 043105–043105, 2012.

[59] E. Hutter and J. H. Fendler, "Exploitation of Localized Surface Plasmon Resonance," *Advanced Materials*, vol. 16, no. 19, pp. 1685–1706, Oct. 2004.

[60] L. Pang, G. M. Hwang, B. Slutsky, and Y. Fainman, "Spectral sensitivity of two-dimensional nanohole array surface plasmon polariton resonance sensor," *Applied Physics Letters*, vol. 91, no. 12, p. 123112, 2007.

[61] D. Tseng, O. Mudanyali, C. Oztoprak, S. O. Isikman, I. Sencan, O. Yaglidere, and A. Ozcan, "Lensfree microscopy on a cellphone," *Lab on a Chip*, vol. 10, no. 14, p. 1787, 2010.

[62] L. Verslegers, P. B. Catrysse, Z. Yu, J. S. White, E. S. Barnard, M. L. Brongersma, and S. Fan, "Planar Lenses Based on Nanoscale Slit Arrays in a Metallic Film," *Nano Letters*, vol. 9, no. 1, pp. 235–238, Jan. 2009.

[63] D.R. Lide, *Handbook of Chemistry and Physics*. CRC-LCC, 2004.

[64] J. R. Fienup, "Phase retrieval algorithms: a comparison," *Applied Optics*, vol. 21, no. 15, pp. 2758–2769, 1982.

[65] K. Matsushima and T. Shimobaba, "Band-limited angular spectrum method for numerical simulation of free-space propagation in far and near fields," *Optics Express*, vol. 17, no. 22, pp. 19662–19673, 2009.

[66] S. W. Hell, "Far-Field Optical Nanoscopy," *Science*, vol. 316, no. 5828, pp. 1153–1158, May 2007.

[67] L. Schermelleh, R. Heintzmann, and H. Leonhardt, "A guide to super-resolution fluorescence microscopy," *The Journal of Cell Biology*, vol. 190, no. 2, pp. 165–175, Jul. 2010.

[68] JB Pawley, *Handbook of Biological Confocal Microscopy*, 3rd ed. Berlin: Springer, 2006.

[69] M. Minsky, "Microscopy Apparatus," U.S. Patent 3, 031, 467.

[70] S. W. Hell and J. Wichmann, "Breaking the diffraction resolution limit by stimulated emission: stimulated-emission-depletion fluorescence microscopy," *Optics letters*, vol. 19, no. 11, pp. 780–782, 1994.

[71] S. W. Hell and M. Kroug, “Ground-state-depletion fluorscence microscopy: A concept for breaking the diffraction resolution limit,” *Applied Physics B: Lasers and Optics*, vol. 60, no. 5, pp. 495–497, 1995.

[72] Brent Bailey, Daniel L.Farkas, D. Lansing Taylor, and Fredrick Lanni, “Enhanement of axial resolution in fluorescence microscopy by standing-wave excitation,” *Nature*, vol. 366, pp. 44–48, Nov. 1993.

[73] Eric Betzig, George H. Patterson, Rachid Sougrat, O. Wolf Lindwasser, Scott Olenych, Juan S. Bonifacino, Michael W. Davidson, Jennifer Lippincott-Schwartz,Harald F. Hess, “Imaging Intracellular Fluorescent Proteins at Nanometer Resolution,” *Science*, vol. 313, pp. 1642–1646, Sep. 2006.

[74] M. J. Rust, M. Bates, and X. Zhuang, “Sub-diffraction-limit imaging by stochastic optical reconstruction microscopy (STORM),” *Nature Methods*, vol. 3, no. 10, pp. 793–796, Aug. 2006.

[75] P. M. Shankar, W. C. Hasenplaugh, R. L. Morrison, R. A. Stack, and M. A. Neifeld, “Multiaperture imaging,” *Applied optics*, vol. 45, no. 13, pp. 2871–2883, 2006.

[76] R. C. Hardie, K. J. Barnard, J. G. Bognar, E. E. Armstrong, and E. A. Watson, “High-resolution image reconstruction from a sequence of rotated and translated frames and its application to an infrared imaging system,” *Optical Engineering*, vol. 37, no. 1, pp. 247–260, 1998.

[77] M. Irani, and Shmuel Peleg, “Improving Resolution by Image Registration,” *IEEE SIGNAL PROCESSING MAGAZINE*, vol. 53, no. 3, pp. 231–239, May 1991.

[78] M. Irani, and S. Peleg, “Motion analysis for image enhancement: Resolution, occlusion, and transparency,” *Journal of Visual Communication and Image Representation*, vol. 4, no. 4, pp. 1993–12, 1993.

[79] S. C. Park, M. K. Park, and M. G. Kang, “Super-resolution image reconstruction: a technical overview,” *Signal Processing Magazine, IEEE*, vol. 20, no. 3, pp. 21–36, 2003.

[80] M. Elad and A. Feuer, “Restoration of a single superresolution image from several blurred, noisy, and undersampled measured images,” *Image Processing, IEEE Transactions on*, vol. 6, no. 12, pp. 1646–1658, 1997.

[81] C. Richard, A. Renaudin, V. Aimez, and P. G. Charette, “An integrated hybrid interference and absorption filter for fluorescence detection in lab-on-a-chip devices,” *Lab on a Chip*, vol. 9, no. 10, p. 1371, 2009.

[82] A. F. Coskun, I. Sencan, T.-W. Su, and A. Ozcan, “Lensfree Fluorescent On-Chip Imaging of Transgenic Caenorhabditis elegans Over an Ultra-Wide Field-of-View,” *PLoS ONE*, vol. 6, no. 1, p. e15955, Jan. 2011.

[83] B. Khademhosseinieh, I. Sencan, G. Biener, A.Ozcan, “Use of Nanostructured Surfaces to Enable Higher Resolution Detector Arrays for Lensfree Imaging and Sensing on a Chip", *Nanoelectronic Devices for Defense and Security Conference ( Nano DDS)*, New York, August 29-September 1, 2011.

[84] “DNA microarray, http://en.wikipedia.org/wiki/DNA_microarray ( accessed 2012-09-12),” *wikipedia*. .

[85] A. Emadi, H. Wu, G. de Graaf, K. Hedsten, P. Enoksson, J. H. Correia, and R. F. Wolffenbuttel, “An UV linear variable optical filter-based micro-spectrometer,” *Procedia Engineering*, vol. 5, pp. 416–419, Jan. 2010.

[86] McNamara, G., Larson, J. M., Schwartz, S. A. & Davidson, M. W., “Nikon Microscopy U: The Source for Microscopy Education, http://www.microscopyu.com/articles/confocal/spectralimaging.html (accessed 10 May 2012).”

[87] Joseph R.Lakowicz, *Principles of Fluorescent Spectroscopy*, Third. Springer, 2010.

[88] H. Zhu, S. Mavandadi, A. F. Coskun, O. Yaglidere, and A. Ozcan, “Optofluidic Fluorescent Imaging Cytometry on a Cell Phone,” *Analytical Chemistry*, vol. 83, no. 17, pp. 6641–6647, Sep. 2011.

[89] P. D. Nation, A. Q. Howard, and L. J. Webb, “Modeling biological fluorescence emission spectra using Lorentz line shapes and nonlinear optimization,” *Applied optics*, vol. 46, no. 24, pp. 6192–6195, 2007.

[90] C. R. Berger, Z. Wang, J. Huang, and S. Zhou, “Application of compressive sensing to sparse channel estimation,” *Communications Magazine, IEEE*, vol. 48, no. 11, pp. 164–174, 2010.

[91] Wakin, Michael, Jason Laska, Marco Duarte, Dror Baron, Shriram Sarvotham, Dharmpal Takhar, Kevin F. Kelly, and Richard G. Baraniuk, presented at the Picture Coding Symposium., 2006.

[92] H. Zhu, O. Yaglidere, T.-W. Su, D. Tseng, and A. Ozcan, “Cost-effective and compact wide-field fluorescent imaging on a cell-phone,” *Lab on a Chip*, vol. 11, no. 2, p. 315, 2011.

[93] H. Zhu, U. Sikora, and A. Ozcan, “Quantum dot enabled detection of Escherichia coli using a cell-phone,” *The Analyst*, vol. 137, no. 11, p. 2541, 2012.

[94] S. Padmanabhan, “Multi Colour Flow Cytometry on a Mobile Phone,” M.S. thesis, Dept. Elect. Eng. UCLA, 2012.

[95] S. Suzuki, K. be, “Topological structural analysis of digitized binary images by border following,” *ELSEVIER*, vol. 30, no. 1, pp. 32–46, Apr. 1985.

[96] Y.Bar-Shalom,X.-Rong Li, Thiagalingam Kirubarajan, *Estimation with Applications to Tracking and Navigation*, [Online]. John Wiley and Sons, Inc., 2002.

[97] J. C. Crocker, D. G. Grier, and others, “Methods of digital video microscopy for colloidal studies,” *Journal of colloid and interface science*, vol. 179, no. 1, pp. 298–310, 1996.

[98] J. C. Bezdek, S. K. Chuah, and D. Leep, “Generalized k-nearest neighbor rules,” *Fuzzy Sets and Systems*, vol. 18, no. 3, pp. 237–256, 1986.

[99] “Lecture 12. Classification at <http://research.cs.tamu.edu/prism/lectures/iss/iss_l12.pdf>,” (accesses 2012-09-14).

[100] N. Bhatia and Vandana, “Survey of nearest neighbor techniques,” *International Journal of Computer Science and Information Security*, vol. 8, no. 2, 2010.

[101] P. Cunningham and S. J. Delany, “k-Nearest neighbour classifiers,” *Multiple Classifier Systems*, pp. 1–17, 2007.

[102] B. Li, S. Yu, and Q. Lu, “An improved k-nearest neighbor algorithm for text categorization,” *Proceedings of the 20th international conference on computer processing of oriental languages*, 2003.